

# **ALPHA FOUNDATION FOR THE IMPROVEMENT OF MINE SAFETY AND HEALTH**

## **Final Technical Report**

**Project Title:** Autonomous Robotic Early Warning System for Underground Stone Mining Safety

**Grant Number:** AFC820-69

**Organization:** West Virginia University, Morgantown, WV  
886 Chestnut Ridge Road, PO Box 6845  
Morgantown, WV 26506-6845

**Principal Investigator:** Ihsan (Berk) Tulu, Ph.D. (ME)  
Phone: 304-293-3883, E-mail: [itulu@mail.wvu.edu](mailto:itulu@mail.wvu.edu)

**Co-Principal Investigators:** Jason N. Gross, Ph.D. (MAE)  
E-mail: [jason.Gross@mail.wvu.edu](mailto:jason.Gross@mail.wvu.edu)

Yu Gu, Ph.D. (MAE)  
E-mail: [Yu.Gu@mail.wvu.edu](mailto:Yu.Gu@mail.wvu.edu)

Guilherme A. S. Pereira, Ph.D. (MAE)  
E-mail: [guilherme.pereira@mail.wvu.edu](mailto:guilherme.pereira@mail.wvu.edu)

**Period of Performance:** September 1, 2019 – April 30, 2023

**Disclaimer:** This study was sponsored by the Alpha Foundation for the Improvement of Mine Safety and Health, Inc. (ALPHA FOUNDATION). The views, opinions and recommendations expressed herein are solely those of the authors and do not imply any endorsement by the ALPHA FOUNDATION, its Directors and staff.

## 1.0 Executive Summary:

**Problem statement:** In the underground stone mining industry ground falls from roofs and pillars have been responsible for over 40% of fatalities since 2006 (MSHA, 2016). In general, underground stone mines have naturally strong rockmass and the modern pillar and roof span design guidelines developed by National Institute for Occupational Safety and Health (NIOSH) were published in 2011 and have improved the design of stable layouts for modern limestone mines. However, since then, five massive pillar collapses occurred in older workings of active limestone mines, and four out of five occurred after 2020. On January 7, 2022, a massive roof fall claimed the life of a dozer operator in an underground mine operating in the Loyalhanna formation, and reports of extensive regionalized roof falls in other mines demonstrated the potentially severe risk to the safety of miners in underground stone mines. In these mines, previously mined sections stay open for the life of the mine, which may be many years and subject the pillars to time-dependent degradation, which is not covered in the NIOSH guidelines. Mine Safety and Health Administration (MSHA) indicated that there is not any design method available to predict when, or even whether, a particular pillar or group of pillars would collapse, but it is possible to recognize hazards that might increase the likelihood of these massive collapses (MSHA, 2021). Safety in the stone mines would be improved with a safe and efficient way to monitor these old pillars and provide a long-term stability assessment and/or warn of pillar instability.

**Research approach:** Unmanned Aerial Vehicles (UAV) and Unmanned Ground Vehicles (UGV) can be used to scan old workings and capture high-resolution 3D maps of these areas that can be used for assessment of pillar and roof damage, and stability. This project developed an autonomous robotic system that is comprised of an Unmanned Aerial Vehicle (UAV) tethered to an Unmanned Ground Vehicle (UGV) and accompanying integrated hazard mapping (Stability-Mapping) / boundary element modeling (LaModel) approach for the assessment of stone mine pillar stability. This combination of remote vehicles can optimally provide high-resolution 3D maps, which are then used as input for the assessment of stability. The research accomplished in this project includes: (i) Develop a proof of concept of a robotics system specifically for stone mine inspection. (ii) Develop a framework for integrating hazard mapping (Stability-Mapping) and boundary element modeling (LaModel) for the assessment of stone mine pillar stability. (iii) Test and verify the integrated autonomous robotics and Stability-Mapping based underground stone mine hazard detection and early warning system in the field.

**Accomplishments:** During this research study, a TRL 7 technology autonomous robotics system composed of an UGV, called Rhino, and a tethered unmanned aerial vehicle (TUAV), known as Oxpecker, was developed. In addition to this new technology, this research project produced a practical stone mine pillar design framework and accompanying software tool that utilizes the empirical stone mine pillar equation, Large Discontinuity Factor (LDF), AutoCAD ObjectARX add-in Integrated Stability Mapping Software (ISMS), and LaModel software.

**Expected impact on mining health and safety:** Autonomous UAV/UGV robotic system and integrated software tools developed in this project are expected to reduce injuries of underground stone mine workers.

## **2.0 Problem Statement and Objective:**

### **The Research Focus Area**

The goal of this research is to reduce the exposure of stone mine workers to fall of ground through the development of enhanced monitoring and warning system for pillar stability with an integrated autonomous robotic system, hazard mapping, and pillar stability analysis. While the problem of pillar stability is associated with all underground operations, this project focused on the underground stone mining industry and addresses the Alpha Foundation Research Topical Area “*Health and Safety Interventions*” with a specific emphasis on “*prevention of unstable ground conditions that result in collapses and roof/rib falls*”. This work is directly relevant to Alpha Foundation Priority Areas 1) *Ground Control - Prevention of unstable ground conditions that result in collapses; roof and rib falls; and injuries due to insufficient support coverage*, and 2) *Monitoring Systems and Integrated Control Technologies - Recognition of and intervention to prevent the escalation of conditions that lead to health and safety risks before they reach hazardous levels*.

### **The Problem Statement**

There are now approximately 100 active underground stone mines operating in 19 states (Rumbaugh et al., 2022). Underground stone mines generally have a long operational life and previously mined sections stay open for the life of the mine and subject the pillars to weathering and age-related degradation (Rumbaugh et al., 2022). Further, these older workings are not typically inspected due to the difficulty of covering vast areas of mine workings with limited personnel, and Rumbaugh et al. (2022) indicated that many of these older pillars were designed with less sufficient safety factors.

In the eastern United States, four underground stone mines have seen five massive pillar collapses since 2015. The pillar failures in three of the four mines happened in older workings that were at least 15 years old (Rumbaugh et al., 2022). The National Institute for Occupational Safety and Health (NIOSH) has made several efforts in the development of ground control tools and design guidelines to help mine workers recognize, create, and keep a safe and healthy workplace. Among these guidelines, it can be found the “*Pillar and Roof Span Design Guidelines for Underground Stone Mines*” published by NIOSH (Esterhuizen et al., 2011). These empirical design guidelines have helped to identify critical aspects of pillar and roof instability. However, considering there are only about 100 limestone mines operating in the United States, the five recent pillar collapses indicate a potentially severe risk to the safety of miners in underground stone mines still exists (Rumbaugh et al., 2022).

Rumbaugh et al. (2022) studied five recent collapses and summarized the factors that may increase the likelihood of a pillar collapse. They stated that two factors, pillar stability and width-to-height ratio, are the most critical, and they recommended the S-Pillar approach for the assessment of pillar stability. They also indicated that the pillar stability analysis must consider the depth of cover, extraction ratio, actual pillar dimensions, limestone strength, and the presence of joints or other geologic features. They stated the possibility that the mine maps for older working can be inaccurate and recommended the verification of the pillar layout dimensions. They also recommended including the variability of pillar dimensions to the design with the following

explanation “*if some pillars within the array are significantly smaller than the others then these smaller pillars can fail first, transfer stress to neighboring pillars, and subsequently trigger a pillar collapse.*” They also stated the weakness of the tributary area theory to estimate the true vertical stress distribution under variable overburden depth and when pillars are shaped irregularly. Their research results also indicated the importance of identifying major geological features that would increase the likelihood of a pillar collapse or roof/rib fall, similar conclusions were driven by Esterhuizen et al. (2019) and Evanek et al. (2022) too.

Therefore, proper inspection of the ribs, roofs, and pillars to identify deteriorating ground conditions, actual 3D geometry of pillar layouts, and geological hazards; and proper assessment of pillar stability with a method that incorporates the geological factors, overburden stress distribution under variable topography, and irregular pillar layouts to design would protect miners from possible fall of ground accidents. However, often it is neither practical nor economical to inspect vast areas of mine workings with limited personnel, and the S-pillar approach has limitations due to the tributary area theory assumption and does not consider the relative location of geological structures with respect to pillars or that multiple joint sets may intersecting a pillar. The objective of this project is to develop a warning system for old workings in underground stone mines with an autonomous robotic system that is comprised of an UAV tethered to an UGV that provides 3D maps, which are then used as an input for assessment of pillar damage, and accompanying integrated hazard mapping (Stability-Mapping) / boundary element modeling (LaModel) approach for the assessment of stone mine pillar stability. Successful deployment of the autonomous robotic system, as well as the use of the resulting monitoring results in hazard assessment, is expected to reduce injuries of underground stone mine workers. The techniques developed in this research would be easily adaptable to all underground metal/nonmetal mining sectors.

## **Background**

In the US, the S-Pillar program was developed to assist in the design of stable pillars for room-and-pillar workings in underground stone mines (Esterhuizen et al, 2011). Esterhuizen et al. collected operational information and pillar performances from 34 different stone mines in the Eastern and Midwestern United States. They classified a total of 18 cases of individual pillars as a failure and assessed each of the failed pillars visually. Modes of pillar instabilities were categorized as crushing or structure-controlled failure. Esterhuizen et al. indicated that rib spalling and the emergence of an hourglass shape is the indicator of crushing failure (Figure 1a). They sub-characterized structure-controlled failures as pillars intersected by large discontinuities (Figure 1b) and pillars with weak bedding planes (Figure 1c). It is important to note that all these pillar failure modes would be detected by 3D mapping (Presto et al., 2015).



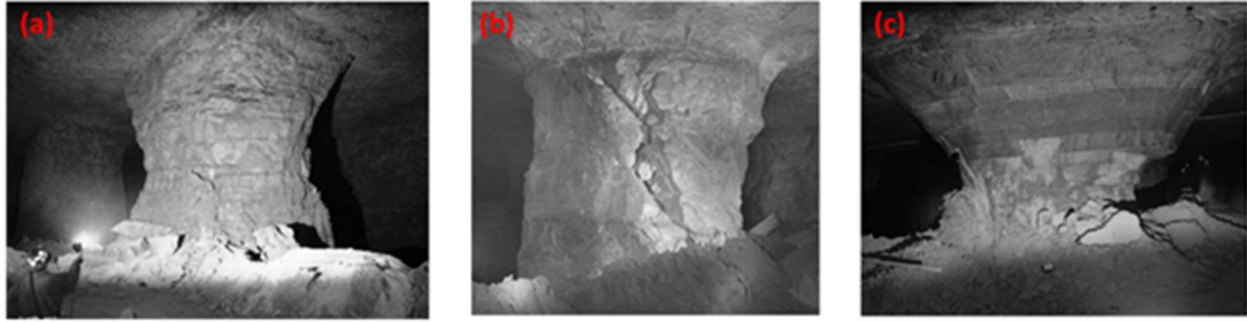


**Figure 2.1.** Failure modes a) crushing failure, b) pillar intersected by large discontinuity, c) pillar with weak bedding planes (after, Esterhuizen et al., 2011).

Later, by completing a comprehensive numerical modeling work to understand pillar behavior within the consideration of brittle rock spalling, large and angular discontinuities, weak bedding bands, floor benching, and length of pillar, Esterhuizen et al. established a base pillar strength equation governing stone mines in the US (Equation 2.1).

$$\sigma_p = k \frac{w^{0.3}}{h^{0.59}} \quad (2.1)$$

where;

$\sigma_p$  = Pillar Strength (psi or MPa).

UCS = Uniaxial Compressive Strength.

$k = 0.65 \times \text{UCS (for psi)} \mid 0.92 \times \text{UCS (for MPa)}$ .

$w$  = width of the pillar (ft or m).

$h$  = height of the pillar (ft or m).

Esterhuizen et al. (2011) also studied the large and angular discontinuity effects on pillar strength. Large and angular discontinuity is defined as a joint system passing through the pillar from floor to roof with different dip angles. Later, they introduced the “large discontinuity factor” (LDF) (Equation 2.2) in addition to the base equation (Equation 1) to reduce the strength of pillars with large and angular joints in their matrix. The large discontinuity factor consists of two different parameters: the discontinuity dip factor (DDF) and fracture frequency (FF). Finally, Esterhuizen et al. (2011) published Equation 2.3 to estimate stone mine pillar strength in the Eastern and Midwestern US.

$$LDF = 1 - DDF \cdot FF \quad (2.2)$$

$$\sigma_p = k \cdot LDF \cdot \frac{w^{0.3}}{h^{0.59}} \quad (2.3)$$

S-Pillar software assesses the stability of stone mine pillars by calculating the factor of safety and comparing it with the historical data on pillar performances. The factor of safety is the ratio of the pillar strength, calculated using the empirical strength equation (Equation 2.3), to the pillar stress. S-Pillar uses the tributary area method to calculate the stress on the pillars, and this method assumes that the full weight of the overburden is uniformly distributed among the pillars. Moreover, S-Pillar calculates the pillar load as the maximum depth over the pillar layout, and the stress calculation is only truly valid if the areas of the mine use regular-sized pillars (Esterhuizen

et al., 2011). Esterhuizen et al. recommended that the pillar safety factor must be at least 1.8 and the width-to-height ratio of the pillar must be larger than 0.8 to achieve a successful pillar layout.

Since the development of S-Pillar, there has been a major effort to use laser scanning and photogrammetry methods to map geological structures, characterize the rock mass, monitor rock mass deformation and develop discrete fracture networks for advanced distinct model analyses (Slaker, 2015; Slaker et al., 2016; Monsalve et al., 2018). Preston et al., (2015) used a time-lapse photogrammetric survey to measure hard rock mine pillar volumes in different time intervals to measure pillar damage as the depth of failure. They surveyed 19 pillars over 230 days. Later, they used the displacement discontinuity (DDA) approach of Roberts et al. (2007) to estimate the pillar strength from the back analysis of damage progression. NIOSH intramural research project concentrated on building a framework for expanding pillar design criteria used in S-Pillar software to multiple-seam, deep, and dipping mining environments (NIOSH, 2022). In this project, the NIOSH team used light detection and ranging (LIDAR) and photogrammetry methods to map case study mines and geological structures, characterize the rock mass, monitor rock mass deformation, and develop numerical models that simulate pillar responses and failure mechanisms. Virginia Polytechnic Institute and State University (VT) research, funded by NIOSH, focused on the application of LIDAR and photogrammetry for mapping discontinuities in case study mines and generating discrete fracture networks for stochastic discrete element simulation of stone mine pillars (Bishop, 2022). The major contribution of the VT research has been the demonstration of the successful applications of the UAVs to mapping and inspection of underground workings both with manual piloting and autonomously (Bishop, 2022).

### **Specific Aims and Research Objectives**

West Virginia University (WVU) Mining Engineering and Robotics researchers performed a three-year study to develop the proof of concept of a framework for a warning system for old workings in underground stone mines with an autonomous robotic system that is comprised of an UAV tethered to an UGV that provides 3D maps, which are then used as an input for assessment of pillar damage, and accompanying integrated hazard mapping (Stability-Mapping) / boundary element modeling (LaModel) approach for the assessment of stone mine pillar stability. The following research specific aims and research objectives were undertaken to achieve the research goal:

**Specific Aim 1:** Develop a robotic system that consists of an UAV tethered to an UGV for stone mine inspection.

- *Research Objective 1.1:* Integrate sensing, navigation, and mapping on cooperative UAV/UGV systems.
- *Research Objective 1.2:* Develop a tethering system between the UGV and UAV for power transmission and autonomous landing.
- *Research Objective 1.3:* Integrate high-level autonomy and planning on the robotic system.

**Specific Aim 2:** Develop a framework for integrating hazard mapping (Stability-Mapping) and boundary element modeling (LaModel) for the assessment of pillar stability from remotely obtained 3D mapping.

- *Research Objective 2.1:* Develop stone mine pillar module for stability mapping.

- Research Objective 2.2: To develop an approach for time-dependent strength degradation adjustment for pillar strength equation used in S-Pillar.

**Specific Aim 3:** Test and verify the integrated autonomous robotics and Stability-Mapping based underground stone mine hazard detection and early warning system in the field.

- Research Objective 3.1: To test reliability of integrated autonomous robotics system in underground environment and to verify integrated autonomous robotic system measurements.

### 3.0 Research Approach:

In mining, hazards causing fall of ground related accidents generally develop with time. The development of hazards depends on factors like geology, excavation geometry, in situ stress state, and mining-induced stresses. Generally, ground control design methods cannot consider all of these factors due to the difficulty of accurately and economically identifying these spatially and temporally changing factors throughout a mine. In addition, there isn't any method accepted by the mining industry available to quantify the time-dependent stability of stone, metal or coal mine. Generally, engineers estimate average conditions based on available information on geology, rock mass mechanical properties, and mine geometry to select input values for existing design tools to minimize the occurrence of possible hazards. Time-dependent degradation is typically addressed with a suitable safety factor. Mine Safety and Health Administration (MSHA) indicated that there is not any design method available to predict when, or even whether, a particular pillar or group of pillars would collapse, but it is possible to recognize hazards that might increase the likelihood of these massive collapses (MSHA, 2021). MSHA listed the following hazards that might cause pillar collapses: (i) irregular undersized pillars due to surveying or blasting errors, and (ii) ignoring or not realizing geological features (joints, weak bedding planes etc.) on the pillars that might reduce pillar stability or induce rib falls (MSHA, 2021).

Therefore, proper inspection of the ribs, roofs, and pillars to identify deteriorating ground conditions; and rapid response to prevent further deterioration would protect miners from possible fall of ground accidents. However, often it is neither practical nor economical to inspect vast areas of mine workings with limited personnel. In our approach, we developed a technology that would allow mine operators to perform inspections remotely and autonomously. The research approach consisted of a development phase (Specific Aims 1 and 2) and a testing/verification phase (Specific Aim 3). During the development phase: 1) The autonomous robotic system that consists of UAV and UGV was developed and 2) The framework for integrating hazard mapping (Stability-Mapping) and boundary element modeling (LaModel) for assessing stone mine pillar stability was developed. During the testing/verification phase, the autonomous robotic system was deployed and tested in different underground mining environments and, the integrated hazard mapping / BEM framework was applied to a field case study.

#### **Specific Aim 1: Develop a robotic system that consists of an UAV tethered to an UGV for stone mine inspection.**

In this section of the report, we describe the development of the autonomous robotic system shown in Figure 3.1, composed of an unmanned ground vehicle (UGV), called Rhino, and a tethered unmanned aerial vehicle (TUAV), known as Oxpecker. The system was designed to autonomously map underground stone mine entries to provide an accurate 3D map of stone mine pillars. When in operation, the system records 3D point-cloud data of pillars to support time-lapse hazard mapping and pillar stability analysis. Because stone mines have pillars varying from approximately 5 to 22 m in height, sensors on the UGV alone cannot obtain high-resolution data of the entire pillar, thus justifying the deployment of the TUAV each time a pillar must be surveyed. As the UAV batteries are carried by the UGV and the tether provides relative measurements between the vehicles, the proposed configuration not only increases the battery capacity of the drone but also

allows drone navigation and landing without vision. We developed the robotic stone mine pillar inspection system through three specific research objectives.

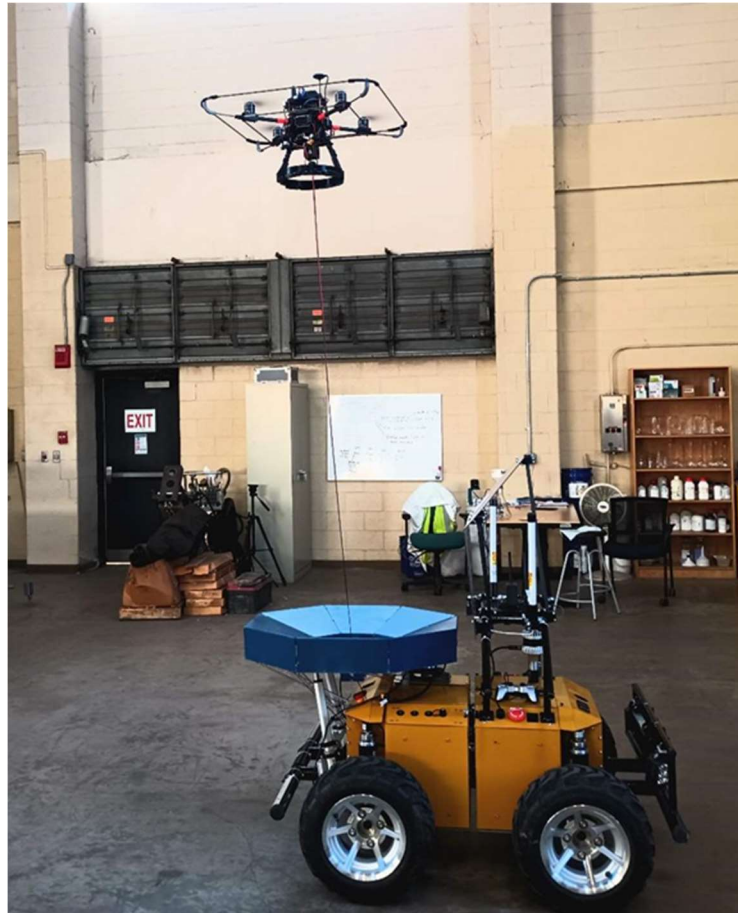


***Figure 3.1.** Rhino, the unmanned ground vehicle (UGV), is a mobile robot in yellow and blue. Oxpecker, the tethered unmanned aerial vehicle (TUAV), is the drone flying above Rhino. Rhino and Oxpecker form a cooperative robotic system for underground mine mapping.*

**Research Objective 1.1: Integrate sensing, navigation, and mapping on a cooperative UAV/UGV systems.**

The Rhino robot was developed to assist in the inspection and monitoring of underground stone mines, the objectives of the UGV are to:

- Traverse the mine terrain reliably and autonomously;
- Avoid obstacles and untraversable areas;
- Create high-resolution 3D maps of the mine and columns;
- Operate for extended periods of time of at least six hours per day;
- Support the tethered drone system.

**Task 1.1.1: Develop the UGV for the stone mine pillar inspection.**

**UGV Mechanical Overview:** In order for the UGV to operate for extended periods of time of at least 6 hours, the system must carry batteries that will be able to provide power to all the electronics

and sensors. Due to the limitations in the current energy density of batteries (e.g., around 295Wh/kg for Lithium-Ion)[Li et al., 2017], the weight of the battery was the main constraint when designing a robot that is able to operate continuously for an extended period of time. To successfully complete the required tasks in the mine, a wheeled design was chosen due to its efficiency with four large wheels to allow for the traversal of the rugged terrain. A skid-steering driving configuration is used due to its simplicity, and ease of service.

A split-body chassis was chosen because it allows the wheels to come into contact with the ground to provide traction on uneven terrain. A 300mm diameter bearing connects both halves instrumented along the body axis of the robot. For ease of manufacturing, the chassis was designed to prioritize the use of waterjet parts and minimize the number of Computerized Numerical Control (CNC) machined parts.



**Figure 3.2.** *Rhino robot rendering, including sensors, landing platform and the drone.*

Lithium Iron Phosphate (LiFePO<sub>4</sub>) batteries were chosen due to their longer life span, safety, cycle time, and high capacity. Ten 12.8V batteries with a combined energy of 420 Ah and a combined weight of 58kg are used to power the electronics and sensors. A render of the robot is shown in Figure 3.2. The robot is divided into two parts: the front chassis and the back chassis. There are six batteries in the back chassis of the robot, with an easy-to-access front panel with a connection to charge the batteries. The front chassis has two side compartments with one side instrumented with electronics required to power the system, while the other compartment contains the computer. In the back chassis, there are six batteries and the winch system for the drone. The drone and its landing platform can be assembled on top of the back chassis. The two side compartments in the back are instrumented with the motor controllers and other auxiliary electronics such as relays, network switch, etc. All the panels and compartments are sealed for insulation for operating inside



the mine environment. A roll cage is mounted on the top of the front chassis of the rover for protecting the chassis as well as for mounting cameras and communication antennas and radios. Front and back bumpers are added for additional safety and for mounting the work lights. The robot's total weight is 190kg and its footprint is 1.52m by 1.15m and has a ground clearance of 0.22m.

**Task 1.1.2:** *Integrate a 3D point-cloud sensor on the UAV system to support dense mapping of the pillars, onboard collision avoidance, and inner-loop control of the UAV.*

**UGV Electronics Overview:** The Rhino robot is instrumented with a set of sensors to enable autonomous operation in underground environments. Figure 3.3 shows an overview of the rover's electronics and sensors. The ZED Stereo Camera and an Ouster OS1-64 LiDAR with 64 channels and a max range of 200m and 45° vertical field of view are used to sense the environment. The Analog Devices ADIS16495 Inertial Measurement Unit (IMU) that has a triaxial digital gyroscope and a triaxial accelerometer and a KVH DSP-1760 single-axis fiber optic gyroscope are used in combination with the exteroceptive sensors to reduce errors in the localization and mapping estimates. In order to obtain accurate localization and mapping estimates, the LiDAR is extrinsically calibrated with an IMU to track the motion distortion in each LiDAR scan. To make the transformation between the LiDAR and IMU simple to compute, the robot was designed so that the IMU was mounted below the LiDAR with only a translation offset in the Z-direction. Data is collected and processed onboard the robot using an Intel i7-9700K computer with 32GB of RAM memory and a GTX 1050Ti GPU.

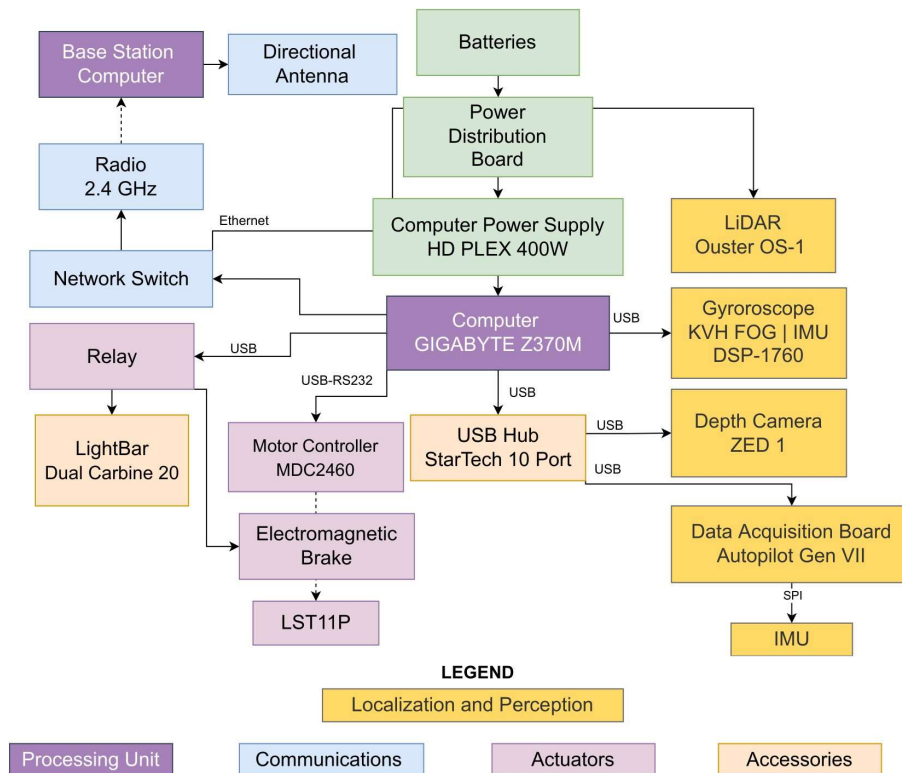


**Figure 3.3.** Diagram showing Rhino's sensors and electronics required to complete the autonomous navigation and mapping tasks.

Due to the high current demand for the motors and drone, and the sensitivity of the sensors and electronics such as the computers, the power distribution of the robot is split into three independent



modules: the electronics and sensors, the drone, and the drive motors. Four batteries are dedicated to powering the motors, which is an independent system due to the large current spikes and back-EMF. Two batteries are assembled in series 25.6V to power the motors on each side of the robot. For the modularity of the drone system, there are four batteries dedicated to the UAV system, since the UGV and UAV operate independently in most situations. This system uses one 12.8 V battery for powering the winch motor, linear actuators and electronics and 38.4V to power the UAV. The rest of the electronics and sensors onboard are powered by the other two 12.8V batteries in series that are connected to a custom power distribution board that is able to supply a wide range of voltages from 3.3V to 24V. The batteries are assembled in a configuration that allows them to be easily charged with a single connector in the front compartment of the robot.

Rhino's drive motors are four LST11P 24 VDC brushed motors with a gear reduction of 45.5:1 and electromagnetic brakes. Two 2-Channel Roboteq MDC2460 motor controllers are used to control the motors in a skid steer configuration and provide up to 50A maximum current and 10A continuous current per motor. An additional circuit was designed to allow the motors to draw as much current as it needs to operate and protect the rest of the system from high voltage transients caused by the back-EMF due to the high inertia of Rhino. The circuit involves adding a relay, fuse, fly-back diode, an emergency-stop (e-stop) button, and an In-Rush current limiter to the motor's power module. The In-Rush Current limiter protects the motor controllers from the large impulse of current when the robot is switched on. The relay and e-stop act as a switch to power the motors on and off and also allows power to the motors to be cut off in emergency situations. On the software side of the driving configuration, the acceleration is linear and limited to  $0.5m/s^2$  and the Proportional-Integral (PI) feedback controller has a limitation on the maximum integral value ensuring smoother driving. In order to control the brakes during Rhino's missions and for safety, the electromagnetic brakes are interfaced with a relay that allows user input.

Rhino is instrumented with Dual Carbine light bars that are controlled by USB relays for improved visibility during underground operations. The robot has four LED indicators on its side that provide visual information on whether it is in autonomous or teleoperation mode and the status of the brakes.

The goal of Rhino's communication system is to enable the transmission of data between the robot and a base station computer when in direct line of sight. Data such as the orientation of the system, camera feedback during teleoperation mode, state of the brakes, the current draw of the motors, localization pose estimates, etc. The robot communication system consists of two omnidirectional antennas with a 2.4GHz and 900MHz frequency radio system by Ubiquiti interfaced with the system via a network switch.

A base station computer with high-gain directional antennas is used to communicate with the robot. The communication link transmits crucial information such as health status and sensor data; allows for joystick teleoperation from the base and for emergency braking; and is also used to deploy and monitor the robot on autonomous missions.

**Research Objective 1.2: Develop a tethering system between the UGV and UAV for power transmission and autonomous landing.**

In the system developed in this project, a set of high-energy density batteries was added to Rhino's payload to achieve long-endurance flights of Oxpecker. The batteries can deliver an average power of 570 W (i.e., 38 V at 15 A) to the TUAV through a power cable. Two other subsystems were

designed to integrate and handle the tether. First, a tether management subsystem was developed to control the tension (i.e., force) on the cable, keeping it in suspension and preventing it from touching the ground. A second subsystem consists of a set of sensors used by the drone for localization and landing. These sensors measure the length of the tether and tether angles at both endpoints (i.e., the UAV and the landing platform on the UGV). Finally, a landing platform was designed to hold the UAV while the UGV moves inside the mine. The next subsections describe in detail all the systems developed to allow the interaction between the UGV and the UAV.

***Task 1.2.1:*** *Develop a tethered power system between the UAV and UGV.*

**Mission Requirements and Design Decisions:** The main requirement of this project is that the pillars of the mine, the height of which may vary from approximately 5 to 22 m, are autonomously and completely scanned with a LiDAR or camera so that a 3D map can be constructed and used for hazard assessment. Although a standard UAV could be applied to this task, its short flight time would not be practical for mines with hundreds of pillars. On the other hand, a UGV alone could not scan a single pillar completely unless it is equipped with a telescopic device/manipulator that would be able to move the sensors along the pillar until its top. After considering this solution as cumbersome and costly, our team then considered the use of a drone, which would work in tandem with the UGV.

The mission requirements for this drone are listed as follows:

- Able to operate for several hours without human intervention;
- Able to carry mapping and surveying sensors, including LiDARs and cameras;
- Able to precisely land on the UGV before moving from one pillar to the next.

These requirements lead the research team to design:

- A tether-powered quadrotor with enough payload capacity to carry localization and 3D mapping sensors, and the weight of the released power cable;
- A tethering system that manages the cable release and retraction and that assists the drone localization and landing by measuring relevant variables, such as tether angles and tether length;
- A self-leveling landing platform that compensates for the roll and pitch of the ground vehicle and assists in drone landing.

The rest of this section overviews the design concept of the tethered-powered UAV. The goal of this design was to develop a drone that can be powered by a cable and has enough payload capacity to carry the required instruments and the tether. The main challenge of designing such a system was working on the trade-offs of transmitting such high power over a long cable. Our solution required a combined selection of frame, powertrain, and cable. To complete the design, we selected the flight controller, companion computer, and sensor suite onboard the drone. A schematic overview of the hardware setup can be seen in Figure 3.4. Table 9.1 (in the appendix) lists the components required to assemble Oxpecker along with their manufacturers, models, and other relevant specifications. The most relevant components are discussed next.

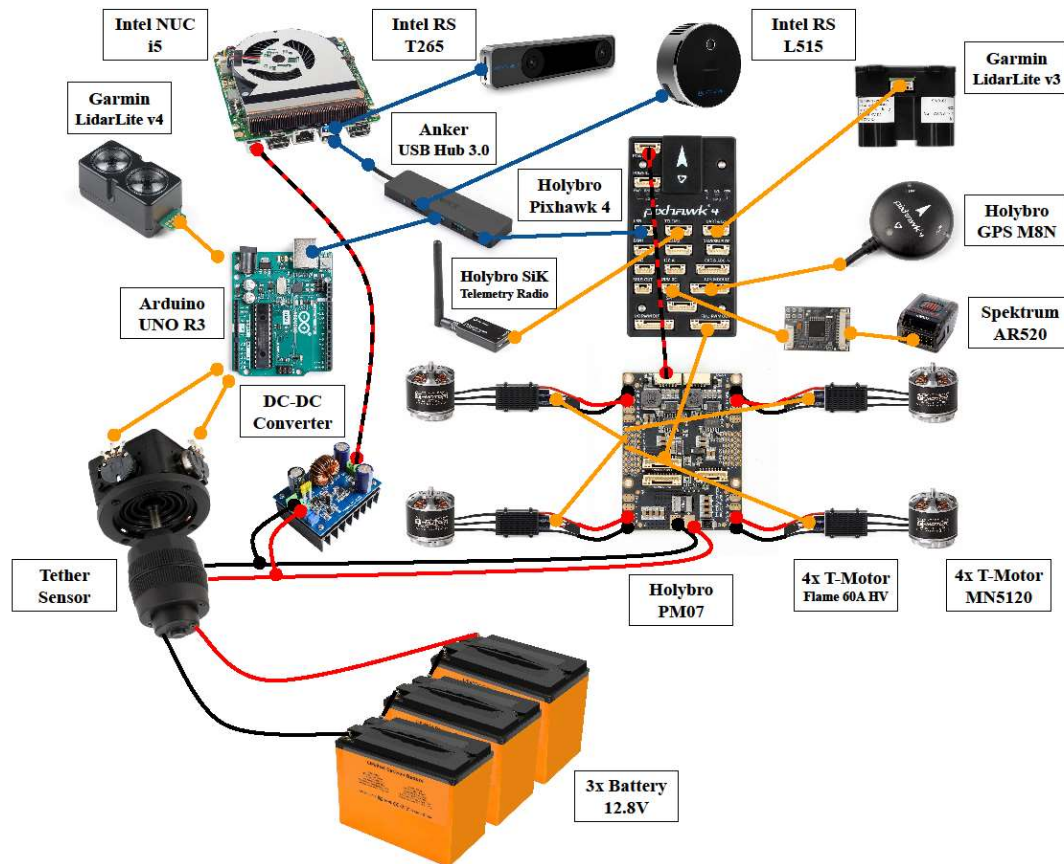


**Figure 3.4.** Schematic overview of Oxpecker's electronics. Except for the battery pack, all other components are carried onboard by the drone.

Cable Specification: An electrical cable has its resistance given by  $R = \rho L/A$ , where  $L$  is the cable length,  $\rho$  is the material resistivity, and  $A$  is the cross-sectional area. Therefore, the longer the cable, the higher the resistance. In the presence of current ( $i$ ) the voltage drop ( $\Delta v$ ) along the cable is ruled by  $\Delta v = Ri$ . The current and voltage drop directly translate into energy loss by Joule's law (heat dissipation), which states that the power converted from electrical energy to thermal energy is given by  $P = \Delta v \cdot i = (\rho L/A) \cdot i^2$ . One way to reduce the resistance, and thus the power loss, is to increase the cross-sectional area of the conductor. However, this approach contributes to increasing the weight of the cable to be suspended by the drone. We could also reduce the length of the cable, which would limit the reach of the drone. A feasible alternative to minimize the power loss without shortening the cable is then raising the voltage delivered to the drone, thus reducing the current flowing through the tether for the same power consumption. As the power loss on the cable scales with the square of the current, this would be the best approach to take. Additionally, smaller currents permit the use of conductors with reduced cross-sectional areas, which contributes to decreasing the cable's linear weight. Many commercial applications prefer to transmit power at a very high voltage (e.g., 400 V) and include a voltage converter on the UAV to reduce the voltage level required by the motors and flight controller. However, as the payload is a critical constraint in our design and power conversion devices are usually not lightweight, we decided to increase the voltage as much as possible to connect it directly to the power management board without a DC-DC converter.

Given an estimated power-to-weight ratio of  $\approx 150$  W/kg which is consistent with the specific power estimates of 200 W/kg for agile quadrotors shown in (Mulgaonkar et al., 2014) and a maximum hovering weight of  $\approx 4$  kg, we selected the cable for an expected power consumption of 600 W on the drone. We then chose to use three 12.8 V batteries connected in series to power the UAV. Given the open-circuit battery voltage of  $v_b = 3 \times 12.8 = 38.4$  V and the required power of 600 W, an initial current estimate on the cable without assuming any voltage drop would be  $\approx 15.6$  A. By assuming a 16 AWG stranded copper cable with resistivity  $0.0132 \Omega/\text{m}$ , which has adequate flexibility for our application, and also considering the additional resistance of  $0.15 \Omega$  from connectors and other parts of the circuit, we can iterate the voltage drop until convergence is reached. By applying this process, we compared different tether lengths and opted for a 15 m-long cable, which is sufficient for proof of concept demonstration. The estimated voltage drop in this cable is  $\Delta v \approx 6.6$  V when the current is 18.8 A. This yields a power loss of  $\approx 123.5$  W along the tether.

The powertrain of the quadcopter, specifically, electronic speed controllers (ESCs), motors, and propellers, were chosen to handle high voltage (38.4 V) from the tether and provide enough thrust to match the maximum hovering weight of the drone ( $\approx 4$  kg). We considered that the system would work around the 8S voltage rating after accounting for the losses on the cable and expected power consumption for the drone ( $\approx 600$  W). The power delivered was considered to be approximately constant during its mission, as the drone is not expected to be agile and will work in near-hover flight conditions all the time. The selected motor was the T-MOTOR MN3520 (rated 4S-8S) with a T-MOTOR  $12 \times 4$  carbon fiber propeller, using a T-MOTOR FLAME 60A HV ESC (rated for 6S-12S). In our tests, we measured the voltage ( $\approx 33.5$  V) and current ( $\approx 18.5$  A) delivered to Oxpecker during flight, confirming the expected power consumption ( $\approx 620$  W) and validating the selection of the powertrain.

Frame Selection: The frame is the structure that holds all the components of a quadrotor together. It needs to be designed to be strong but also lightweight. The lighter a frame is, the more payload the drone can carry. A great way to optimize the airframe is to select carbon fiber frames. We chose an easy-access, commercial frame for this aerial system, the Holybro X500 Frame Kit. This frame was selected because it is easy to assemble and is capable of supporting the estimated maximum takeoff weight for this drone (4 kg). Adaptations have been made to install the heavier, higher voltage motors selected (e.g., 3D printing reinforced clamps that hold the arms and the motors).

Flight Controller Selection: A review of flight controller options in (Foehn et al., 2022), shows that, typically, research groups rely on Pixhawk-PX4, Parrot, or DJI low-level controllers. They are mostly used as black boxes, but they differ in how much authority is given to change the controllers. The flight controller unit (FCU) selected for the drone was the Pixhawk 4, which is optimized to run PX4, an open-source flight control software for UAVs and other unmanned vehicles. It provides all the main sensing capabilities required by a UAV, such as an inertial measurement unit (IMU) and barometer, and ports to integrate several others directly. For Oxpecker, we integrated a U-Blox Neo-M8N GPS/GLONASS receiver to provide a compass, a SiK Telemetry Radio V3 for monitoring and debugging purposes using QGroundControl, a Garmin LidarLite v3 ranging sensor to provide height measurements, and a Spektrum AR620 receiver to provide manual radio control. A large community also supports the Pixhawk, and it can easily be integrated with a companion computer through the MAVLINK (Koubâa et al., 2019) communication protocol.



**Companion Computer Selection:** Given that the Pixhawk 4 has very limited onboard computing capability, a companion computer is required to run custom software for the drone and allow for data collection (i.e., images and point clouds). There are many options for companion computers, and the most popular are listed in (Foehn et al., 2022). When no GPU is required, the Intel NUC family, the Udoo family, and the Raspberry family of computers are the most popular options. From our previous experience, fully autonomous operation, including localization and mapping, is possible with an embedded computer with extended RAM and storage. Originally, the Udoo X86 II Ultra with an Intel® Pentium® N3710 (2.56 GHz, 8 Gb RAM, 32 GB eMMC Storage, 150 g, 6 W) was tested due to its lower cost. Moreover, this computer also contains an Arduino Leonardo-compatible platform embedded on the same board, which facilitates the integration of I2C and analog sensors, such as the potentiometers we use to measure tether angles. However, although enough to perform basic functions (landing, wall following, etc.) and to save data, this computer was not powerful enough to run simultaneous localization and mapping (SLAM) algorithms online. Subsequently, we opted to substitute this embedded computer with an Intel® NUC 11 with an Intel® Core™ i5-1135G7 processor (8M cache, up to 4.20 GHz) and an external Arduino UNO R3 for low-level sensor communication. Additionally, we included a 2TB SSD card for storing the mapping data. The custom software running in this computer was developed using the Robot Operating System (ROS) and is described further in this report. The communication between the companion computer and the Pixhawk was done using the MAVROS package (Ermakov, 2020). A USB hub was connected to the computer to allow for several USB devices: WiFi antenna, notification light, Arduino, Pixhawk, stereo camera, and LiDAR.

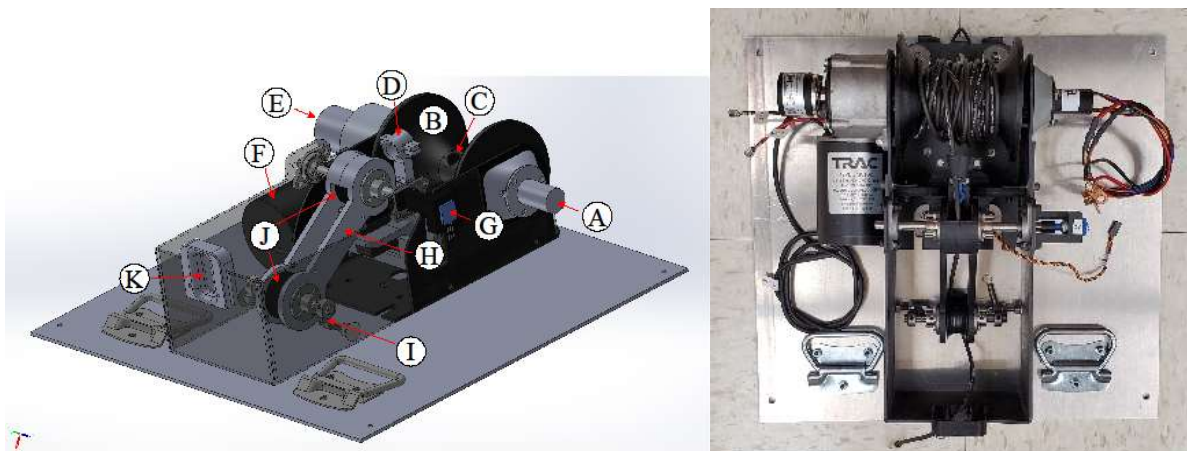


**Figure 3.5.** Cable management system. On the left is a three-dimensional CAD model of the system highlighting the slip ring device (A), which allows the power to be transmitted from its external fixed frame to the internal rotating frame physically attached to a custom 3D printed spool (B) where the power cable is stored. The cable goes inside the spool's axis, comes out from (C), and passes through a funnel-like device (D). This device is driven by a servomotor that moves from side to side to evenly distribute the cable over the spool. The length of the tether is measured by a digital rotary encoder (E) when the DC motor (F) is turning. The tether tension is measured by a potentiometer (G) installed in the axis of a pivoted lever arm (H), which supports a pair of pulleys (J) where the cable can slide off. A spring (I) is used to load the lever arm. The cable accesses the system through the outlet (K). On the right image we see the real-world implementation of the designed system.

**Tethering System development:** The tethering system is composed of (1) a cable management system, responsible for controlling the tether tension by reeling the tether in or out, depending on

the measured tension; (2) a tensiometer for measuring the tether tension; and (3) two tether angle sensors. Tension is measured by a mechanism composed of a pivoted spring-load lever arm with conveying pulleys where the tether slides off, as shown in Figure 3.5. A mechanism composed of a servomotor and a lever arm is used to evenly distribute the cable on the reel when turning, as depicted in Figure 3.5. The lever arm moves synchronously with the reel's spin, which can be properly adjusted in firmware. The control system is accomplished by a digital proportional-integral-derivative (PID) controller implemented in an Arduino microcontroller. In order to deliver power to the UAV through the cable, a slip ring is used to convey electrical power through the reel. The tethering system is assembled in a compartment located at the rear of the ground robot.

Two tether angle sensors were designed in-house. A joystick-like device was adapted (see Figure 3.6 on the right) for the sensor at the drone endpoint of the tether. Because the axes of rotation for this device are co-planar, the measurements of its potentiometers can be directly translated to the tether's azimuth and elevation angles by converting the voltage read by a microcontroller analog-to-digital converter (ADC) port and applying a calibration curve. A similar approach was used for the sensor at the platform endpoint of the tether, where we have the custom design shown in Figure 3.6 on the left. To obtain the tether azimuth and elevation angles for this device, a kinematic chain system needs to be solved to obtain a frame transformation from the platform frame to the tether endpoint frame. More details about this transformation can be found in our published paper (Rocamora et al., 2023).

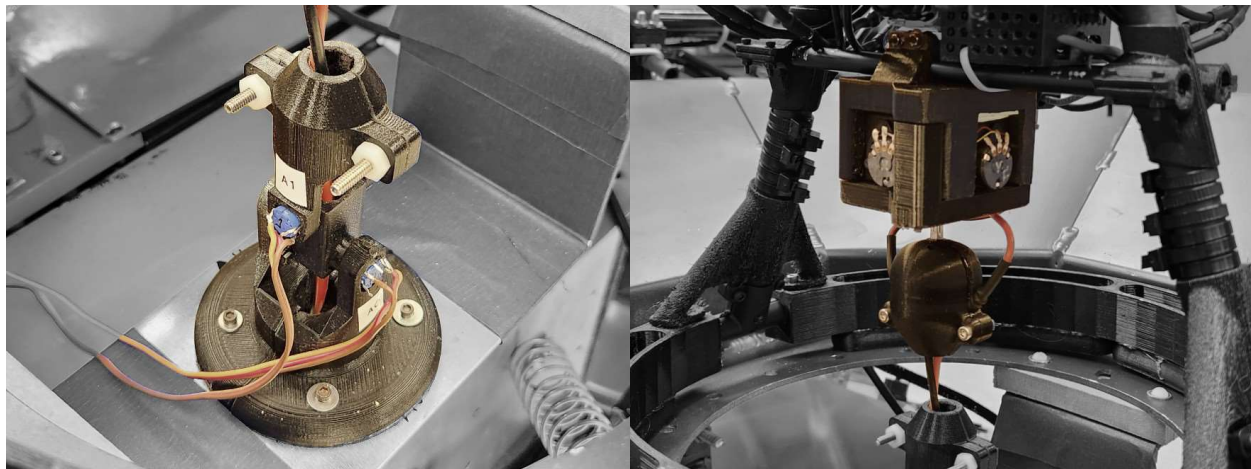


**Figure 3.6.** Tether angle sensors: The figure on the left shows a kinematic chain with two degrees of freedom designed to measure azimuth and elevation angles at the platform; The figure on the right shows an analog joystick adapted to obtain the same angles at the drone side.

**Task 1.2.2:** Develop an autonomous landing system for the UAV on the UGV.

**Self-Leveling Landing Platform System:** A self-leveling platform was included in the UGV to provide a stable, level surface for the UAV to land on. In our design, we used a tri-axial accelerometer and two linear actuators to adjust the platform attitude and maintain it horizontally leveled, even when the UGV is located on uneven terrain or a slope, as shown in Figure 3.7. This platform helps to ensure that the UAV lands safely and precisely without tipping over or damaging itself or its surroundings.



**Figure 3.7.** Self-leveling landing platform compensates for the angles of the UGV by increasing the strokes of two linear actuators.

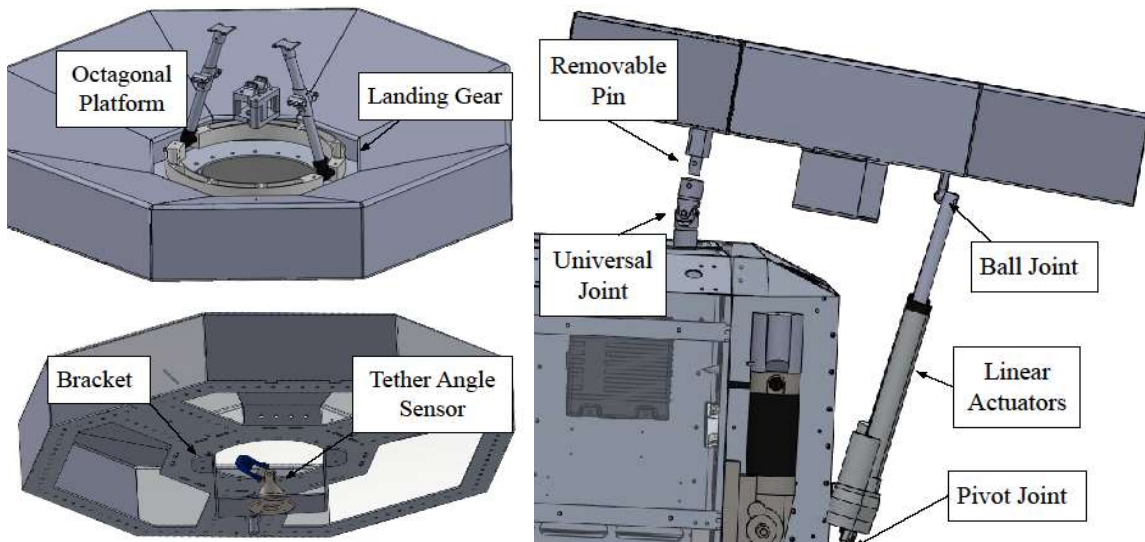


**Figure 3.8.** The shape of the landing platform viewed from above and below and the shape of the landing gear that fits in a depression located in the center of the platform (left); On the right is the side view of the mounting points of the platform.

The landing platform was designed with an octagonal shape and a central depression to serve as a passive positioning mechanism and to securely hold the UAV in place when the UGV moves, as illustrated in Figure 3.8. On the UAV side, a landing gear was designed to match the depression in the landing platform. Its circular shape allows the UAV to land without any orientation



constraints. This design enables the platform to function effectively as a landing and docking station for the UAV. A bracket to hold the tether angle sensor was mounted below the platform in the center of the depression. The octagonal platform is connected to three points that are physically attached to two Progressive Automations' PA-14P 12-inch stroke linear actuators and a universal joint, as illustrated in Figure 3.8. As expected, the point representing the fixation to the universal joint does not translate and only rotates. The two points representing the fixation to the linear actuators can translate and rotate when the linear actuators increase or decrease their stroke. The displacement of these two points allows for two possible rotation angles of the platform. If both points move in opposite directions with respect to the horizontal plane, the deck rolls around its x-axis. If the points move in the same direction, the platform pitches around its y-axis. Therefore, with a combination of these two movements, it is possible to adjust the roll and pitch angles of the platform.

To automatically control the platform's attitude, a closed-loop control system was designed using zero roll and pitch angles as setpoints. The controller chosen was the discrete PID control due to its ease of implementation and tuning process. Assuming that the UGV is static and that the only acceleration applied to the system is gravity, the platform attitude is estimated by finding the Euler angles using accelerometers fixed to the platform. Details of the angle computation can be found in our published paper (Rocamora et al., 2023).

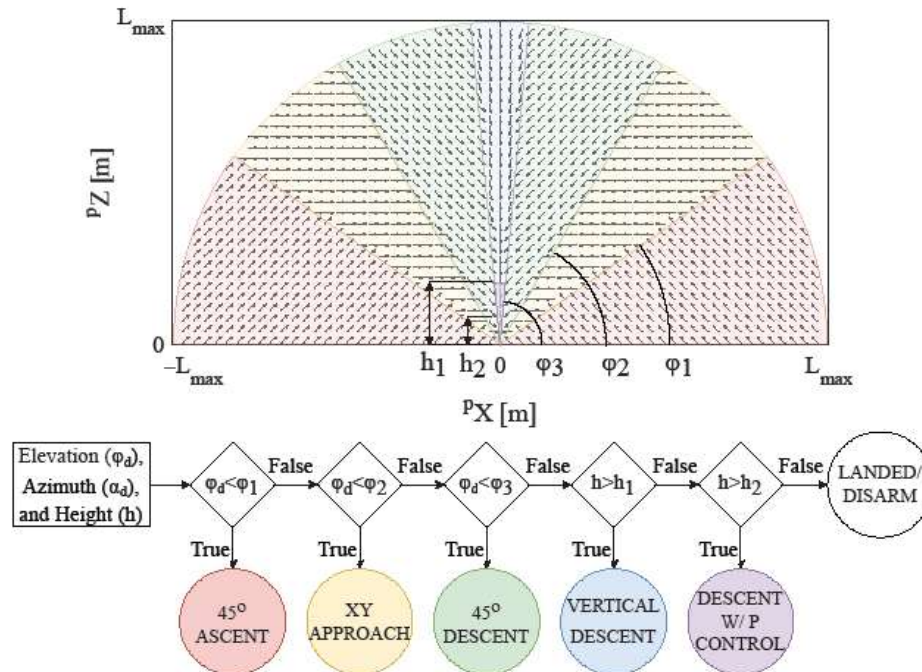


**Figure 3.9.** Proposed tether-guided landing approach. The vector field on top shows the direction of movement on the  $XZ$  plane (in the platform's coordinate frame), limited by the maximum tether length,  $L_{max}$ . The complete 3D vector field can be obtained by rotating this field around the  $z$ -axis. As shown in the flowchart, the vector field, although represented in the workspace, is constructed only based on the drone elevation ( $\phi_d$ ) and azimuth ( $\alpha_d$ ) angles, and the height of the vehicle ( $h$ ). Therefore, no localization is necessary. Ideally, the drone follows the actions sequentially until landed: 45° ascent, horizontal approach, 45° descent, vertical descent, and vertical descent with P control. The angles  $\phi_1$ ,  $\phi_2$ , and  $\phi_3$ , and the heights  $h_1$  and  $h_2$  are thresholds that define the transition between different actions.

**Tether-Guided Landing:** For the TUAV to land accurately on the landing platform situated on the UGV, an algorithm based solely on an altimeter (laser range finder onboard the vehicle) and the tether angle sensors on the TUAV was developed. Therefore, our method does not require a precise localization of the UAV to perform a precise landing on the platform. When a landing is happening, this state is communicated to the tethering system to set the tension setpoint to a higher value so that the tether tends to become taut, which is the ideal situation for landings. The landing procedure is illustrated in Figure 3.9. A switched vector field, which represents velocity setpoints given to the low-level controller in the body frame, is used to guide the drone to the landing pad. The transitions in the vector field are obtained from a combination of elevation angle and height, as shown in the flowchart of Figure 3.9.

To summarize the procedure, if the drone is laterally distant enough from the platform, as indicated by a small elevation angle, the flight path obeys the sequence: a 45-degree incline ascent, followed by a horizontal approach, which progresses to a 45-degree descent, ending in a vertical descent. All horizontal movement is directed toward the landing platform. This flight path may shorten, lengthen, or skip one of these actions entirely, depending on how close the TUAV is to the platform, both vertically and horizontally. The transition elevation angles ( $\phi_1, \phi_2, \phi_3$ ) and heights ( $h_1, h_2$ ), as well as the command speeds ( $V$  and  $V_d$ ) are kept as parameters for tuning. Another observation is that, although the proposed solution generates a discontinuous vector field, to avoid steps in the desired velocity given as a setpoint to the drone's velocity controller, we linearly change the setpoint when we switch from one phase to the next.

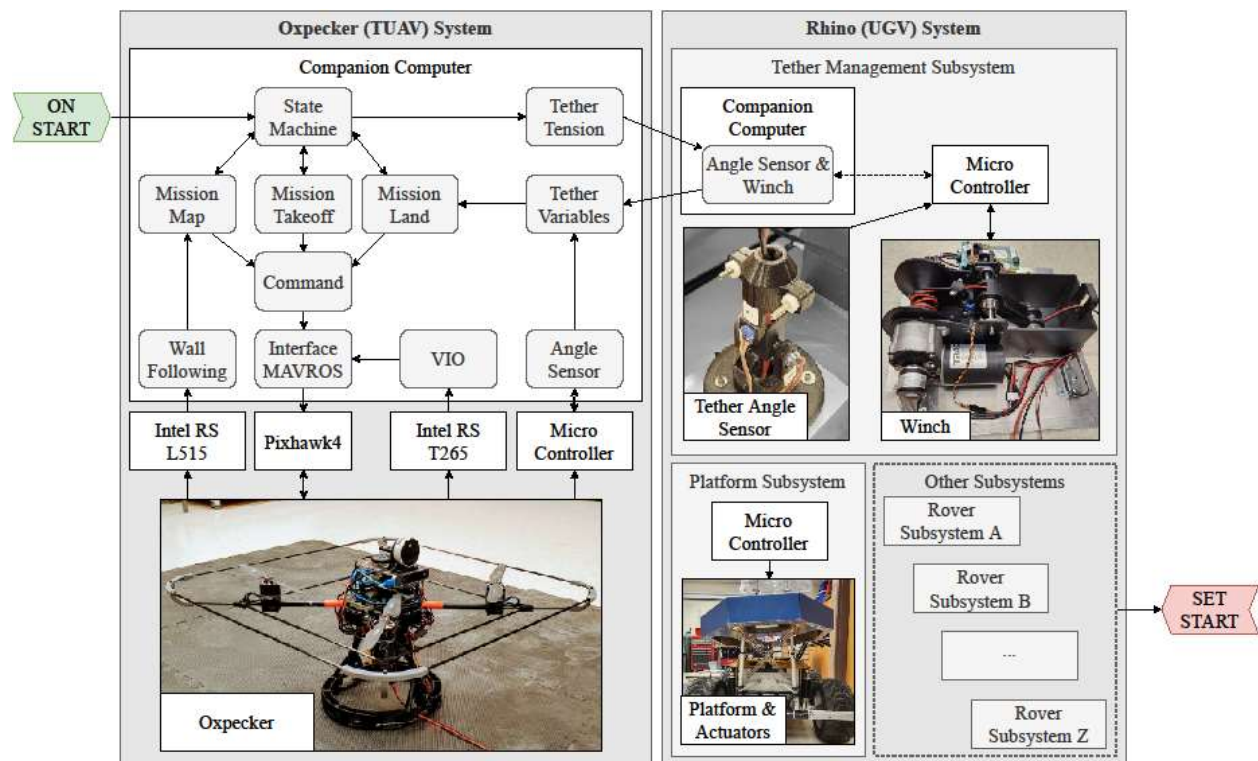


**Figure 3.10.** Cooperative autonomous system framework (UAV-UGV). On the left: a schematic overview of Oxpecker's system. On the right: a schematic overview of Rhino's subsystems related to the drone operation. The rounded gray rectangles represent the ROS nodes developed to operate the autonomous system.

**Software Framework:** For the autonomy framework of the Tethered UAV, we developed a set of ROS nodes to control the drone operation. These nodes were distributed between the computers of the ground and aerial robots. An overview of the UAV and UGV systems and their software is shown in Figure 3.10. The state machine node selects which mission the TUAV will execute by enabling a mission node. This is done by broadcasting the active node through an ROS topic. The mission nodes generate commands that are sent to the commander node, the only node able to communicate with the actual TUAV. This makes this stack generic and independent of the UAV platform. In our experiments, for example, we used a DJI drone by simply changing the command node, which is the only platform-dependent node. For our specific setup, the TUAV commander node is able to control the TUAV using auto-takeoff, auto-landing, target position, and target velocity commands. Other than takeoff, which is usually a native function of the drone's controller, in our application, we split the actions of the TUAV into two missions: mapping and landing. The mapping mission node is responsible for moving towards the pillar and executing a lawnmower pattern to map the pillar surface. The landing mission node is responsible for returning the TUAV to the ground vehicle and landing using only tether information. These two missions will be detailed later in this section.

***Research Objective 1.3: Integrate high-level autonomy and planning on the robotic system.***

The goal of the UGV operation is to enable the robot to drive using waypoint commands inside the mine environment while avoiding obstacles and maintaining a precise state estimation. These commands could be either sent by a user, a task planner algorithm or an exploration-based algorithm. The software is developed in ROS and all core components are running on the robot computer. The software architecture can be divided into four modules: Hardware Interface, State Estimation, Planning, and User Interface, as shown in Figure 3.11.

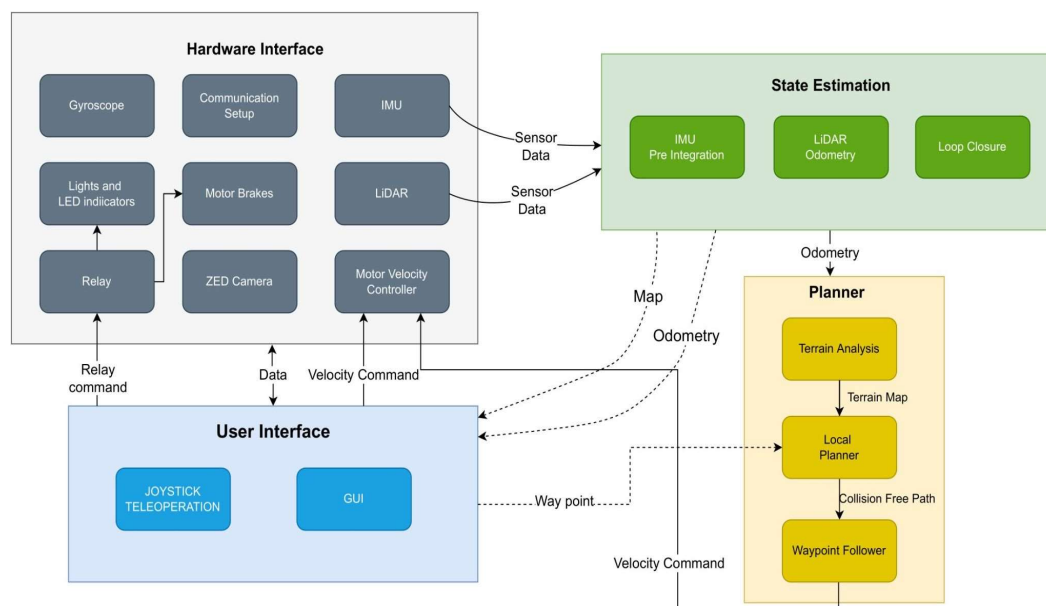


**Figure 3.11.** Systems Software Architecture, where grey is the hardware interface module, green is the state estimation module, yellow the planner module and blue is the user interface module.

**Task 1.3.1:** *Develop hardware interface module.*

The Hardware interface module involves developing software that allows for communication with the sensors and electronics on Rhino which are essential for all the modules. The skid-steering velocity controller algorithm uses command velocities as input at a 50Hz frequency and outputs individual motor commands via a serial interface with the motor controller. This controller also implements a ramp for the velocity commands, limiting the robot acceleration to  $0.5m/s^2$ . The IMU and FOG gyro data are also read using the serial interface at 200Hz and 100Hz respectively. The Ouster LiDAR and the ZED camera data are acquired using the default software provided by the developers. The USB relay software was developed for the activation and deactivation of the spotlights, LED indicators, and electromagnetic brakes. The communication is set up with the robot as the router server and a base station as a client to that computer, allowing for continuous operation even when the connection with the base is lost.

The state estimation module is responsible for providing the robot with reliable localization during autonomous navigation tasks. All the goal commands to the robot are in a global reference frame, therefore having a good state estimation is necessary. The tightly-coupled LiDAR-inertial-odometry via smoothing and mapping (LIO-SAM) SLAM framework (Shan et al., 2020) formulated as a Maximum a Prior (MAP) problem was used since it has demonstrated high accuracy and real-time performance in other environments with similar characteristics such as the tunnel environment in the DARPA subT competition. LIO-SAM is built on a factor graph formulation that allows multisensor input such as IMU, LiDAR, etc., and allows for global optimization. Prior to the IMU data being used by the state estimation module it is calibrated using the Allan Variance method and a complementary filter implemented to infer the orientation estimates. To mitigate issues with pointcloud deskewing due to high acceleration, a nonlinear motion model that receives IMU measurements is used to estimate the motion of the vehicle during the LiDAR scan. The estimated motion from the IMU is also used as an initial guess in the LiDAR odometry optimization and the approximation of IMU biases in the factor graph. For real-time performance and to improve computational complexity, the framework utilizes scan matching at the local scale, as well as the use of selective keyframes. With the formulation being a MAP problem, a Gaussian noise model can be assumed and solved as a linear least-squares problem. The factor graph has nodes that represent the robot state, while the factors in the graph are IMU preintegration, LiDAR odometry, GPS, and loop closure. The state estimation module provides odometry estimates at 10Hz and is also responsible for creating maps of the environment.

**Task 1.3.2:** *Implement autonomous planning for the UGV.*

The Planning module is responsible for receiving  $(x, y, z)$  waypoints commands and returning velocity commands to the robot. It includes a terrain analysis, local planner, and path-following modules. The terrain analysis subscribes to the state estimation odometry and LiDAR and map data and generates a 15m by 15m terrain map around the robot. It uses voxels (Oleynikova et al., 2017) to represent the terrain around the robot and estimates the ground height. Areas that are further than 0.2m away from the ground are considered non-traversable. The map around the robot and the current LiDAR reading are merged to create an updated terrain map around the robot at every timestep at an update rate of 5Hz. The terrain map and the waypoint goal are used as inputs



for the local planner algorithm. The local planner algorithm uses FALCO (Zhang et al.,2020), where motion primitives are pre-computed. The motion primitives around the robot are sampled via the Monte-Carlo method. A path is considered to be valid when every point within the robot's footprint is traversable. The path with maximum likelihood towards the waypoint goal is chosen, while the local planner updates at a rate of 10Hz. The path follower algorithm uses the odometry and the goal path to generate a velocity command that is sent to the motor controller at 20Hz. A lookahead distance of 0.75m is used to follow the selected path. A proportional-integral controller is used to define the linear  $x$  and angular  $z$  velocities at every timestep. The path follower algorithm is the only portion of the robot software where positions are converted and modeled with respect to the robot frame.

The user interface module was developed for ease of deployment of the robot in the underground mine environment. It consists of visualization tools and teleoperation. The user interface is designed to run on the base station computer, with communication routed through both the 900Mhz and the 2.4GHz antennas. A qt-based graphical user interface was developed to provide the user with feedback on the robot's operation. This means monitoring the robot's health including velocity and the current being drawn by each motor, its temperature, battery level, and state estimates. Operators are able to monitor operations via the camera and point cloud, where the quality deteriorates with lower bandwidths. Waypoint goals can be sent by the user using the terminal, and any task planner such as (Tatsch, 2020) or an exploration-based algorithm like (Yamauchi, 1997), (Bircher et al., 2016), (Cao et al., 2021). The teleoperation module is designed to have a higher priority than the velocity commands from the path follower in case of emergencies. The joystick can be used on both the robot and the base station computer, to send velocity commands to the velocity controller, and operate the spotlights. The electromagnetic brakes can only be released with the joystick by the user and it overwrites any motor command, therefore, increasing the safety of robot and operators while testing.

The developed robot software enables the robot to operate autonomously inside the subterranean environment. The state estimation module provides reliable odometry, allowing continuous mapping of the terrain around the robot and analysis of its traversability. This information is used to plan paths that the robot has to follow to reach its goals. The goals that can be set either by the user via its user interface or an autonomous decision-making algorithm such as a task planner or an exploration algorithm.

**Specific Aim 2: Develop a framework for integrating hazard mapping (Stability-Mapping) and boundary element modeling (LaModel) for the assessment of pillar stability from remotely obtained 3D mapping.**

In this section of the report, we describe the development of the stone mine pillar design approach and accompanying software tool that utilizes the empirical stone mine pillar equation, Large Discontinuity Factor (LDF), AutoCAD ObjectARX add-in Integrated Stability Mapping Software (ISMS), and LaModel software to allow stone mine operators to integrate geological structures, irregular pillar layouts, and variable topography into the global and local pillar stability analysis. Figure 3.12 visualizes the framework of the design approach developed in this research.

This research also developed an approach for studying the effect of natural fractures on the mechanical behavior of limestone pillars. This approach was designed to study the time-dependent strength degradation for future research.

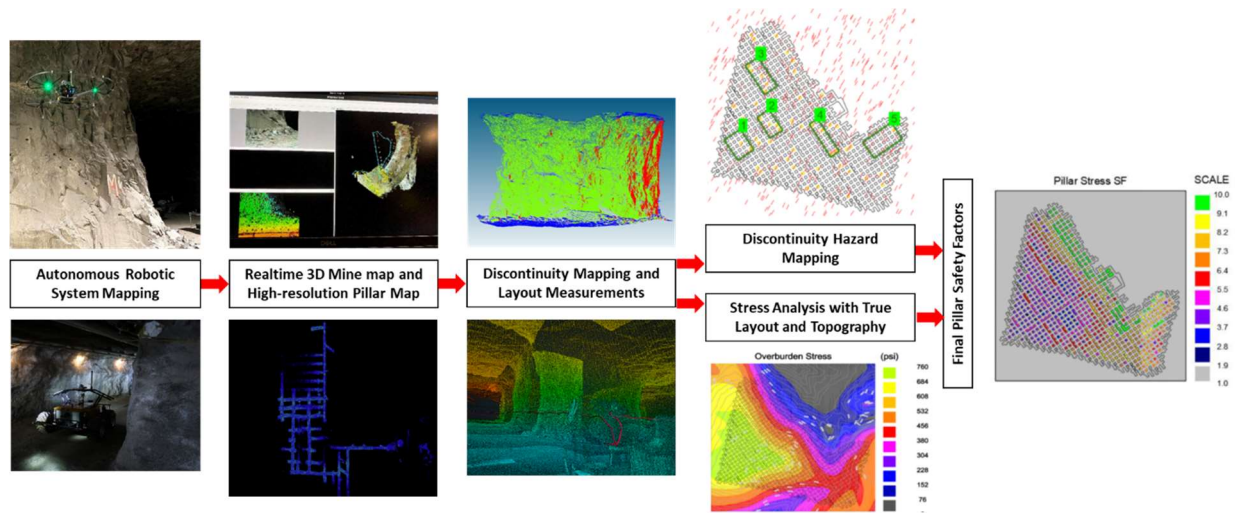


**Figure 3.12.** Visualization of the design approach framework.

### **Research Objective 2.1: Develop stone mine pillar module for stability mapping.**

The robotic system developed in the first specific aim can map the mine layout, autonomously by ground robot, and provide high-resolution pillar maps, autonomously by tethered drone. From these 3D point cloud maps, true pillar layout dimensions can be measured, and discontinuities can be mapped. The layout information can be used to update or generate the overall mine map, and the geological information can be overlaid on the mine map to generate the hazard map. The pillar layout and overburden topography maps are used as input to the LaModel program for stress analysis. In this research, the application of the S-Pillar empirical stone pillar strength equation is extended to the Boundary Element Method software (BEM), LaModel. Therefore, irregular stone mine pillar safety factors under variable topography can be calculated using the LaModel software. In addition, the software tool developed in this research can use the LaModel output, discontinuity hazard mapping grid, and large discontinuity factor approach of S-Pillar to explicitly account for the impact of large discontinuities on local pillar stability.

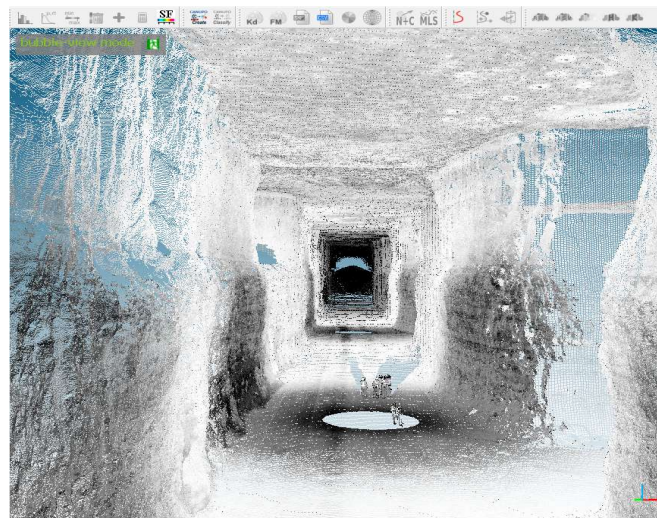
#### ***Task 2.1.1: Setting a benchmark for robotic measurement accuracy.***

Figure 3.1 shows the robotic system that is developed in this project. This system is designed to autonomously navigate in an underground stone mine and scan the pillars (Figure 3.12). During the scanning process, the ground robot stops, UAV takes off, moves towards to pillar wall, and stops at a certain distance from the wall. Then it starts scanning the pillar wall by flying parallel to the width of the pillar until it reaches the pillar corner. Next, UAV increases its altitude, and at this higher altitude, it repeats the parallel flight in the opposite direction. UAV repeats these series of parallel and vertical flights until it completely scans the whole pillar wall. The goal of this research task is to evaluate the accuracy and resolution of the robotic sensor measurements required to identify the discontinuities (joint sets, bedding planes etc.) and measure the pillar layout dimensions. The results of this research task will be used to guide the robotic system missions. For

this study, Oxpecker's sensor (Figure 3.4) data were compared with I-site 8200 terrestrial LiDAR scanner and ZEB horizon mobile LiDAR scanner. Open-source data-processing programs Cloud Compare, and Discontinuity SET Extractor (Riquelme et al., 2014) were used to process the data gathered from these systems.

Filed Studies: In order to compare different systems, point cloud data were collected from three different field studies where different systems were used. Filed studies were performed in two different mines. To assess the visibility of discontinuities from different 3D point cloud maps, pictures taken during the field tests, and in one instance the geological mapping performed by an experienced geologist, were used as references.

The first field study was carried out in a KY stone mine in a location where the pillars were partially benched, and the only illumination used for the data compilation was the lights coming from the cap lamps. During the field study, 10 pictures from different angles were taken, a visual assessment report was done by a geologist and fourteen scans with the Maptek I-site 8200 LIDAR were performed (Figure 3.13). The I-site 8200 scanner was mounted on a tripod with a height over 5 feet and 18 feet away from the rock mass analyzed, and each scan took approximately six minutes.



**Figure 3.13.** 3D point cloud map from the first field study.

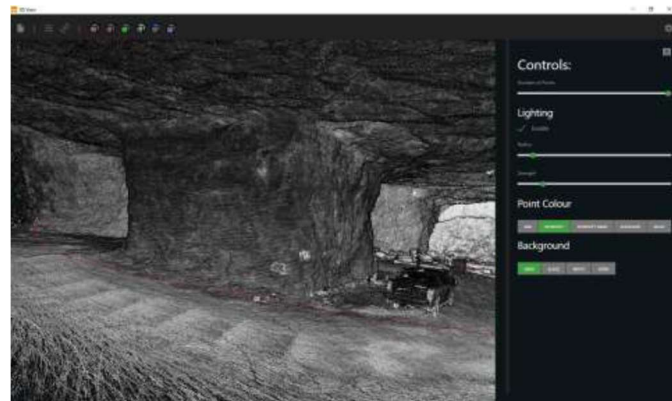


**Figure 3.14.** 3D point cloud map from the second field study.



The second field study was carried out in a PA Limestone Mine (Figure 3.14). The area scanned was a stone mine pillar located in the intersection of a main pass and a crosscut, this intersection was illuminated by the mine. The data gathered for this case study were around twenty pictures from different angles, and the device used was a ZEB horizon LIDAR scanner. The ZEB-HORIZON is a 2D time-of-flight range Velodyne Puck VLP-16 scanner which for the collection of cloud points the user carried the scanner wired to an external battery and data logger device during the scanning process.



*Figure 3.15. UAV mapping, the third field study.*

The third field study was at the same location as the second one. Autonomous scanning of the UAV was tested, the scanner used for this test was a RealSense L515 depth camera that was mounted on a drone and the mapping was performed from 2 meters away from the pillar (Figure 3.15).

***Task 2.1.2: Develop Stone Mine Pillar Stability module for Stability-Mapping.***

The objective of this research task is to develop an approach that integrates the large discontinuity factor (LDF) and the Boundary Element Method software (BEM), LaModel, to allow stone mine operators to assess the impact of the large discontinuities on local pillar stability. NIOSH published design guidelines for underground stone mines to guide the industry in designing pillar and roof support. These guidelines emphasize the impact of large, angular discontinuities on pillar strength. Esterhuizen et al. (2011) derived the large discontinuity factor (LDF) to account for the impact of discontinuities on pillar stability by adjusting the strength of the pillars. In this approach, the pillar load is calculated at the maximum depth over the pillar layout, and the tributary area loading calculation is valid if the mine layout consists of regular-sized pillars. In this research task, first, we extended the application of this approach to the BEM to allow stone mine operators to integrate overburden stress distribution under variable topography and pillar layouts with irregularly sized pillars into their designs (Escobar, 2021). Then, we developed the approach to incorporate the large discontinuity impacts, overburden stress distribution under variable topography, and

irregular pillar layouts by utilizing: LDF, AutoCAD ObjectARX add-in Integrated Stability Mapping Software (ISMS), and LaModel software. The ISMS step transformation function is used to identify the pillars intersected by the large discontinuities and to generate the LLDF grid of the intersected pillars. LaModel is used to compute the safety factor of the stone mine pillars by simulating the strength of complex pillar geometries with the empirical stone mine pillar equation (Esterhuizen et al., 2011; Escobar, 2021). The software tool uses the LLDF grid and LaModel output files to generate the final pillar stress safety factors, which can be visualized in AutoCAD.

*Implementing the Empirical Stone Mine Pillar Strength Equation into the Boundary Element Method Software LaModel*

In this research, the equation for the increasing stress into the interior of a stone mine pillar, as a function of the pillar width-to-height ratio, was derived from the empirical pillar strength equation proposed by Esterhuizen et al. (2011) (Equation 2.1). The gradient stress equations for the stone mine pillars were derived by following similar approaches to those presented by Mark et al. (1992) and Johnson et al. (2014). In these approaches, it is assumed that the variation of stresses within the pillar is a function of distance to the closest rib. The stress gradient function provides the stress distribution within the pillar and is used to derive concentric rings of zones to simulate stone mine pillar yielding in boundary element software.

Following a similar procedure to the one used by Johnson et al. (2014), the square pillar is first divided into eight symmetric pieces for simplicity in calculations (Figure 3.16). Then, cell strength equations were derived for Esterhuizen's base empirical stone mine pillar strength equation, Equation 2.1.

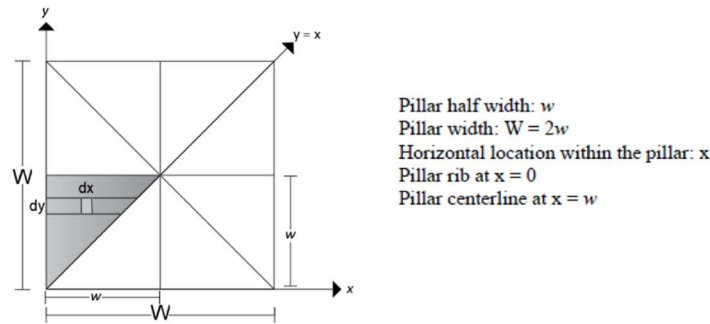


**Figure 3.16.** Plan view of the stress distribution of a square stone pillar (After Johnson et al., 2014).

Equation 3.1. is the empirical strength equation for stone pillars developed by Esterhuizen et al. (2011) where;  $\sigma_p$  is the average pillar strength, the symbol “k” in Equation 2.1 is replaced by “ $\sigma_0$ ” (the rock strength parameter), “w” is replaced by “W” (the width) to be consistent with Figure 3.16 and “h” is the height of the pillar.

$$\sigma_p = \sigma_0 \times \frac{W^{0.3}}{h^{0.59}} \quad (3.1)$$

The ultimate load-bearing capacity of the pillar (F) is calculated by multiplying the pillar strength ( $\sigma_p$ ) by the area of the pillar:

$$F = \sigma_p \times W^2 \quad (3.2)$$

Then performing the substitution of Equation 3.1 into Equation 3.2:

$$F = \sigma_0 \times \frac{W^{0.3}}{h^{0.59}} \times W^2 \quad (3.3)$$

$$F = \sigma_0 \times \frac{W^{2.3}}{h^{0.59}} \quad (3.4)$$

Following the statement by Mark and Iannachionne (1992), the maximum value of horizontal location within the pillar is  $x = \frac{W}{2}$  (Figure 3.16), ( $0 < x < w$ ). Then substituting into Equation 3.4:

$$F = \sigma_0 \times \frac{(2x)^{2.3}}{h^{0.59}} \quad (3.5)$$

$$F = 4.92 \times \sigma_0 \times \frac{x^{2.3}}{h^{0.59}} \quad (3.6)$$

Johnson et al. (2014) defined the total vertical force (F) in terms of the vertical pillar stress ( $\sigma_v$ ) for a square pillar as:

$$F(W) = 8 \int_0^W \int_0^y \sigma_v(x) dx dy = 8 \int_0^W I(y) dy \quad (3.7)$$

$$I(y) = \int_0^y \sigma_v(x) dx \quad (3.8)$$

Moreover, Johnson et al. (2014) used Leibnitz Rule twice in equation (3.7) to obtain the total vertical force in terms of the vertical pillar stress for a square pillar:

$$\frac{d^2F}{dW^2} = 8\sigma_v(W) \quad (3.9)$$

Consequently, using the methodology determined by Johnson et al. (2014) for the square stone pillar variables, Equation 3.10 and Equation 3.11 are obtained:

$$\frac{dF}{dw} = 8 \int_0^w \sigma_v(x) dx \quad (3.10)$$

$$\frac{d^2F}{dw^2} = \frac{d^2F}{dx^2} = 8\sigma_v(x) \quad (3.11)$$

Then the vertical pillar stress of a square stone pillar is obtained by substituting Equation 3.6 into Equations 3.11 and 3.12:

$$\frac{dF}{dx} = 4.92(2.3)\sigma_0 \frac{x^{1.3}}{h^{0.59}} = 11.33\sigma_0 \frac{x^{1.3}}{h^{0.59}} \quad (3.12)$$

$$\frac{d^2F}{dx^2} = 11.33(1.3)\sigma_0 \frac{x^{0.3}}{h^{0.59}} = 14.73\sigma_0 \frac{x^{0.3}}{h^{0.59}} \quad (3.13)$$

Finally, the second derivative of the load-bearing capacity is divided by the eight symmetric pieces of the pillar to obtain the cell strength equation for stone mine pillars:

$$\sigma_v(x) = 1.84\sigma_0 \frac{x^{0.3}}{h^{0.59}} \quad (3.14)$$

Where,  $\sigma_v(x)$  is strength at distance x from the rib of the stone pillar, " $\sigma_0$ " is the rock strength parameter expressed in terms of the UCS, "x" is the distance from the rib towards the center of the pillar, and "h" is the height of the pillar. Equation 3.14 can be expressed both in the International System of Units (S.I.) and Imperial System of Units (I.U.). For pillar dimensions in the I.U. system,

the rock strength parameter " $\sigma_0$ " is computed as  $0.92 \times \text{UCS}$ , for the S.I. " $\sigma_0$ " becomes  $0.65 \times \text{UCS}$  (Esterhuizen et al., 2011).

Johnson et al. (2014) stated that the second most common cell element used to model pillars in boundary element program is the corner cell element (Figure 3.17).

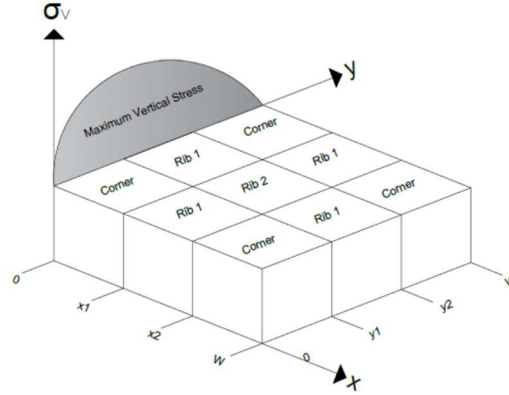


**Figure 3.17.** Stress Profile for different types of elements in a square stone pillar (After Johnson et al., 2014).

Mark et al. (1992) defined the ultimate load-bearing capacity equation for corner cell elements as:

$$F_{corner} = 2 \int_{x_1}^{x_2} \sigma_v(x) w(x) dx \quad (3.15)$$

Where  $w(x)$  is the width function for square stone pillars and " $W$ " is the cell width:

$$w(x) = (x_2 - x) \quad (3.16)$$

$$\text{for } x = x_1, w(x) = x_2 - x_1 = W$$

$$\text{for } x = x_2, w(x) = x_2 - x_2 = 0$$

Substitution of the cell strength Equation 3.14 and Equation 3.16 into the Equation 3.15 gives:

$$F_{corner} = 2 \int_{x_1}^{x_2} 1.84 \sigma_0 \frac{x^{0.3}}{h^{0.59}} (x_2 - x) dx \quad (3.17)$$

$$c_1 = \frac{1.84}{h^{0.59}} \quad (3.18)$$

Substitution of the Equation 3.18 into Equation 3.17 gives:

$$F_{corner} = 2c_1 \int_{x_1}^{x_2} x^{0.3} (x_2 - x) dx \quad (3.19)$$

Separating  $c_1$  from the integration:

$$\frac{F_{corner}}{2c_1} = \int_{x_1}^{x_2} x^{0.3} (x_2 - x) dx \quad (3.20)$$

Solution of Equation 3.20 (Escobar, 2021):

$$F_{corner} = \frac{2c_1}{2.99} (x_2^{2.3} - 2.3x_2x_1^{1.3} + 1.3x_1^{2.3}) \quad (3.21)$$



$$\sigma_{corner} = \frac{F_{corner}}{W^2} = \left( \frac{2c_1}{2.99W^2} \right) (x_2^{2.3} - 2.3x_2x_1^{1.3} + 1.3x_1^{2.3}) \quad (3.22)$$

Jhonson et al. (2014) stated that  $x_1$  and  $x_2$  need to be in terms of the width for the  $\sigma_{corner}$  to be a function of the width. The authors proposed a relation for the square pillar, where the locations of  $x_1$  and  $x_2$  are written in terms of the average location of the pillar  $\bar{x}$  (Figure 3.18).

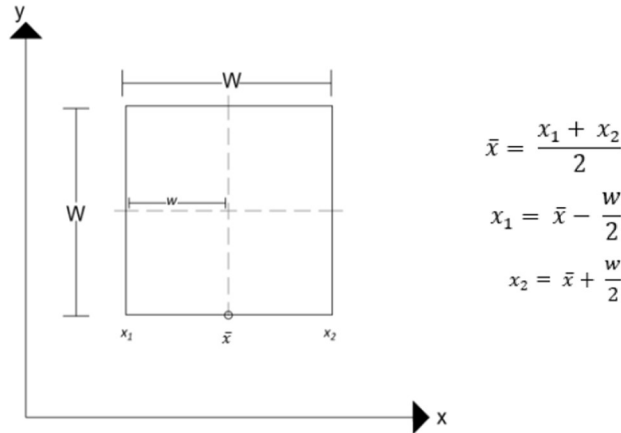


**Figure 3.18.** Average location within the square stone pillar (After Johnson et al., 2014).

Performing the substitution of  $x_1$  and  $x_2$  relations into Equation 3.22 and replacing  $c_1$  with Equation 3.18 (Escobar, 2021):

$$\sigma_{corner} = \left( \frac{1.23\sigma_0}{h^{0.59}W^2} \right) \left[ \left( \bar{x} + \frac{W}{2} \right)^{2.3} - 2.3 \left( \bar{x} + \frac{W}{2} \right) \left( \bar{x} - \frac{W}{2} \right)^{1.3} + 1.3 \left( \bar{x} - \frac{W}{2} \right)^{2.3} \right] \quad (3.23)$$

Where  $\sigma_{corner}$  is the average stress at the corner element of the pillar, " $\sigma_0$ " is rock strength parameter-dependent of the UCS, " $\bar{x}$ " is the average location within the pillar, "W" is the width of the pillar and "h" is the height of the pillar. Similarly, to the empirical strength equation for stone mine pillars (Esterhuizen et al., 2011), the Stone Pillar Corner Cell Equation can be calculated in the International System of Units by expressing " $\sigma_0$ " as 0.65 x UCS, and in the Imperial System of Units by expressing " $\sigma_0$ " as 0.92 x UCS.

#### Integrated Large Discontinuity Factor, Lamodel and Stability Mapping Approach for Stone Mine Pillar Stability

Equations 3.14 and 3.23 extends the application of the S-Pillar strength equation to the Boundary Element Method software LaModel. Equations derived by Escobar and Tulu (2020) assume that no large discontinuities are present and that discontinuities do not impact the strength calculation. The software tool that integrates the large discontinuity factor (LDF), Equations 3.14 and 3.23, and LaModel was developed to allow stone mine operators to assess the impact of the large discontinuities on local pillar stability.

Esterhuizen (2008) recognized the importance of the large angular discontinuities on the strength of the stone mine pillars and developed the LDF (Esterhuizen et al., 2011) to quantify their influence on pillar stability. The large discontinuity factor represents the average impact of large discontinuities on the strength of pillars in a layout of many pillars. Therefore, LDF implicitly

accounts for the spatial distribution of the large discontinuities at a stone mine. In this research, a new term, Local Large Discontinuity Factor (LLDF), is proposed to explicitly account for the impact of large discontinuities on local pillar stability. To better understand this concept, intersected pillars term is used to represent the pillars intersected with a discontinuity. Local large discontinuity factor of the pillar ( $LLDF_{pillar}$ ) specifically examines the safety factor of an individual pillar that intersects a discontinuity. Esterhuizen (2008) applies the LDF reduction to the whole mine layout. Instead of applying the effects of large discontinuities to the whole mine layout, LLDF allows quantifying the influence of large discontinuities on a selected local area within the mine. As shown in Figure 3.19, red lines represent the local discontinuities, yellow boxes show the intersected pillars, and black boxes are the pillars with no interaction with the discontinuity.

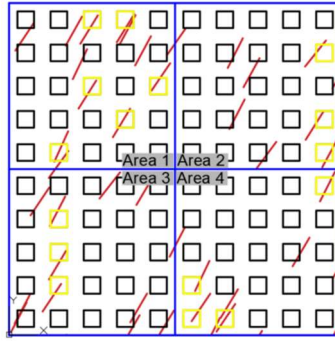


**Figure 3.19.** Pillar layout and theoretical discontinuity distribution.

LLDF strength reduction calculations are done in two steps. First, the safety factor of each pillar in a defined local area is calculated, and if large discontinuities intersect any pillars, strength reduction is computed using Equation 3.24, where “DDF” represents Discontinuity Dip Factor (Esterhuizen et al., 2011). Then the  $LLDF_{mean}$  of the specified area or the whole mine is found by the summation of safety factors of intersected pillars and undisturbed pillars divided by the total pillar number (Equation 3.25).

$$LLDF_{pillar} = 1 - DDF \quad (3.24)$$

$$LLDF_{mean} = \frac{(LLDF_{pillar} \times \text{intersected pillar number}) + (1 \times \text{undisturbed pillar number})}{\text{Total Pillar number}} \quad (3.25)$$

To prove the LLDF concept, one scenario is created as follows and compared with LDF calculations. The mine layout of 100 pillars with  $60^\circ$  discontinuity dip angle and 0.6 pillar width-to-height ratio is set (DDF=0.86). 16 out of 100 pillars are intersected pillars (Figure 3.19). The layout is divided into four different districts.

LLDF reduction for an intersected pillar is:

$$LLDF_{pillar} = 1 - 0.86 = 0.14 \quad (3.26)$$

There are 16 intersected pillars with LLDF reduction safety factors and 84 undisturbed pillars. The mean LLDF of the mine is calculated as:

$$LLDF_{mean} = \frac{(0.14 \times 16) + (1 \times 84)}{100} = 0.8624 \quad (3.27)$$

Esterhuizen et al. (2011) derived Equation 3.28 to calculate the frequency of large discontinuities per pillar, frequency factor (FF), using average discontinuity per pillar values determined from field surveys. The average frequency of large discontinuities per pillar is abbreviated as AFP in the formula which is dividing the pillar width by the average spacing of the discontinuity.

$$FF = 1 - e^{-AFP} \quad (3.28)$$

LDF is calculated using Equations 2.2 and 3.28 as:

$$LDF = 1 - 0.86 \times (1 - e^{-0.16}) = 0.8728 \quad (3.29)$$

The LLDF calculations of both individual and combinations of the areas are done as shown in Figure 3.20, where blue points show the LLDF values of the specified areas, and the orange line represents calculated LDF value.

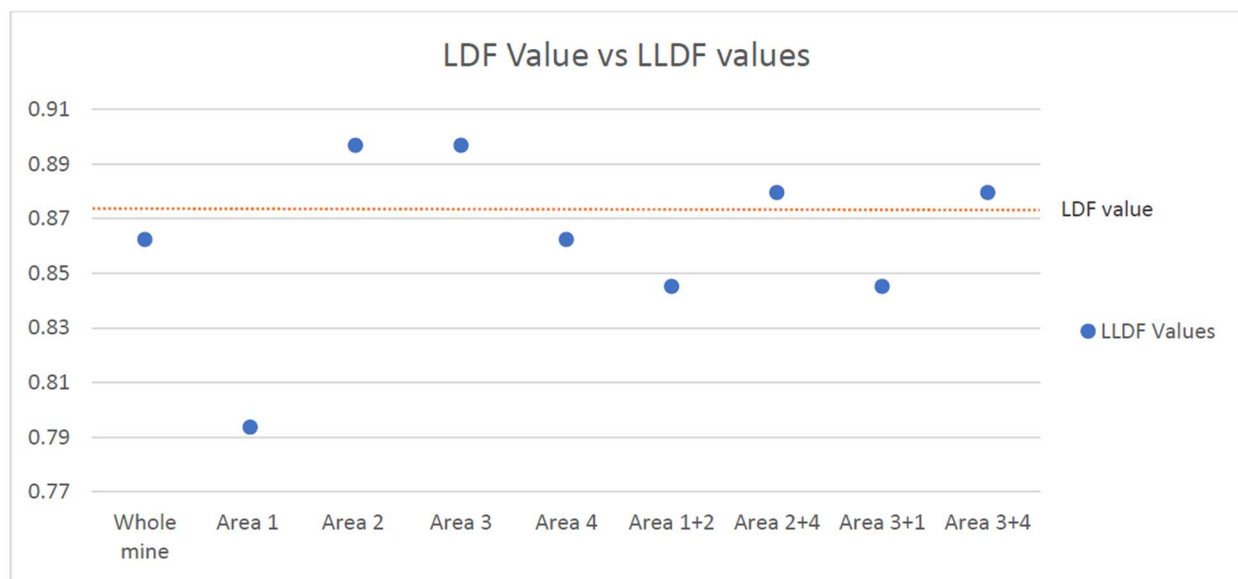


**Figure 3.20.** LDF and LLDF comparison.

The points below the orange line indicates that using LDF for the whole mine might cause overestimation of the safety factors in some local parts. In this scenario, especially for Area 1, it can be seen how the LDF overestimates the safety factor of local layout by almost 10%. Therefore, LLDF approach allows mine operators to assess the influence of spatial distribution large discontinuity sets on pillar stability explicitly and to identify hazardous locals on the mine map.

#### Implementing LLDF to pillar stability analysis

For implementing LLDF application into the mine layout, it is necessary to obtain the geological features from field surveying and mapping, the operational parameters from mine observations, overburden topography and pillar layout inputs from the mine surveys. The AutoCAD and LaModel software have been chosen for the illustration and calculation parts of the application. The LLDF application follows the procedure shown in Figure 3.21.

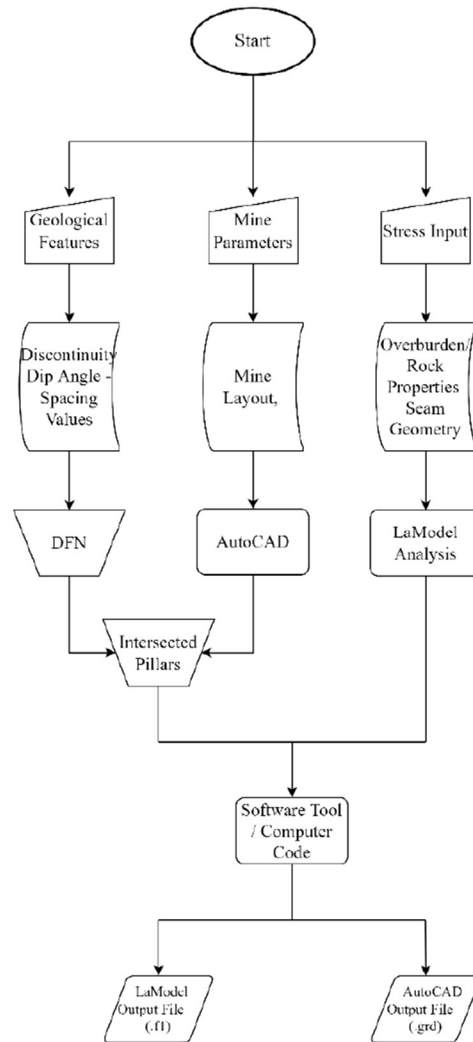


**Figure 3.21.** Data flow chart of LLDF application.

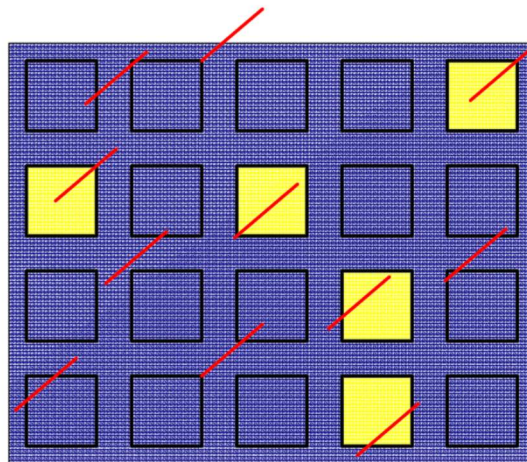


**Figure 3.22.** The application of `SMAP_SFCTORINAREA` command for intersected pillars.

Integrated stability mapping software is used to identify pillars that are intersected by a large discontinuity. Esterhuizen (2011) states that at least 30% of the pillars must be intersected by large discontinuities to be considered as an intersected pillar. The pillars intersecting the discontinuities are found (Figure 3.19) where red lines represent the local discontinuities, and yellow boxes show the intersected pillars. Then those pillars are assigned with a constant number via the SMAP\_SFCTORINAREA command. The module automatically assigns the number "100" as its default value. However, a specific number, such as the LLDF factor value, can be given if the user wants to indicate it in the grid file (Figure 3.22).

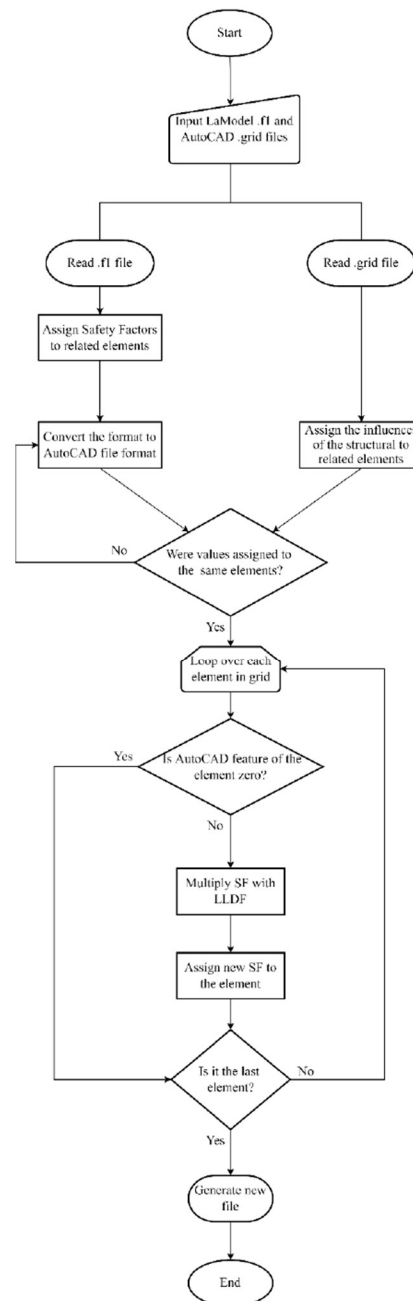


**Figure 3.23.** Details of the generating new safety factor file by using Python code.



A Python script for LLDF implementation is developed:

- Read LaModel output file (.fl).
- Convert .fl file into AutoCAD Integrated Stability Mapping Software grid format.
- Read AutoCAD Integrated Stability Mapping Software mine plan and intersected pillars (.grd).
- Define Local Large Discontinuity Factor .
- Match the safety factors in .fl file with intersected pillars in grd file.
- Multiply the safety factors of the intersected pillars by LLDF.
- Generate a new grid file with new safety factors.
- Convert new grid file into LaModel output format (.fl).
- Generate a new .fl file with new safety factors.

Figure 3.23 shows the flow chart of how python code implements a large discontinuity factor and inserts it into the output files.

### **Task 2.1.3:** Program Stone Material Wizard.

The “Stone Material Wizard” was programmed as a standalone script software using Python. Program requires five input parameters: pillar width, pillar height, UCS of the limestone, Elastic Modulus of the limestone pillar and yield zone number. Then calculates the elastic-perfectly plastic yield zone strength parameters and updates the LaModel input file (Figure 3.24).

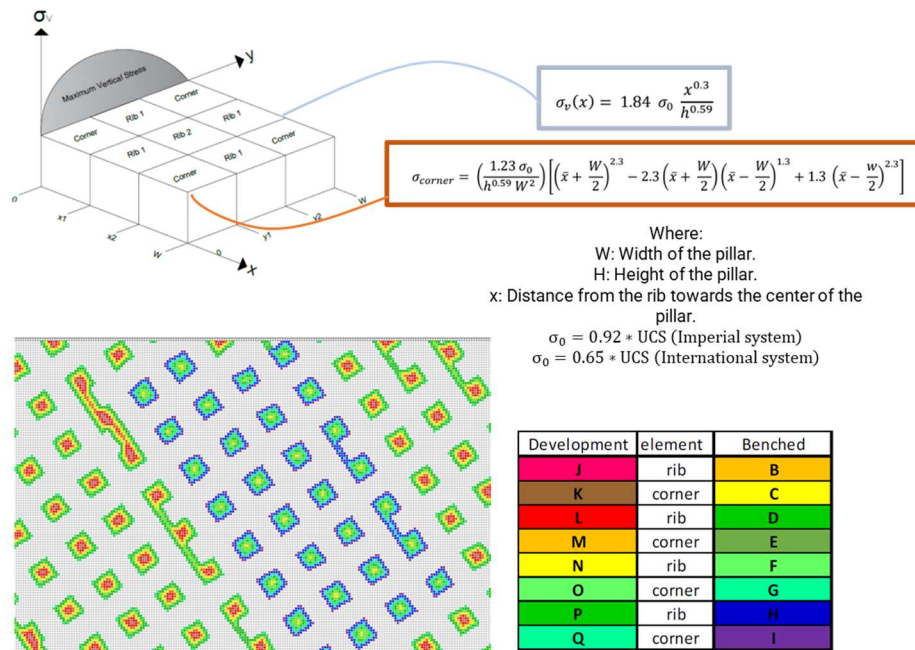


**Figure 3.24.** Stone Material Wizard approach.

**Research Objective 2.2: To develop an approach for time-dependent strength degradation adjustment for pillar strength equation used in S-Pillar.**

The fifth research objective involves development of a framework approach for time-dependent strength adjustment for pillar strength equation used in S-Pillar. Preston et al., (2015) used lapse photogrammetric survey to measure hard rock mine pillar volumes in different time intervals to measure pillar damage as depth of failure. Later, they used the DDA approach of the Roberts et al, (2007) to develop empirical pillar design guidelines from the back analysis of damage progression with stress analysis. Similar measurements can be performed with the LiDAR attached to an autonomous robotic system accurately and more efficiently. Since the naturally existing fractures on limestone pillars influence the long-term stability significantly, in this research, we developed a new modeling approach that can simulate the influence of naturally existing fractures on the strength and failure mechanisms of the underground stone mine pillars. This new modelling approach and LiDAR measurements can be used to back analyze the time-dependent strength degradation.

**Task 2.2.1: Develop a Modeling Approach for Incorporating Effect of Natural Fractures on the Mechanical Behavior of Limestone Pillars.**

In the fractured rock mass, discrete discontinuities might influence rock mass behavior slightly or significantly depending on the density of discontinuities within the representative rock mass volume. In order to investigate pillar mechanics, a systematical methodology is developed based on the novel approach, the Synthetic Rock Mass (SRM) by utilizing the two-dimensional Universal Distinct Element Code (UDEC). In order to form the first component of SRM, the Bonded Particle Model (BPM), the mechanical properties of the standard size laboratory rock specimen scaled up to the upper-limit of the Hoek-and-Brown Scaling Equation. Then, Voronoi-Trigon Discretization Logic is used to model the intact rock matrix of the stone mine pillars. Later, field data is used to stochastically generate Discrete Fracture Networks (DFNs), and SRM models are established by integrating the BPM and DFNs. Then, rock specimen sizes are increased from laboratory size to field size by sampling the generated DFNs. In the up-scaling operation (i.e. specimens' size increase), the homogenization process is applied that the estimated strength properties of the pillars by SRM are captured with a new BPM. By doing so, the numerical simulations calibrated against the empirical stone mine pillar strength equation established by NIOSH (Equation 2.3). Finally, the predicted strength parameters are used to examine the pillar failure mechanics with various width-to-height ratios.

**Standard Size Laboratory Specimen Calibration:** Hoek and Brown strength criteria is used to derive Mohr-Coulomb equivalent friction and cohesive strength parameters. Then, 0.05 m wide laboratory size rock specimen with the width-to-height ratio of 0.5 is calibrated with the parametric studies to simulate intact rock stress-strain behavior in the numerical code.

**Generation of Bonded Particle Model with Voronoi-Trigon Discretization:** BPM logic is implemented using UDEC to represent rock matrix as an assembly of Voronoi-Trigon Blocks where the explicit fracturing of the intact rock will be simulated along the trigon block boundaries. During the generation of BPM, size of the rock block is increased from standard laboratory scale

by following the scaling equation of Hoek and Brown (1980) (Equation 3.30). It should be noted that this equation is valid for sample sizes ranging from 10 mm to 200 mm.

$$\text{Rock Block Strength} = \sigma_{50} \left( \frac{50}{\text{width of the target rock block}} \right)^{0.18} \quad (3.30)$$

In the BPM, the strength reduction from Equation 3.30 is satisfied by calibrating the micro-properties (i.e. contact strength properties such as friction or cohesion) of the Voronoi-Trigon Tessellation. The simulated macro-properties (i.e. target strength properties), such as friction and cohesive strength, are captured with a series of test configurations constructed in UDEC: 1) uniaxial compressive strength test; 2) triaxial or confined uniaxial compressive strength test; 3) Brazilian indirect tensile strength test. Details of the trigon contact property calibration procedure are explained in Suner (2021) and Suner and Tulu (2022). Figure 3.25 illustrates the transition stage via Hoek and Brown scaling equation (1980) to generate BBMs.

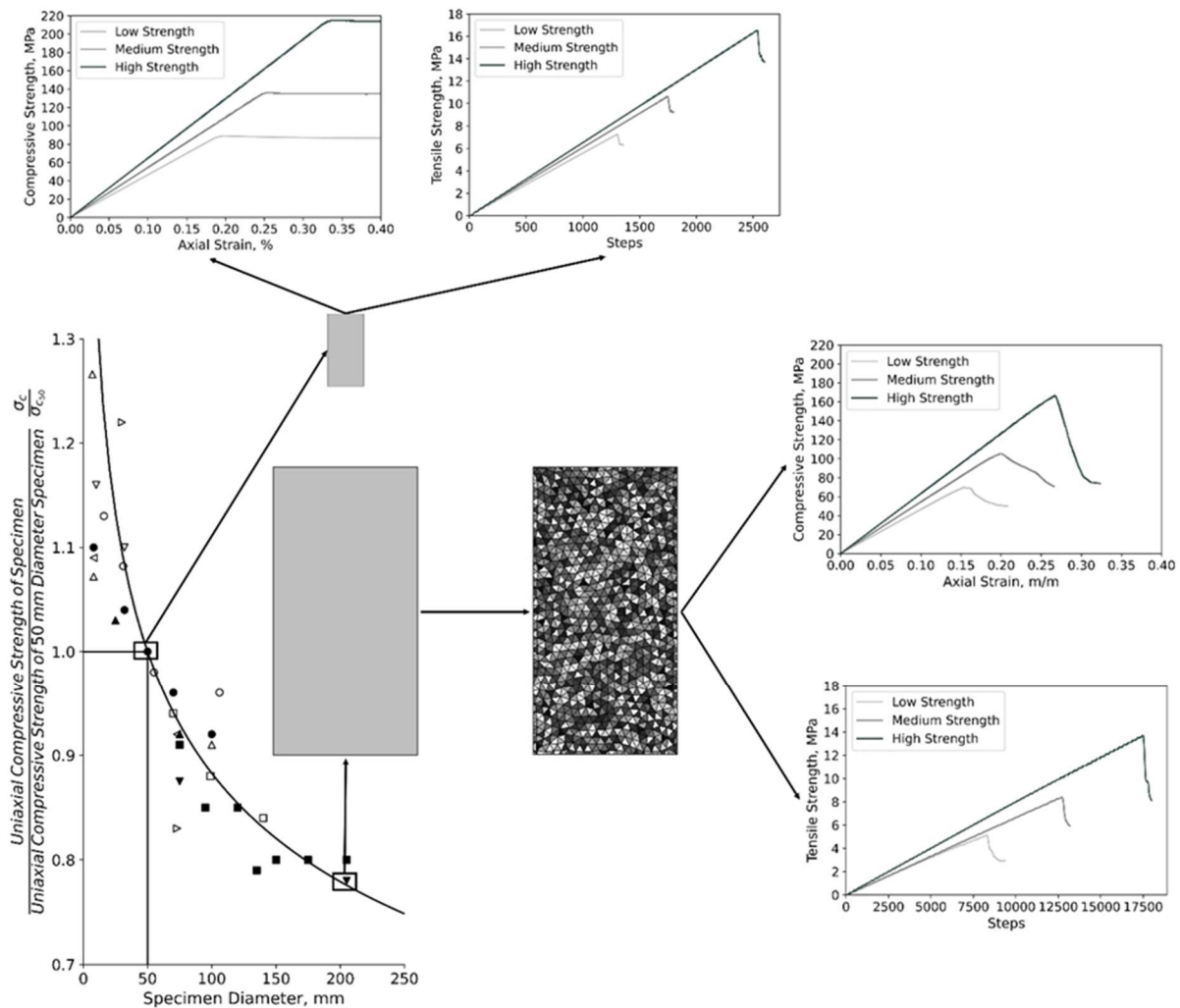


**Figure 3.25.** Transition Stage from Standard Size Laboratory Specimen to BBM via Hoek and Brown (1980) Scaling Equation.

Discrete Fracture Networks (DFNs) Approach: The transitional phase from laboratory scale to field scale is simulated by transition from BPM to SRM with the implementation of DFNs generated from the stone mine field survey database. DFN generation requires a stochastic approach, and knowledge in statistical analysis to prevent biases that would result in an inaccurate representation of the rock mass.

DFNs of a rock mass is represented by various parameters: fracture density size, size/trace length, orientation, and position. Fracture size density, the combination of fracture trace length, and density is an important parameter affecting the DFNs model generations. It controls the number of fractures per unit volume ( $n(l)$ ) that their size should be in the range of  $[l, l+dl]$ , where  $l$  and  $dl$  are the size and size increment of the fractures, respectively. The general knowledge indicates that fracture size density distribution is expressed as a negative-power law distribution functions in most of the field cases (Priest and Hudson, 1981; Elmo, 2006; Vazaios et al., 2017; Monsalve et al., 2019).

In the DFNs generation, the input parameters utilized in the numerical simulations are derived from the field observations (Esterhuizen et al., 2011). Mean GSI values of the S-Pillar database vary between 74 and 76 (Suner, 2021). The area of interest for this study on the GSI chart marked on Figure 3.26. Stone mine rock masses, within the range of the S-Pillar database, can be represented as blocky. The red line is the mean values for each rock strength category (i.e. low, medium, and strong) while the orange line represents the boundary for the one standard deviation from the mean value.

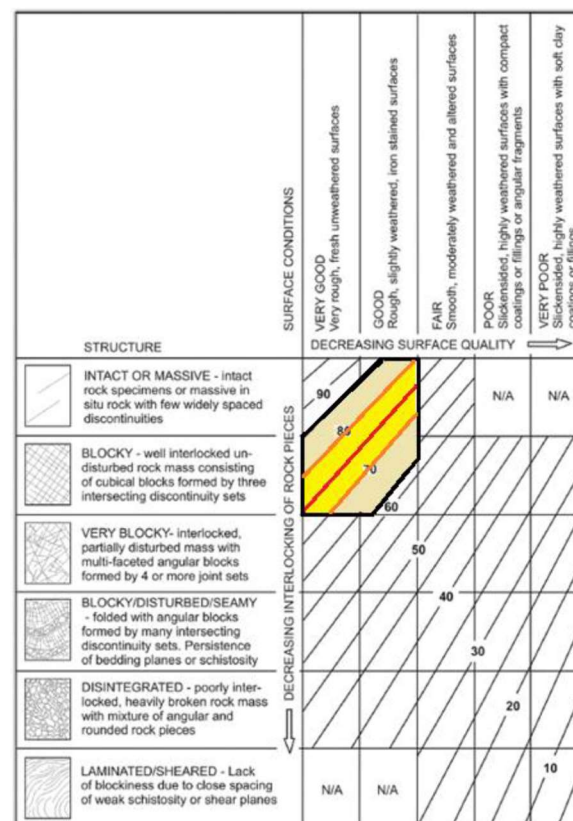


**Figure 3.26.** S-Pillar Database GSI Representation in GSI Table.

Three different DFNs realizations are generated for Low Strength, Medium Strength, and High Strength limestone formation reported by Esterhuizen et al. (2011). Details of DFNs realizations are explained in Suner (2021) and Suner and Tulu (2022).

*Synthetic Rock Mass Approach:* Unfortunately, using the same size discretization in laboratory specimen (i.e.  $200\text{ mm} \times 400\text{ mm}$ ) and field size limestone pillars (i.e.  $15\text{ m} \times 30\text{ m}$ ) found to be impractical due to excessive computer memory requirement. A rational procedure to scale simulated samples from laboratory to field size, a homogenization process, is introduced. This homogenization process can be thought as representative elementary volume (REV). The stress-strain response of the jointed pillar model is simulated with a new joint-free BPM with a larger particle size to study scale effects. The main advantage of utilizing this methodology is the reduced modeling time when simulating specimens from laboratory size to field size.

During the development of SRM, the DFNs are generated from the S-Pillar Database. From the stochastically generated DFNs model, the multi-stage upscaling methodology with the homogenization process at the interim stages is applied to establish rock block strength from laboratory to field. Figure 3.27 visualizes the up-scaling process. The SRM methodology to numerically assess the field size limestone mine pillars' strength and failure mechanism are summarize in Figure 3.28.

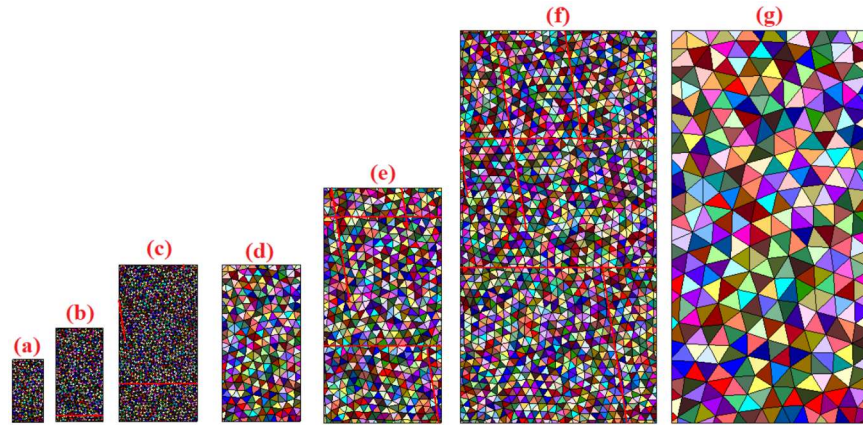


**Figure 3.27.** The representation of multi-stage up-scaling operation: a) BPM having  $0.2\text{ m}$  width; b) SRM having  $0.3\text{ m}$  width; c) SRM having  $0.5\text{ m}$  width; d) Homogenized BPM having width of  $0.5\text{ m}$ ; e) SRM having width of  $0.75\text{ m}$ ; f) SRM having width of  $1.25\text{ m}$ ; g) Homogenized BPM having width of  $1.25\text{ m}$ .



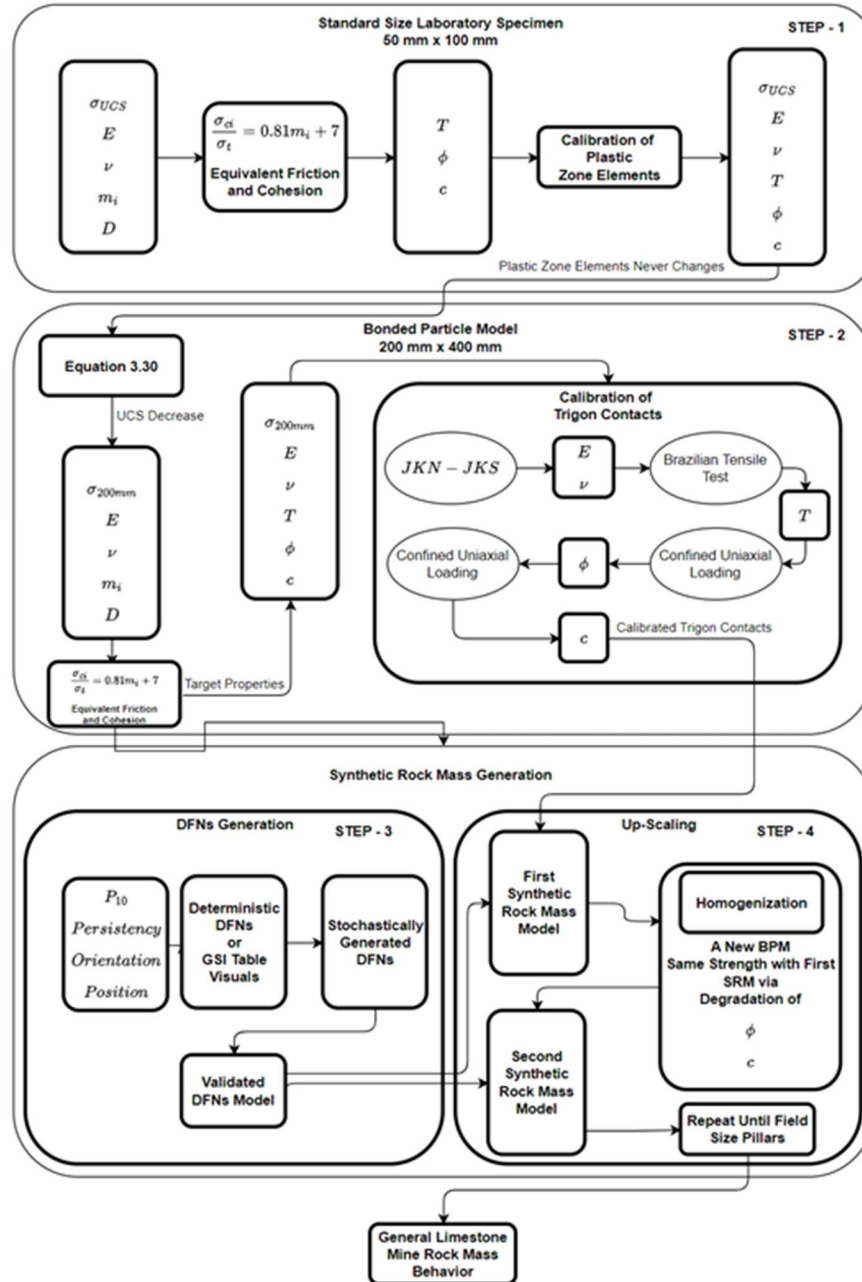


Figure 3.28. Flow Chart of SRM Methodology.

**Specific Aim 3:** Test and verify integrated autonomous robotics and Stability-Mapping based underground stone mine hazard detection approach.

**Research Objective 3.1:** To test reliability of integrated autonomous robotics system in underground environment and to verify integrated autonomous robotic system measurements.

The autonomous robotic system components deployed to different underground mine environments to test the reliability of the system components and to autonomously map pillars and entries. The integrated hazard mapping / BEM framework was applied to a field case study.

#### 4.0 Research Findings and Accomplishments:

Our research findings and accomplishments are summarized by classifying them into the following categories: (i) the autonomous robotic system and its components and (ii) the practical framework for integrating hazard mapping and pillar stability.

##### **The autonomous robotic system and its' components:**

###### *Integrate sensing, navigation, and mapping on a cooperative UAV/UGV systems.*

Experiments were performed to validate and fine-tune the robot's capabilities. Initial tests were conducted to assess the robot's driving performance through teleoperation over different types of terrain including concrete, grass, tiled indoor surfaces, gravel, and muddy terrain. Localization, waypoint navigation, and obstacle avoidance capabilities were tested on several terrains with the most extensive tests being carried out on an outdoor gravel terrain.

The robot was tested on a large gravel terrain to verify the performance of the robot localization by using user-generated waypoints as inputs for the planner module to allow the system to autonomously navigate to multiple waypoints for an extended period of time and validated via a truth reference solution from GPS measurements. The truth reference solution is determined by a carrier-phase differential GPS (DGPS) setup. The setup for the DGPS solution consists of two dual-frequency Novatel OEM-615 GPS receivers, and L1/L2 Pinwheel antennas, one mounted to the rover and the other mounted on a base station. The GPS data is post-processed using RTKLIB 2.4.2 and is solely used to validate the state estimates. The robot was deployed using the base station and monitored using the developed user interface during tests. In the first test, the robot autonomously navigated between two waypoints which were set 100m apart multiple times. The rover drove for 150 minutes and a total distance of 3.6km in a single run. Figure 4.1 shows the LIO-SAM euclidean distance error compared to the RTK GPS ground truth, where the error throughout the entire run is bounded within 0.5m and a 0.2 root mean squared error.

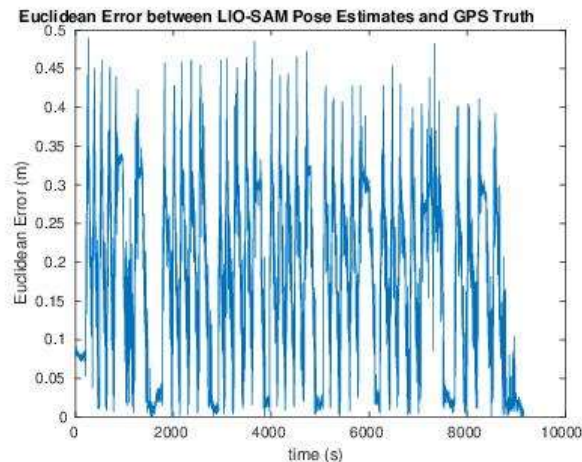


**Figure 4.1.** Euclidean distance error vs time for the robot driving between two waypoints for 3.60km.

For a more demanding test in comparison to the previous experiment, the system was given a set of waypoints to drive in a zigzag pattern. The set of zigzag waypoints allowed the researchers to verify the hardware (actuators and chassis) and the planner's ability to handle more challenging

missions. During the zigzag missions, Rhino autonomously operated for over an hour while traversing 2.3km. Figure 4.2 shows the trajectory of the rover where it traveled 475m and compares the similar state estimates and ground truth. The error during this mission is also bounded within 0.5m of the RTK GPS ground truth throughout the entire test.

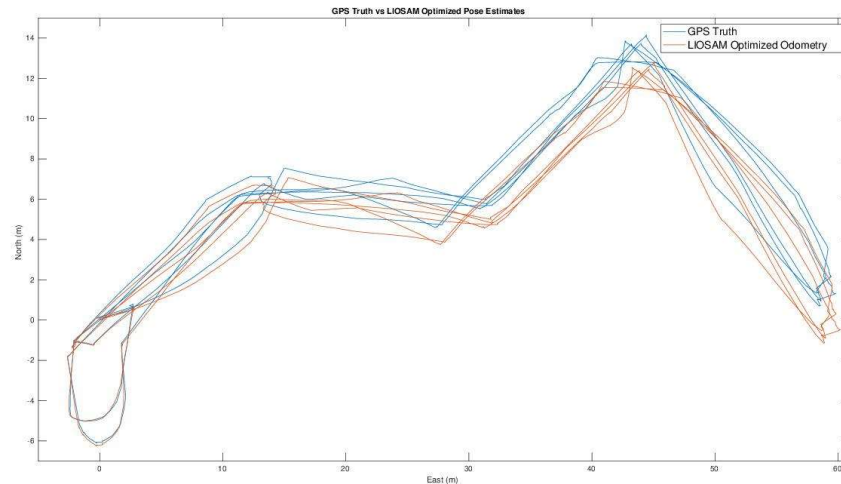


**Figure 4.2.** Robot zig-zag driving: blue represents the GPS ground truth and yellow the robot state estimation odometry.

Besides validating localization, these outdoor tests also demonstrate the capability of the robot to operate for extended periods of time, being able to drive more than 6 hours with a single battery cycle.

For the UAV/Oxpecker the planning, localization, and mapping autonomy software are reported in the following:

- Martinez Rocamora Jr, B., Lima, R. R., Samarakoon, K., Rathjen, J., Gross, J. N., & Pereira, G. A. (2023). Oxpecker: A Tethered UAV for Inspection of Stone-Mine Pillars. *Drones*, 7(2), 73.
- Samarakoon, K. Y., Pereira, G. A., & Gross, J. N. (2022, June). Impact of the Trajectory on the Performance of RGB-D SLAM Executed by a UAV in a Subterranean Environment. In *2022 International Conference on Unmanned Aircraft Systems (ICUAS)* (pp. 812-820). IEEE.
- Samarakoon, K. Y. (2022). UAV Path Planning and Multi-Modal Localization for Mapping in a Subterranean Environment. (WVU Master's Thesis)

Below the UAV mapping and planning state machine are reported from as reproduced from Martinez et al. (2023).

Our framework relies on velocity-based control and thus requires that the drone's velocity is reliably estimated. For that, the Intel RealSense T265 odometry solution was integrated directly into the flight controller localization solution, which estimates the drone position and velocity. We also developed our localization approach, which uses the tether to obtain relative localization with

respect to the landing platform. Tether based localization can be fused with the IMU measurements using a sensor fusion algorithm based on the Extended Kalman Filter (EKF).

The coverage software on Oxpecker is designed to survey and map the face of a pillar or wall by executing a predefined trajectory. The area to be covered is assumed to be rectangular, and the chosen trajectory is a sweeping pattern, as shown in Figure 4.3. The sweeping pattern is implemented to cover the entirety of the area, which is done by designing the coverage rows to be perpendicular to the shortest height of the coverage area. This ensures that the trajectory involves flying the least number of turns, which directly affects the duration, route length, and energy consumption (Li et al., 2011).

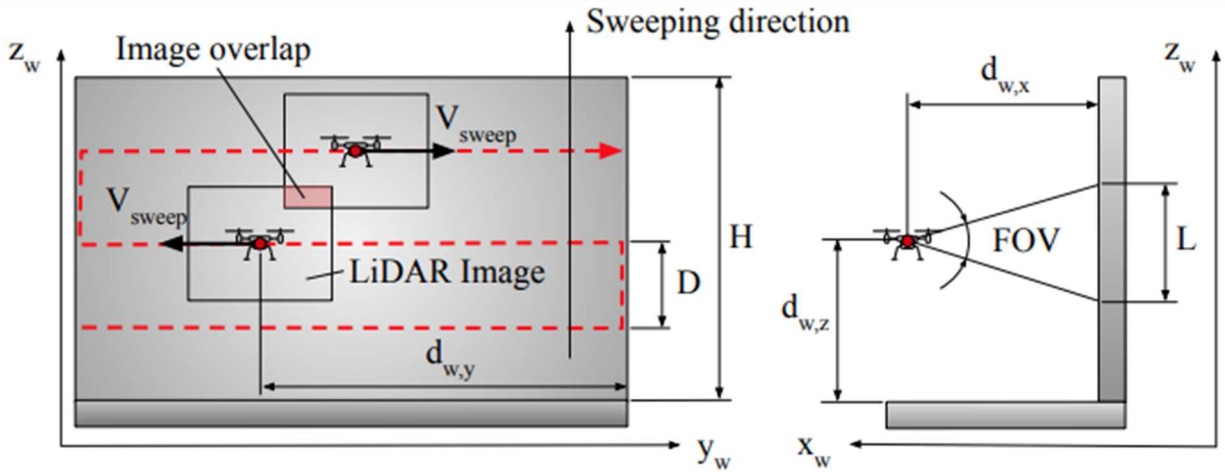


**Figure 4.3.** Sweep pattern implemented to cover an entire area with a distance of “d” between coverage rows.

To determine the number of rows required in the pattern, the approach outlined in Samarakoon et al. (2022) is followed. The first step is to determine the camera's footprint,  $L$ , which can be calculated using the geometric relationship between the distance from the camera plane to the wall,  $d_{w,x}$  and the camera's field of view (FOV):

$$L = 2d_{w,x} \times \tan \frac{FOV}{2} \quad (4.1)$$

The footprint is then used to determine the number of coverage rows and the gap needed to acquire a wanted overlap as represented in Figure 4.3. The number of coverage rows is computed as:

$$N = \frac{H}{L(1-s)} \quad (4.2)$$

where “H” is the height of the coverage area, and “s” is the desired overlap between two images as a fraction. The distance between the coverage rows can be calculated as:

$$D = \frac{H}{N} \quad (4.3)$$

For the complete design of the trajectory, lateral overlaps must also be considered. While longitudinal overlaps are determined by coverage rows, lateral overlaps are related to the speed of the UAV,  $V_{sweep}$ , and the frame rate of the camera as:

$$V_{sweep} = \frac{1-s_{lateral}}{L \times f} \quad (4.4)$$

where “ $s_{lateral}$ ” is the overlap expressed as a fraction, “ $L$ ” is the image footprint, and “ $f$ ” is the frame rate in frames/second.

After defining the survey parameters, the path of the UAV along the coverage rows can be defined by a set of 3D points. Since we have several rows, the “ $z$ ” coordinate is calculated for each row as:

$$d_{w,x}^{(i)} = i \times D - \frac{D}{2}, \quad i = 1, \dots, N \quad (4.5)$$

Initially we considered use of visual-inertial odometry (VIO) and predefined waypoints (a sequence of navigate the drone to follow the desired pattern). However, this method is not practical when mapping walls of different lengths (since coordinates  $y$  of the path would change for each wall) and was prone to position drift due to the featureless environment. Therefore, we changed to reactive method of coverage that relies on flying the drone in front of the wall until it finds its border. An edge-detection software was then developed to replace the necessity of predefined waypoints along the  $y$  axis. This software processes the raw depth image given by the drone's LiDAR (RealSense L515) and calculates the difference between the average depth of the outer left and outer right sides of the image. If the difference exceeds a set threshold, an edge is detected.

Although we chose to use a low-noise sensor, to cope with eventual noise on the depth image given by the sensor, several steps are taken by the system. First, the sensor is configured to work in a predefined range, thus outputting a constant value for distances outside this range. This can be observed in Figure 4.4 (b), which shows a flat black region representing points very far from the sensor. Second, after the depth image is received, the software applies to the image a binary mask that removes the ceiling and the floor from the data, keeping only the region of interest situated in between these two regions. Finally, a sequence of morphological operations (erosions and dilations) are applied to the masked data to remove additional noise.

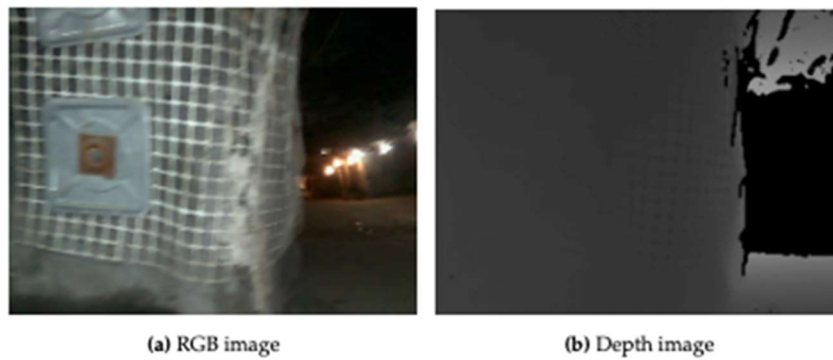


**Figure 4.4.** Raw snapshots from an instance when the edge is detected. (a) shows the color image of a pillar in a coal mine (the image is blurry due to the motion of the drone). (b) shows a depth image of the same instant. Notice that when the edge is detected, if the drone is leveled, a void appears in the center-right part of the depth image, indicating that the distance in that region is outside of the predefined processing distance. The top-right and bottom-right are ignored since they can show the ground or ceiling depending on the pillar's height and the drone's relative position.



The x coordinate of the path represents the drone's distance to the wall. In our approach, we keep a fixed distance from the wall using software that also relies on LiDAR data. Besides a constant distance, the controller adjusts the drone's orientation so that the camera is parallel to the surface being scanned. As illustrated in Figure 4.5, being parallel and at a fixed distance from the wall is important, especially when the wall is not planar. Furthermore, different distances and orientations can cause consecutive images to not have the appropriate overlap.

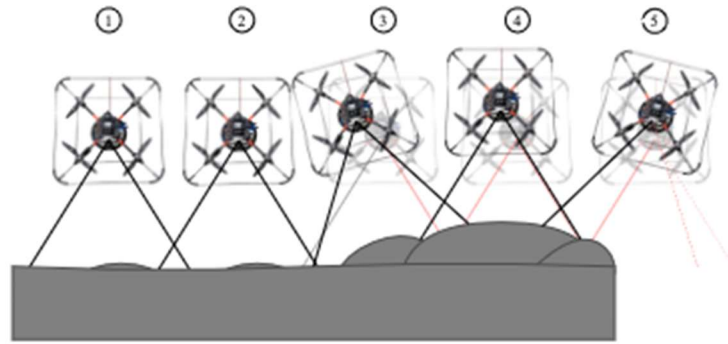


**Figure 4.5.** Top view of a UAV scanning the wall (in gray) at five different timestamps. At timestamps 1 and 2, the wall is basically flat, and the drone can move safely at a determined distance from the wall. At timestamps 3 and 4, the drone faces a bump in the wall. If the drone keeps moving laterally without adjusting the distance (transparencies), we may have an inconsistent overlap between the images captured at the current and next timestamp. The depictions without transparency illustrate how our controller handles the problem following its contour by adjusting the orientation and distance from the wall. At timestamp 5, the drone is not able to detect a valid distance on the leftmost beam (dashed lines), which indicates an edge of the pillar (Figure 4.3) and a need to switch the direction of movement.

To execute the complete path shown in Figure 4.3, a state machine within the “Mission Map” ROS node was developed. This node uses the information obtained from the wall-following software (another ROS node) and altimeter to execute the algorithm shown in Figure 4.6. While the wall-following node maintains a fixed distance from the wall and detects the edges, the altimeter attempts to maintain a specific row height until the next row must be executed.

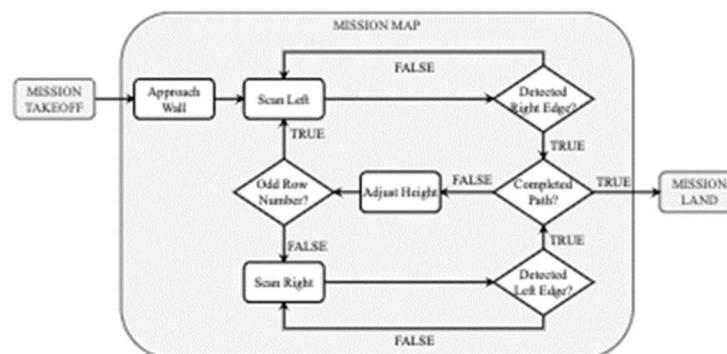


**Figure 4.6.** Sweeping trajectory execution algorithm within the “Mission Map” block.

The path planning strategy described was implemented in ROS and tested in a simulated scenario and on a DJI Matrice 100 drone. The latter served as a software integration and testing proxy while

the experimental drone hardware was being integrated. Due to the inability to provide a source of odometry ground truth for the physical experiments, our path-planning and mapping approaches were initially tested in a graphical simulator for validation purposes. In one set of simulations, we, for example, investigated the impact of combining ranging information with INS and visual odometry (Samarakoon et al., 2022). Results from these investigations are summarized in Table 4.1, where it is evident fusing more information to visual odometry yields improvements in performance.

*Table 4.1. Error associated with different sources of odometry by implementing the path planning strategy (simulator results).*

	Max Error (m)			Mean Error (m)			RMSE (m)		
	$X$	$Y$	$Z$	$X$	$Y$	$Z$	$X$	$Y$	$Z$
<b>Visual Odom</b>	0.558	0.779	0.188	0.177	0.405	0.095	0.074	0.180	0.072
<b>Sensor Fusion Odom</b>	0.178	0.162	0.071	0.035	0.067	0.050	0.032	0.067	0.050

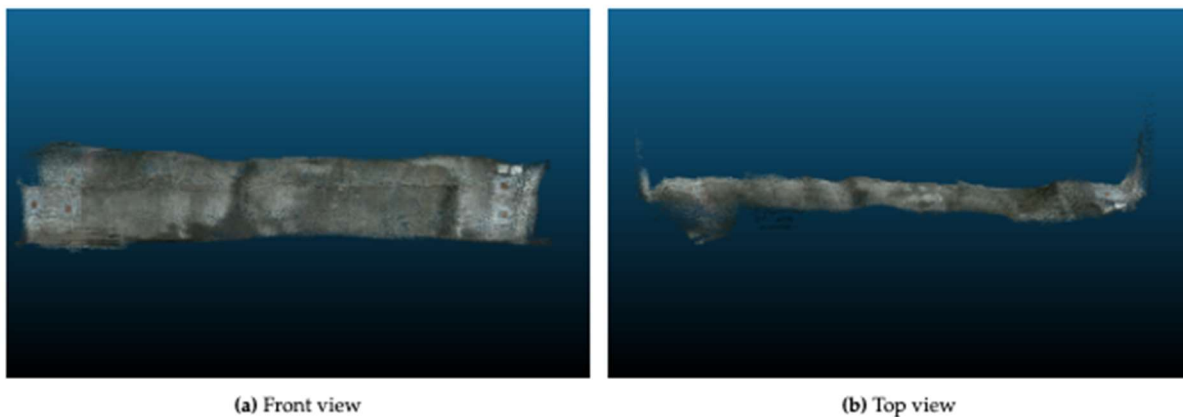


*Figure 4.7. Typical map of a pillar. The drone collects the data by moving in a lawnmower pattern in front of the pillar. When the edges of the wall are detected, the drone changes the height and horizontal direction of movement.*

Real world UAV mapping experiments were executed in the Safety Research Coal Mine operated by the National Institute for Occupational Safety and Health (NIOSH), located in Pittsburgh, PA. A wall within the coal mine was surveyed autonomously. During the flight, the drone's computer saved data that was relevant for mapping. This included RGB images, depth images, and odometry data, which altogether generated approximately ~18 mega-byte/second. In an effort to reduce the onboard computing cost, the 3D map was created during post-processing using an RGB-D SLAM approach called Real-Time Appearance-Based Mapping (RTAB-Map). During post-processing, the primary front-end odometry source was the T265, whilst RTAB-Map used the RGB and depth images to detect loop closures in the back end. This information was combined with specific parameters for RTAB-Map, which included extracting up to 500 visual features per image and

detecting a minimum of 20 visual features. This constraint ensures the acceptance of only certain loop closures. A resulting map can be seen in Figure 4.7.

By observing the resultant map, the designed trajectory successfully explored and mapped the entire wall. Figure 4.7(a) shows that there were no noticeable gaps in the point cloud, indicating sufficient overlap. Figure 4.7(b) shows that the left and right edges were found. A video with some other experiments at the NIOSH experimental mine is available at “<https://www.tinyurl.com/oxpeckeruav>.” Additional experiments and simulations that evaluate our coverage methodology can be found in Samarakoon et al. (2022).

*Develop a tethering system between the UGV and UAV for power transmission and autonomous landing.*

A series of experiments were performed to demonstrate the capabilities of hardware and software for tether management and tether-based landing described before. In these experiments, the TUAV started from different relative positions with respect to the platform. The experiments were conducted in a high bay facility. Figure 4.8 shows images from the experimental setup. On the left we see Oxpecker hovering above the UGV, with the tether fully extended and taut. On the right, a sequence of overlaid snapshots shows the drone approaching and landing on the platform on top of Rhino.



**Figure 4.8.** Typical tether-guided landing. The tether is made taut to help guide the drone back to the landing platform carried by the UGV.

In Figure 4.9, we show an overview of one of the experiments conducted to demonstrate the landing methodology. In Figure 4.9(a), the drone executes three missions. In “Mission Takeoff” (yellow trajectory), the drone takes off to a height of 0.8 m from the platform. In “Mission Move” (cyan trajectory), the drone moves forward with a setpoint speed of  $0.15 \text{ ms}^{-1}$  for 10 s and laterally and up for another 10 s. In “Mission Land” (magenta trajectory), the drone receives zero speed setpoints for 2 s before starting the landing procedure. In Figure 4.9(b), we show the drone localization as given by the T265 sensor, the drone height obtained with the altimeter, and the tether length measured by our system. The background colors represent the different missions described before. Notice that when the altimeter is used for localization, it introduces discontinuities in the data. In this example, the discontinuities appear when the drone leaves the platform, and the altimeter starts measuring the distance to the ground and before landing when

the reverse sequence happens. In Figure 4.9(c), we show the tether tension during the entire experiment. During the first two missions (yellow and cyan backgrounds), the setpoint for the tether tension is 0.3 N. During takeoff, although the controller is trying to release the cable faster to decrease the tension, the drone moves up too fast, and a large peak in the tension occurs. Once the drone starts hovering (around  $t = 30$  s), the controller can adjust to the tension setpoint. Conversely, during landing (magenta background), the drone moves faster than the controller can retract the cable, causing the tension to drop below the tension setpoint, which has been increased to help the landing. The landing methodology was tested successfully from 10 different starting positions. The results in Figure 4.9(d) show the trajectories of the individual flights using the localization solution from the T265 tracking camera.

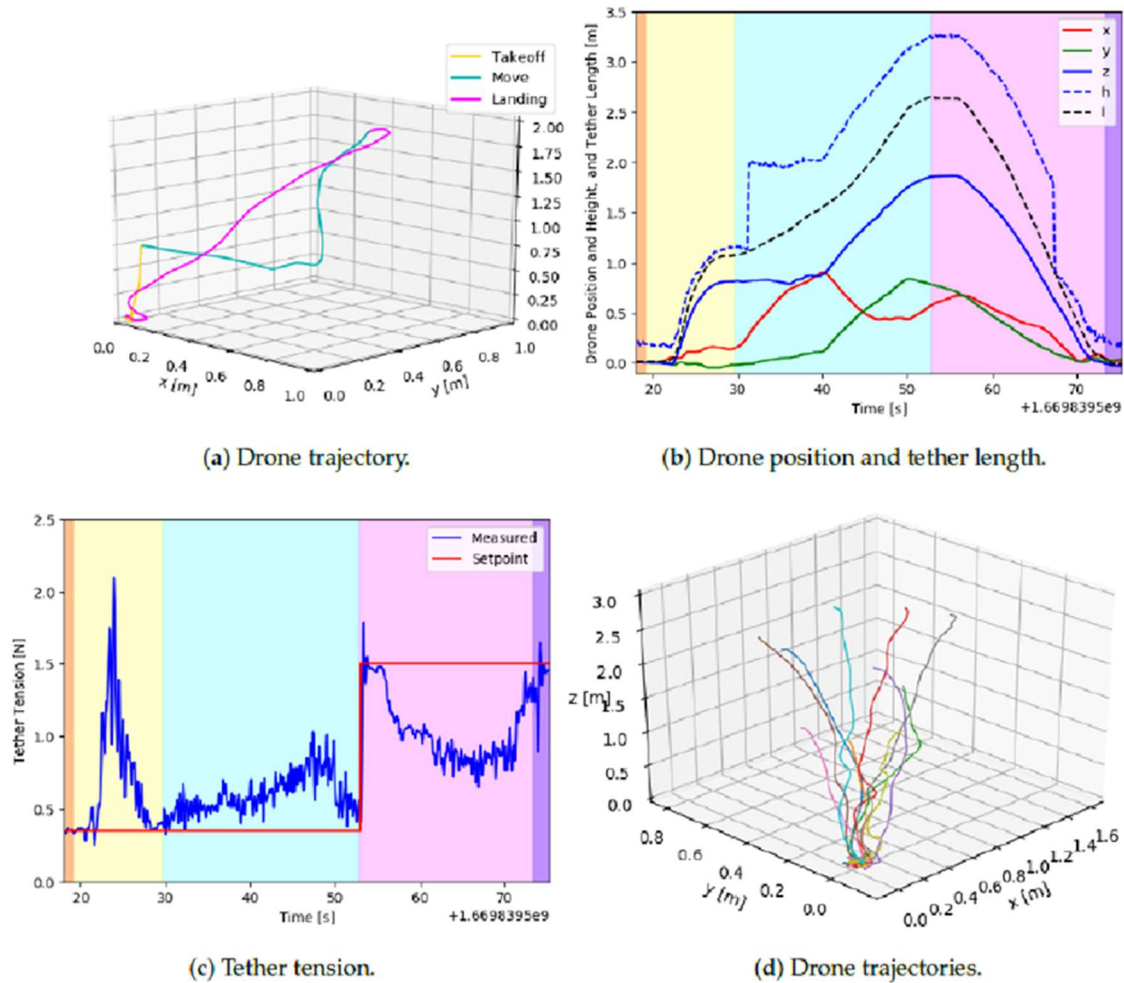


*Figure 4.9. Landing experiment: (a) TUAV trajectory in a typical experiment; (b) drone localization given by the T265 sensor, tether length measured by our system, and height given by a laser altimeter during the landing shown in (a); (c) tether tension during the landing shown in (a); (d) trajectories of several landings as seen by the T265 sensor.*



*Integrate high-level autonomy and planning on the robotic system.*

The robot's ability to operate in subterranean environments was validated on multiple visits to the National Institute for Occupational Safety and Health (NIOSH) Safety Research Coal Mine, Pittsburgh, Pennsylvania. Figure 4.10 shows Rhino operating inside the mine can be seen here.



***Figure 4.10.*** Rhino Robot inside the experimental Mine while mapping.

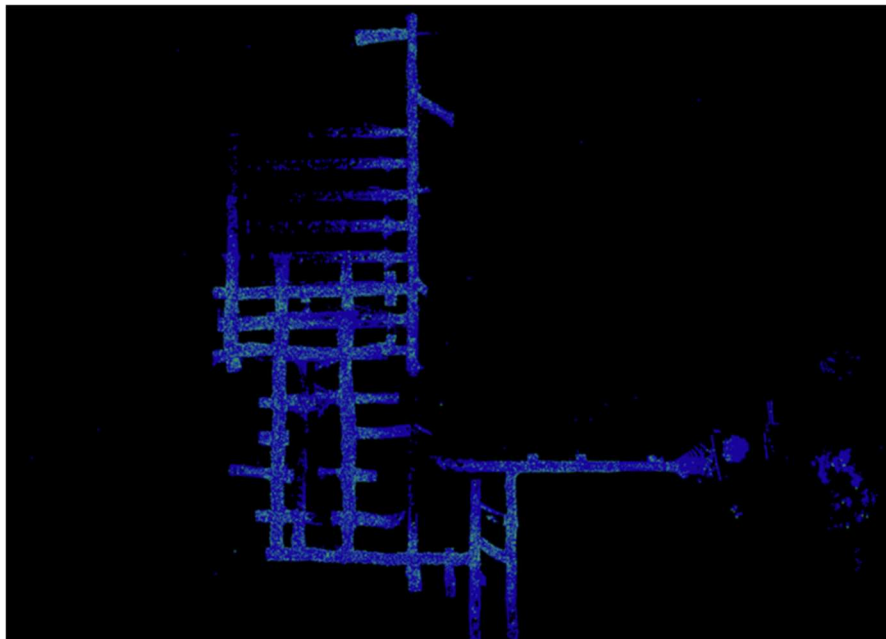


***Figure 4.11.*** Underground Mine LiDAR Mapping by UGV.



In order to verify the system's ability to operate in the mine, driving and mapping tests were performed by remotely teleoperating the robot via the base station and operators following the robot. Rhino was able to traverse the underground terrain while maintaining its state estimation. Figure 4.11 shows the map built by the rover during a run where Rhino traversed 1.018km inside the mine. During this mission, the robot drove over different types of terrain such as gravel, dry, and muddy terrain and built a mine map using the localization and mapping module LIO-SAM. During the mapping missions, the loop closure detection was qualitatively evaluated by driving in several loops to assess the system's ability to recognize loop closures. The areas of the mine that were not traversed had large amounts of water that the operators deemed unsafe for the system, although the Rhino was able to navigate through some sections with water.

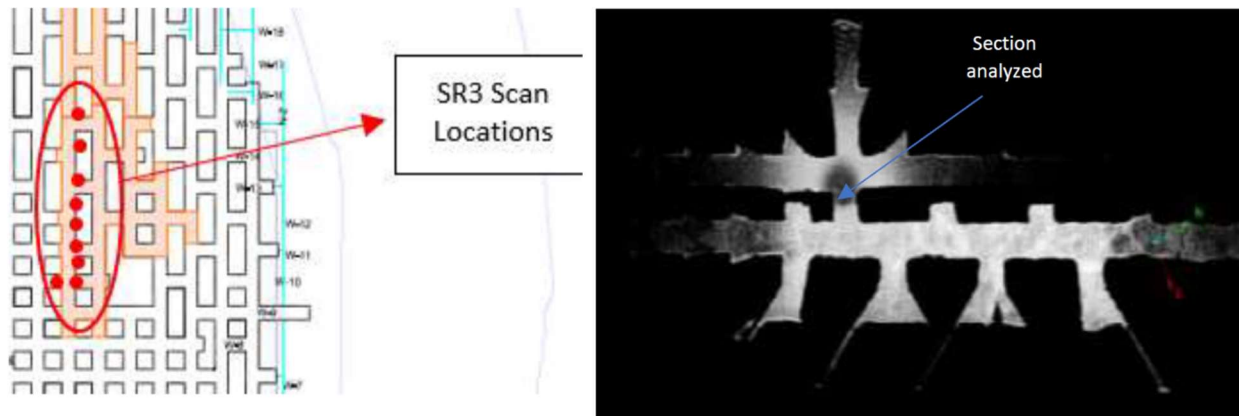
A lesson learned during these tests is that a better understanding of the environment would enable the robot to drive more efficiently and have a safer autonomous driving mode. Examples of these situations are narrow passages where two-way driving is preferable compared to trying to maneuver following arcs to return to a position behind the robot. Knowing the terrain type, where turn-in-place maneuvers can be performed over surfaces with lower friction such as gravel and muddy terrain, but is more challenging over terrain with higher friction such as paved surfaces.

### **The practical framework for integrating hazard mapping and pillar stability**

#### ***Mapping with SLAM based active remote sensing***

As shown in Figure 3.12 (in Section 3.0 of this report), the approach developed in this research uses the robotic sensor data to map the geological structures and develop 3D survey map of the mine. Geological structure and survey maps then can be used as an input to suite of software tools (LaModel, Integrated Stability Mapping and a new Python script) to assess the local stability of the stone mine pillars. Three field tests were performed in this research to assess the accuracy and potential of remote sensing methods to map the geological structures. In the first field test, terrestrial LIDAR scanner, I-site 8200, was used to scan the stone mine face, and conventional geological mapping of the face was performed by an experienced geologist. Point cloud data collected in this test were processed with Cloud Compare, and discontinuities are mapped from the 3D map and compared with the conventional mapping performed during the field test by the geologist. In the second field test, SLAM based LIDAR system, GeoSLAM, was used to scan the stone mine pillar. Data from this test is also processed with Cloud Compare and discontinuities are mapped and compared with the discontinuities identified on the photographs taken during the field experiment. In the third field test, pillar wall was scanned by the UAV autonomously. During this test, the autonomous flight trajectory of the UAV and the LiDAR scanning were observed to identify the operational parameters necessary to reach desired high resolution 3D maps.

***Field Study # 1:*** The investigation took place in main pass N-9 of an underground limestone mine where the pillars were partially benched. The zone analyzed was an area subjacent to two partially benched pillars and beneath a crosscut of an upper level. Fourteen scans were taken with the LiDAR scanner along the main pass N-9. Figure 4.12, left, shows the plan view of the mapped section from point clouds generated from those scans, and Figure 4.12, right, shows the plan view of the mine plan and location of each scan along the section.



**4.12. First field study, location of the area scanned.**

Conventional geological mapping of the rock face was performed by a geologist during the field test. Figure 4.13 shows the results of mapping: the total height of the partially benched pillar, the height and condition of the upper level crosscut, the type of material and discontinuities found, and the distribution of the roof supports. According to the report, the height of the partially benched pillar is 66 feet, the height of the crosscut is 30 feet, the roof is a shaley limestone bedding plane, the floor of the upper level is fracture with an apparent heave or lamination, and the distribution of the bolts are 5 feet and 6 feet at the crosscut and main pass respectively. The four bedding planes identified in this section possess the following material characteristics and thickness dimension:

- Light gray and blocky with 2 feet,
- Medium gray and massive 1.5 feet,
- Light gray and blocky with 2 feet,
- Medium gray and massive with 1.5 feet.

Due to the lack of illumination of the place, no discontinuity joints were perceived by sight.

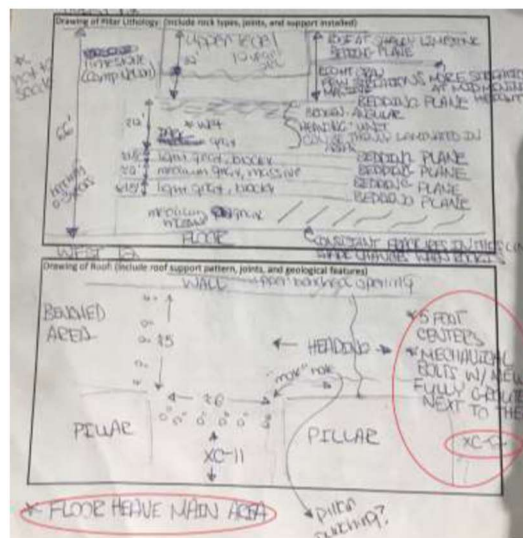


**Figure 4.13. Geologist mapping.**

Digital photographs were also taken to help visualization of the section studied, the material looks very blocky, and 3 bedding planes were identified easily however faults or joints were not easily identified due to the lack of illumination (Figure 4.14).



**Figure 4.14.** *Picture of the area analyzed, and bedding planes visualized.*

The point cloud of the rock mass assessed by the geologist was evaluated in the software program Cloud Compare to assess if the features and dimensions identified in the field can be seen in the point cloud. The height of the section is 65.5 feet, and the roof supports are visible and were measured resulting in a spacings between bolts along the crosscut and entry are approximately 6 feet by 5 feet (Figure 4.15).

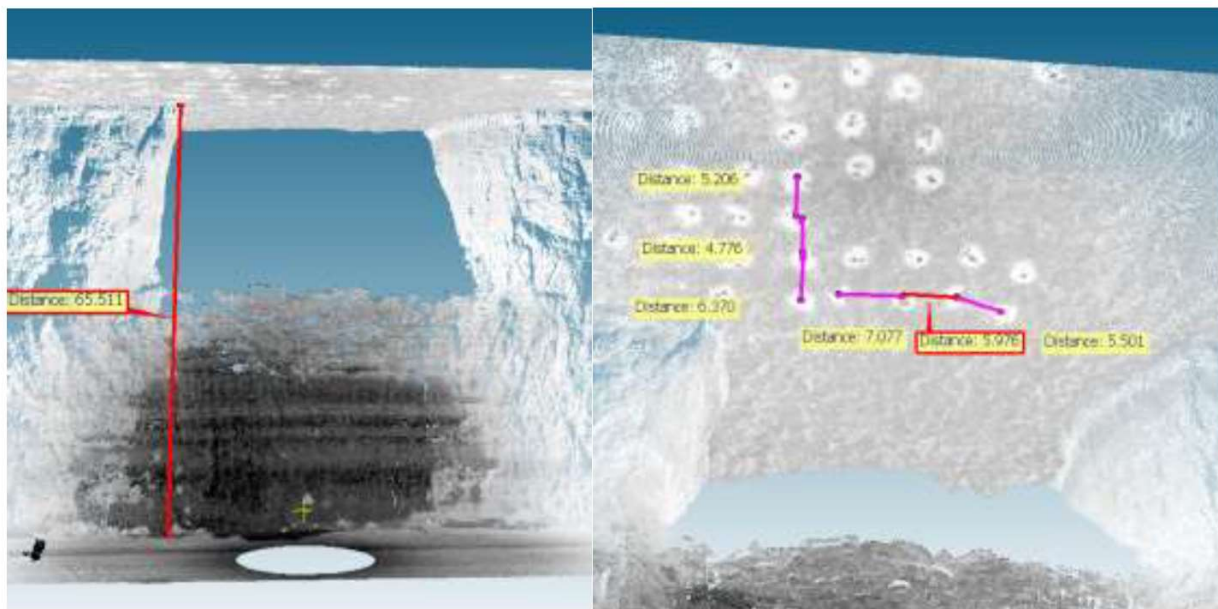


**Figure 4.15.** *Pillar height (left) roof support pattern (right).*

Discontinuity mapping with Cloud Compare gave good results when comparing the geological visual assessment report, it was possible to identify the four bedding planes, the height of the not fully benched pillar, the height of the crosscut and the distances between bolts very accurately. It is important to mention that this point cloud has point intensity values enabled which allows to see a difference of grays and identify the different rock bands. Four bedding planes were identified during the visual characterization (2.0 feet and light gray, 1.7 feet and dark gray, 1.5 feet and light gray, 1.8 feet and dark gray). The uniformity and better density of the point cloud (Figure 4.16) depends on the position of the LiDAR scanner, terrain conditions (orientation) and height of the rock mass.

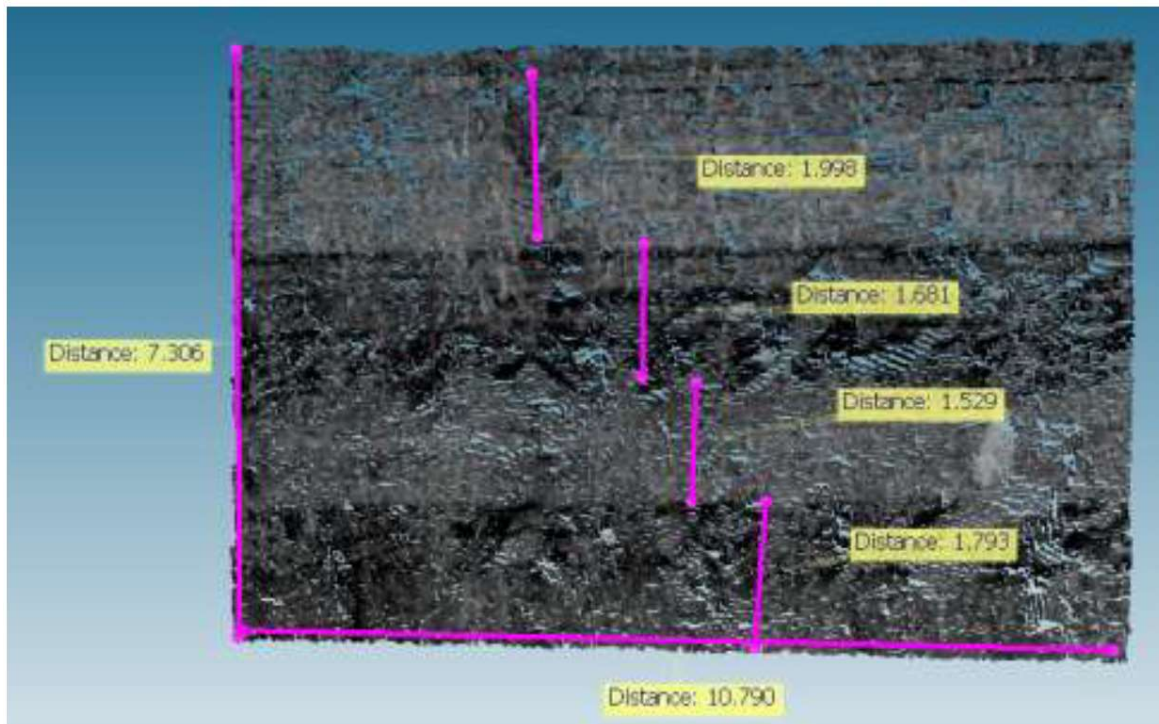


**Figure 4.16.** *Bedding planes from point cloud data.*

Field Study #2: The site of this second case study is in an underground mine located in southwestern Pennsylvania, where the predominant geologic composition is Loyalhanna Limestone, major source of crushed stone. The subject of study was a development pillar with dimensions of 27 feet in height and 45 feet by 45 feet in length and width respectively, located in the intersection of main pass number 10 (M-10) and crosscut number 3 (C-3). Due to the operational activities of the underground stone mine, the location of the pillar analyzed was illuminated, allowing to make a preliminary identification of the visible discontinuities present on the surface of the rock mass. Likewise, the location of the pillar was not a transited area which made it easy for the mapping with the mobile LIDAR. Several scans were performed over the same area to make sure sufficient data was recorded.

Pillar analyzed did not show any signs of failure such as major fractures, spalling, sloughing or other instability conditions that might represent a geomechanical issue or condition causing a hazard or risk. Two main discontinuity sets were identified during the visual inspections, the first



one was an incline discontinuity set that has a negative slope from left to right of the pillar, the other one was a vertical joint on the right of the pillar. A bedding plane was also observed on the top middle that has a dark-brown coloration (Figure 4.17).

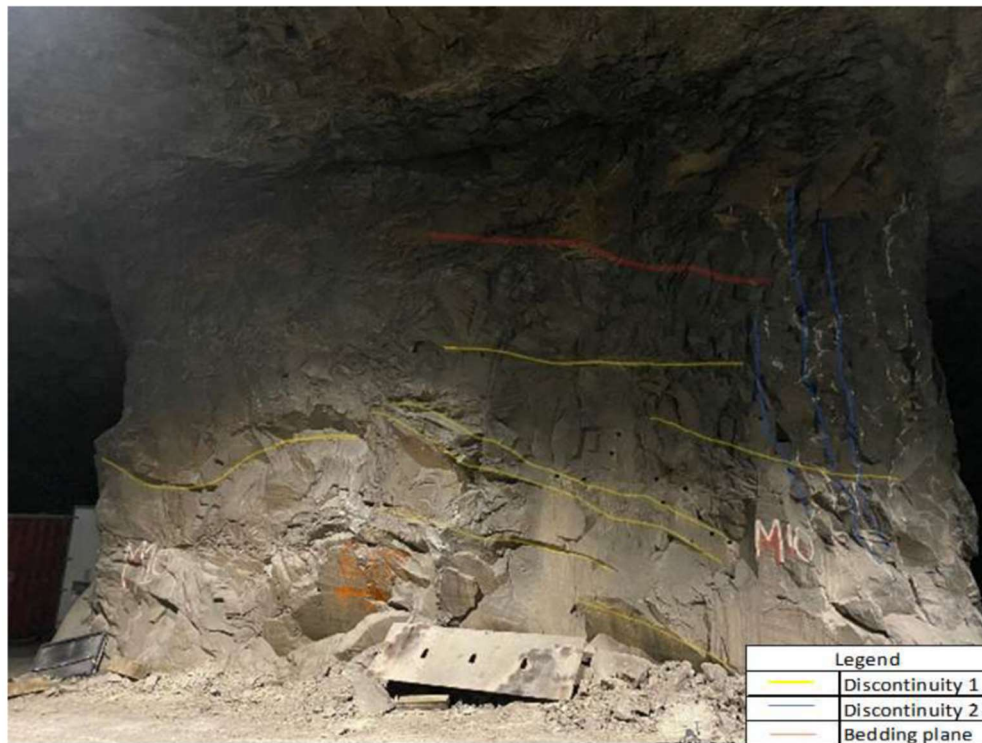


**Figure 4.17.** Underground stone mine pillar and highlighted discontinuities.

For this case study, the ZEB-HORIZON LiDAR scanner was used, and three loops were traversed around the pillar to obtain as much detail as possible from the section where the pillar to analyze is located, the information was uploaded to GEOSLAM Hub and the result can be visualized in Figure 4.18.

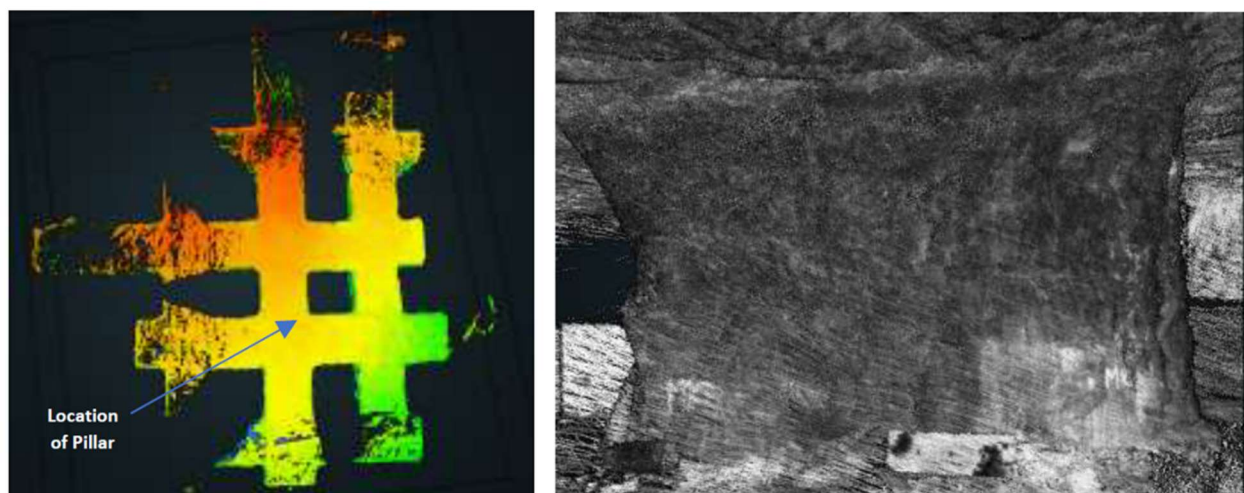


**Figure 4.18.** Point cloud processed by GEOSLAM Hub.



After extracting the pillar from the mine section in Cloud Compare (Figure 4.19) the dimensions of the pillar were measured and it was calculated that the point clouds for the analyzed pillar face have an area of  $122.7 \text{ m}^2$  and it is composed of 1,602,314-cloud points, resulting in a cloud point density of 1.3-cloud points per centimeter square. The point cloud of the pillar was visually assessed in GEOSLAM Hub and Cloud Compare, and although the pillar was shown with great detail in both programs it was not possible to visualize the discontinuities in any of them. The difficulty of observing the discontinuities that were identified in the field could be because the rock mass that compose the pillar seems to be massive, the traces of the discontinuities are not well represented in the point cloud.

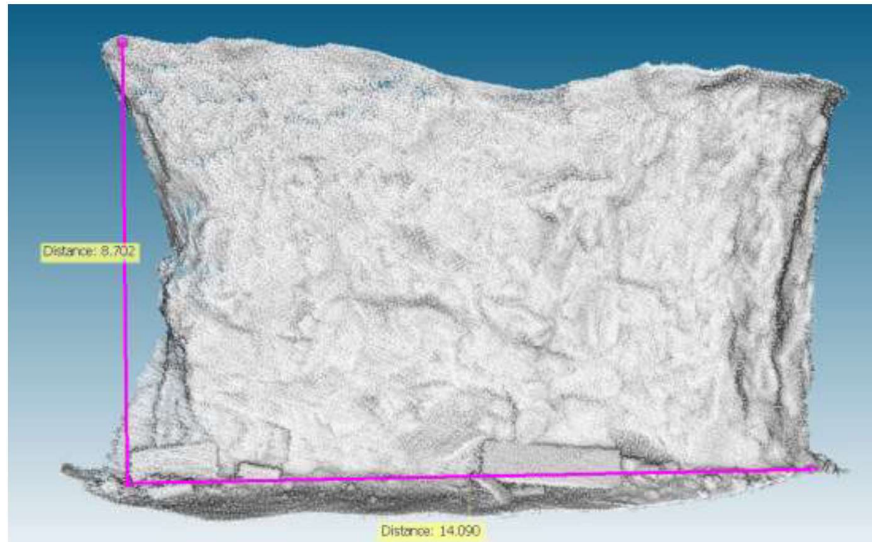


**Figure 4.19.** Pillar visualized in Cloud Compare.

Field Test #3: The Unmanned Aerial Vehicle (UAV) built by the WVU Robotic department performed a test run to assess the quality of the robotic mapping. Since the UAV uses both LiDAR and camera to scan the pillars, both accurate and RGB colored view of the pillar wall can be gathered and discontinuities, fractures or any other features can be extracted from the 3D scan data (Figure 4.20). Ground robot, Rhino, can provide the necessary lighting for the high-quality camera images (Figure 4.21).



**Figure 4.20** Pillar visualized in Cloud Compare after UAV tests (Samarakoon, 2022).



**Figure 4.21.** Rhino navigating in the NIOSH PMRD experimental underground mine.

Stone mine pillar module for stability mapping

In this section, the stone mine pillar module and associated software tools are applied to obtain the stress and safety factor analysis of a case study mine in the Loyalhanna Limestone formation. For testing the cell strength equations (Equations 3.14 and 3.23) for the stone mine stress gradient derived and implemented into LaModel in this research, operational data such as a topographic map, roof elevation data, mine map, and Uniaxial Compressive Strength (UCS) data was collected from the case study mine (Table 4.2). The case study mine is located at the Loyalhanna Limestone formation, where it dips at less than  $5^\circ$ . Thus, it is considered a flat-lying deposit.

**Table 4.2.** General mine information

General Mine Information	
<i>Average Pillar Width (ft)</i>	50
<i>Average Development Pillar Height (ft)</i>	27
<i>Average Benched Pillar Height (ft)</i>	50
<i>Average UCS (psi)</i>	29,401

Mine layout is shown in Figure 4.22. Also, from the mine information, there are two main benched areas. It is important to note that in this case study mine, pillar layout is design very successfully and both the development and benched pillars are stable and in good conditions. 17 yield zones are selected to accommodate the effect of different height pillars on the strength calculation. The UCS laboratory results provided by the mine are averaged to 29,401 psi. This is a value expected for the Loyalhanna Limestone that is usually 29,000 psi to 32,000 psi. The average width-to-height ratio of the pillars in the development stage is 1.85 and fully benched is 1.00 are larger than the minimum S-Pillar suggested value of 0.8 (Esterhuizen et al., 2011).

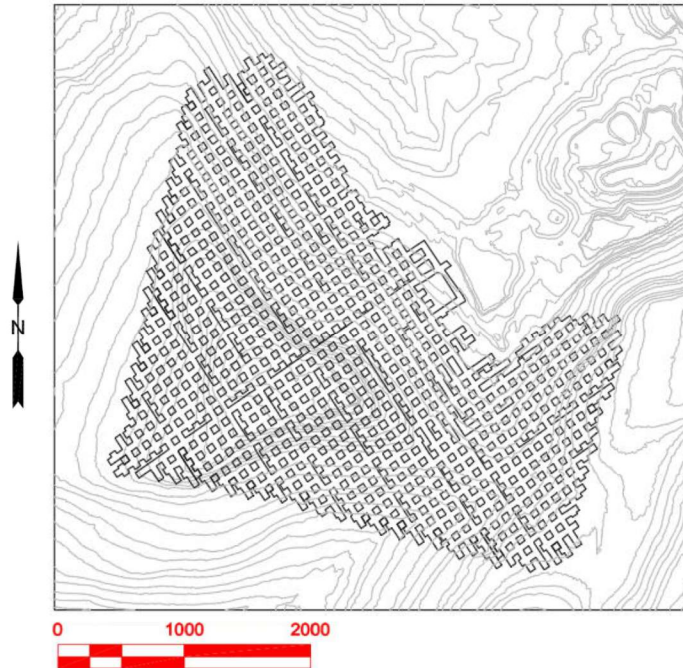


**Figure 4.22.** Mine topographic layout.

The topography elevation grid and the seam grid surface were generated from the elevation contours and the roof elevation contours provided by the mine. For generating the grid files, the Stability-Mapping program was used. The overburden grid was generated by subtracting the seam top elevation grid values from the surface elevation grid values. With the elevation grid and the seam grid obtained from the Stability-Mapping analysis, the cell strength equations are implemented for the case study mine in LaModel.

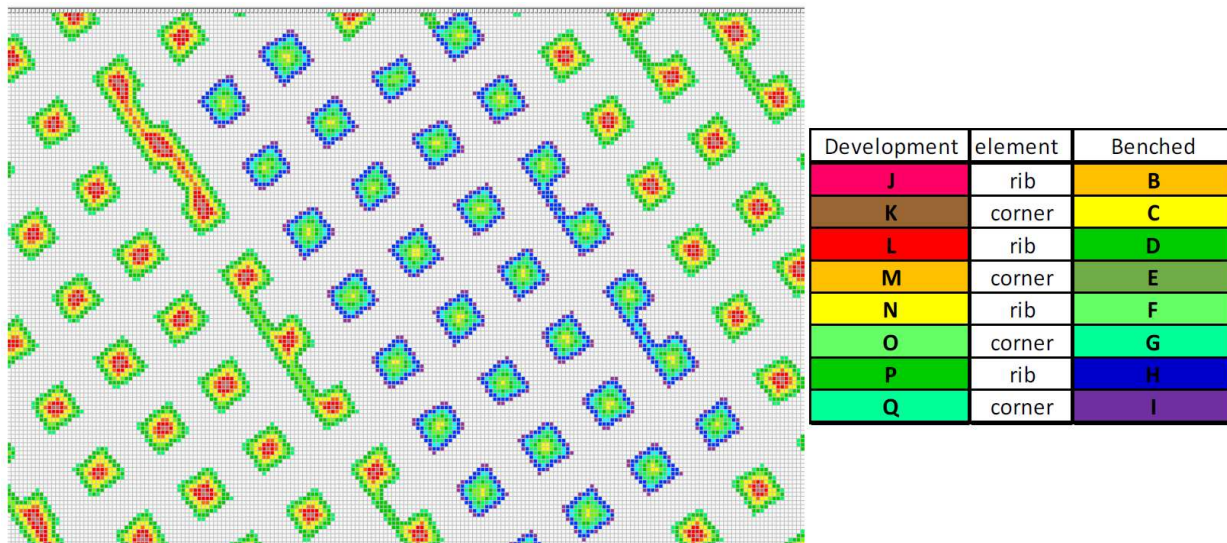


**Figure 4.23.** Element distribution for development and benched pillars in LaModel.

To implement the cell strength equations in the case study mine, two initial conditions were determined. First, since the pillars were 50 ft x 50 ft, the element size selected was 5 ft. Then, the



number of in-seam materials for the whole mine is determined. From the element and pillar size, a total of 8 in-seam elements are defined for each pillar, 4 rib cell elements, and 4 corner cell elements. Given that the input parameters for calculating the benched pillars are different than the development pillars, a different set of 8 in-seam materials for benched pillars is also defined in LaModel. Thus, 17 in-seam materials are defined for the whole mine grid, including development and benched pillars (Figure 4.23).

After the input file for the case study mine is created, the LaModel program is run to calculate the seam's stress and displacements. The stress outputs obtained for the case study mine in the Loyalhanna formation using the Boundary Element Method software LaModel are the overburden stress distribution, the total vertical stress on the seam, and stress safety factor of the stone mine pillars (Figure 4.24).

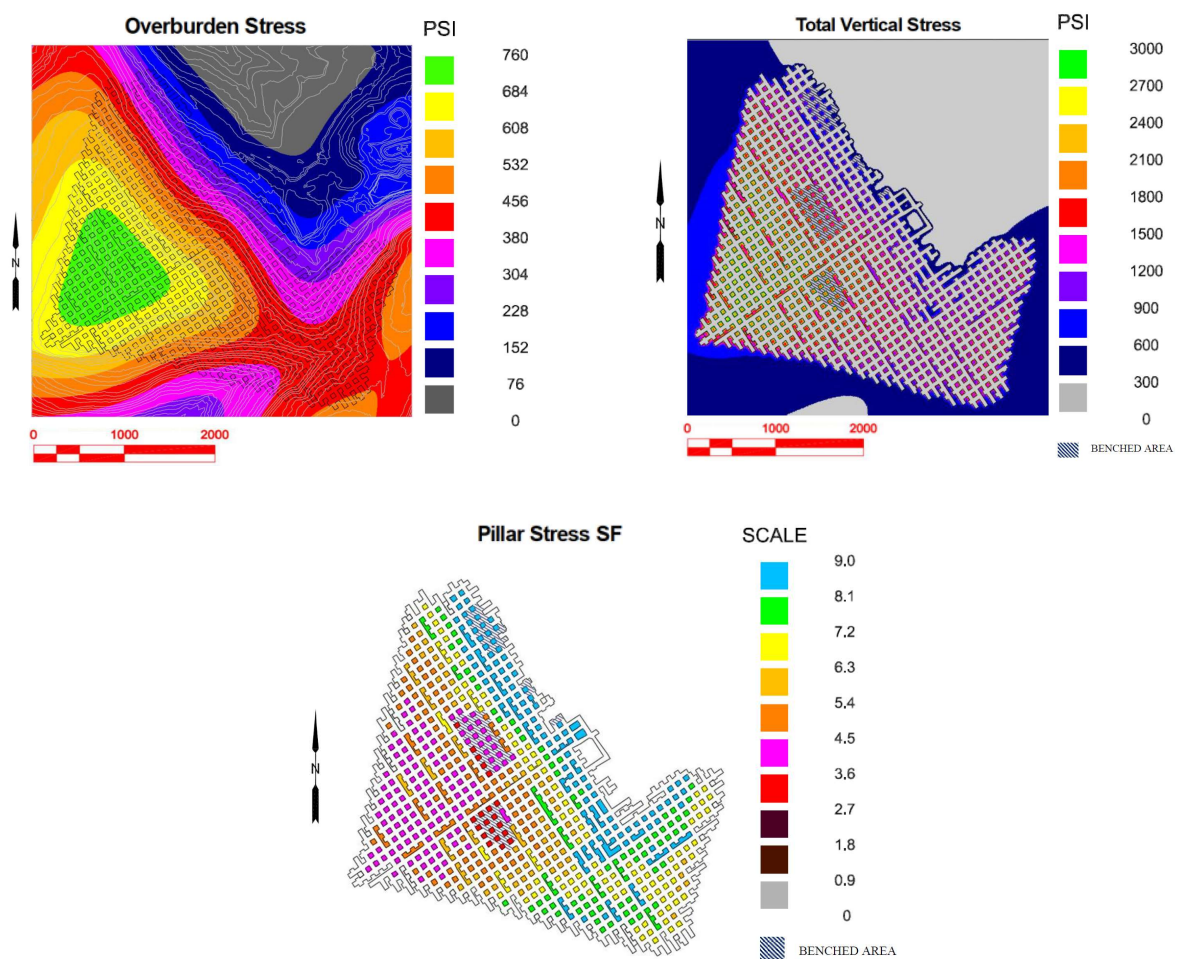


**Figure 4.24.** LaModel outputs, overburden stress, vertical stress, and stress safety factor.

Once the LaModel plots for the overburden stress distribution, vertical stress on the seam, and stress safety factor using the cell strength equations are obtained, the software S-Pillar is used to compare pillar stress and safety factor results for the case study mine. From Figure 4.23, the maximum overburden stress contour is 760 psi. This value is used to calculate the maximum

overburden depth by assuming a 1.125 psi/ft vertical stress gradient. The Maximum Overburden Depth calculated from the overburden stress distribution from LaModel is used as an input parameter in the S-Pillar (Esterhuizen et al., 2011). The S-Pillar uses the maximum overburden depth of the mine to obtain the safety factor results on the benched and development pillars. The results of S-Pillar analysis for the case study mine are presented in Figure 4.25.

S-Pillar calculated the development factor of safety, under the deepest cover, as 4.17. From Figure 4.24, it can be seen that under the deepest cover LaModel safety factor contours are ranging from 4.5 to 3.5, and similar results are calculated. Since LaModel analysis used the actual mine map and at the time of analysis there wasn't any benched pillar under the deepest cover, safety factors calculated at the benched areas of the mine different than S-Pillar results. Therefore, with the integration of the cell strength equations into the BEM software LaModel, more accurate representation of pillar safety factors, and stresses of a mine layout can be calculated. Additionally, this methodology allows the estimation of stress changes near the benched areas during the progressive benching stages in underground stone mines (Figure 4.24).

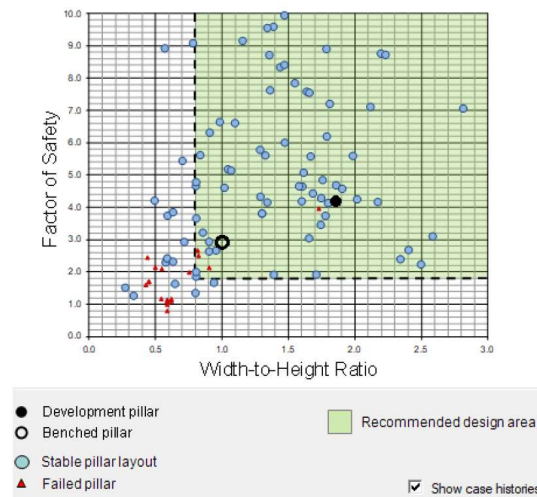


**Figure 4.25.** *S-Pillar results for the case study mine.*

The local large discontinuity factor (LLDF) approach developed in this research is also tested in this underground limestone case study mine. LLDF approach requires the knowledge of the distribution of large discontinuities on the mine layout. This information can be gathered from geological surveys or by using advanced surveying like UAVs or a robotic system as described in the previous section (or, Bendezu, 2021; Bishop, 2022). In this application, a theoretical distribution was generated for the mine layout to demonstrate the LLDF approach. This theoretical large discontinuity distribution was selected according to observations of Esterhuizen et al. (2011) and the characteristics of the formation.



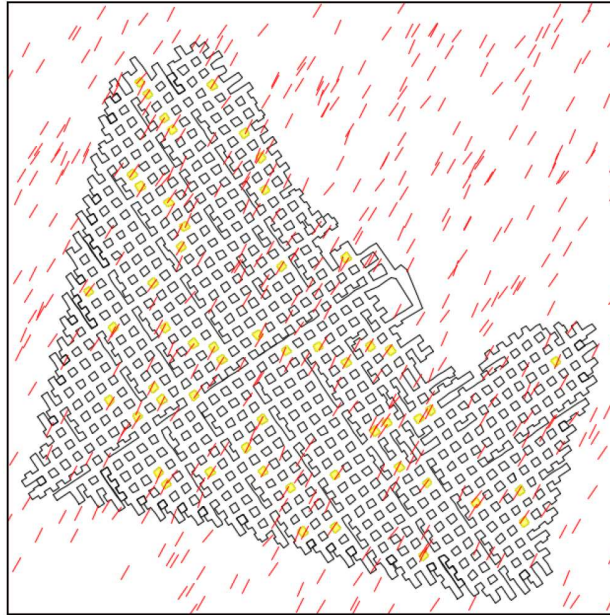


**Figure 4.26.** Discontinuities and intersected pillars.

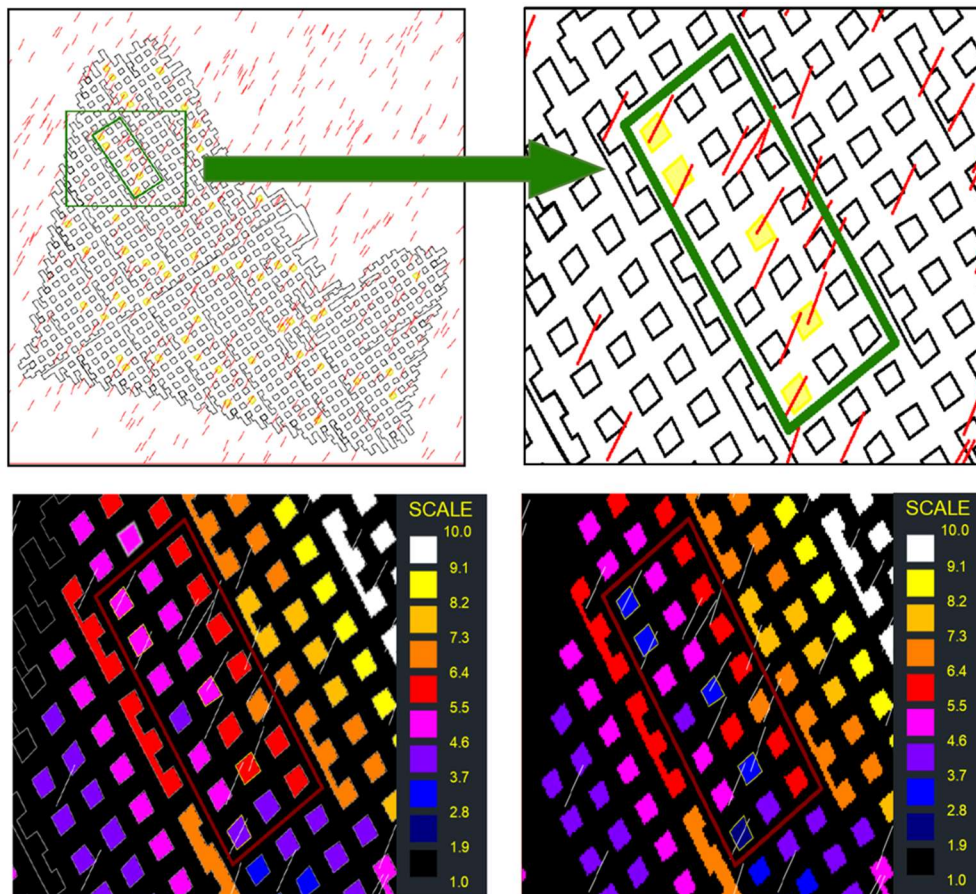


**Figure 4.27.** Application of the LLDF approach.

Large discontinuity distribution (red lines in Figure 4.26) and a grid file for intersected pillars (yellow pillars in Figure 4.26) are generated using the integrated stability mapping software to implement LLDF calculations in the case study mine. Large discontinuities are distributed using the negative exponential distribution on the area of mine grid to give average frequency factor of 0.1 large discontinuities per pillar (Esterhuizen et al, 2011). Dip of the large discontinuity set was set to 60° and strike of the large discontinuity set was defined as approximately N 45° E based on the observations of Iannacchione and Coyle (2002). There are 55 intersected pillars over 525 total development pillars. Integrated stability mapping software identifies pillars that are intersected by the large discontinuities and generates the LLDF grid file by using the area-based step transformation method (Ates, 2022).

The computer code developed in this study reads LLDF grid and LaModel output files and finds the intersected pillars in the LaModel output file by taking the grid file as a reference. The discontinuity dip factors are encoded on the code, and user is required to enter dip angle of the large discontinuity set and pillar width-to-height ratio to run the code. By entering the necessary input parameters and selecting the LLDF grid file, the code applies discontinuity dip factors to the intersected pillars and calculates new safety factors. After this calculation, the code updates the pillar safety factors in the LaModel output file to generate the final pillar stress safety factor output. This final output file is suitable for visualization in both AutoCAD and LaModel software. Final stage of the LLDF approach is to select the local area on the mine pillar layout to calculate the average safety factor of the pillars in the specified location. To be able to better illustrate the LLDF approach, calculations are demonstrated on a local area in the case study mine pillar layout that consists of 21 pillars as shown in Figure 4.27, figure at the top.

Bottom figures in Figure 4.27 shows how the safety factor reduction is applied to the intersected pillars. The safety factors of the intersected pillars are reduced approximately 40%. LLDF approach allows the mine engineers to identify potential hazards due to the large discontinuities by explicitly considering the spatial distribution of the large discontinuities in a mine layout, whereas S-Pillar software LDF factor averages the influence of large discontinuities along the whole mine layout.

As stated in the previous section, frequency of large discontinuities per pillar is theoretically selected as 0.1, and discontinuity dip factor is assigned to 0.34 (pillar width-to-height ratio of 1.0 and dip angle of 60°). We can calculate the LDF of the mine layout using Equations 4.6 as:

$$LDF = 1 - 0.34 \times (e^{-0.1}) = 0.97 \quad (4.6)$$

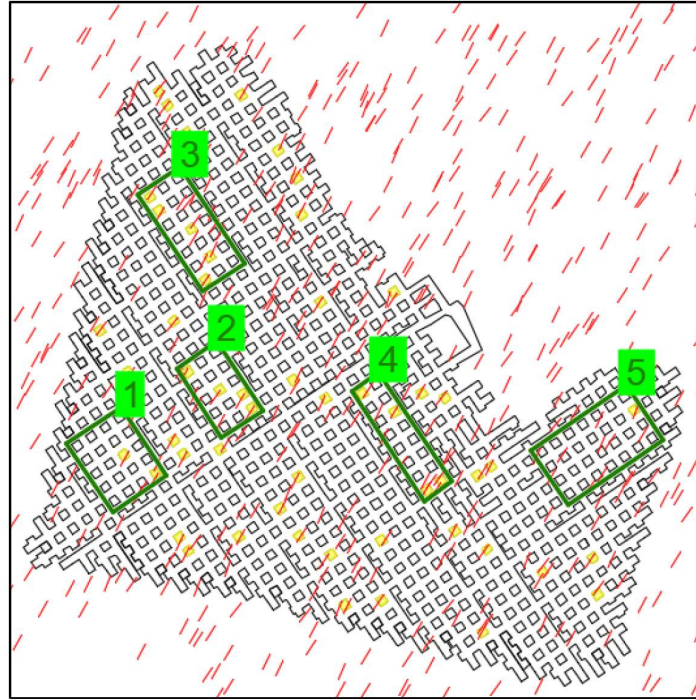


**Figure 4.28.** Selected areas in the Loyalhanna Limestone Mine layout.

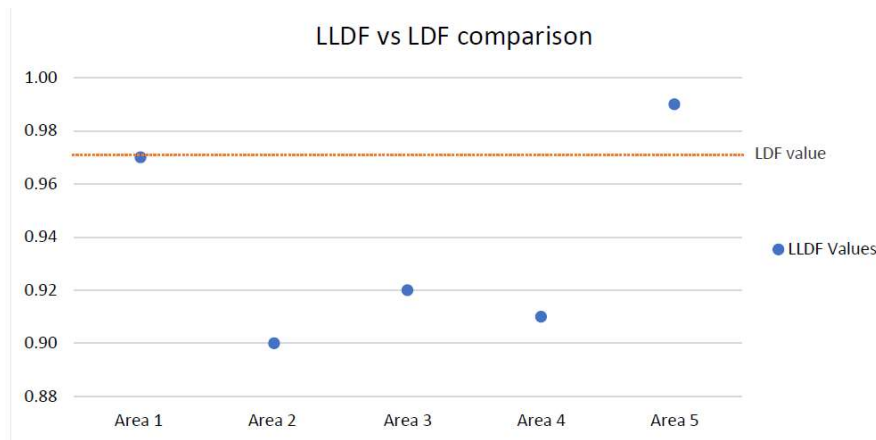


**Figure 4.29.** The illustration of the comparison between LLDF and LDF.

Therefore, in S-pillar approach for the given parameters of this case study, safety factor of the pillars is reduced by 3% in average. The LLDF is computed for five local areas (Figure 4.28). Figure 4.29 illustrates the differences of the LDF and the LLDF where the orange line represents the LDF equal to LLDF values and blue points are the LLDF coefficients. When the LLDF results are compared with LDF calculations, although there isn't such a large difference between the LLDF and LDF results for the case study mine, results demonstrated the potential impact of applying LLDF on stone mine pillar stability. Implementation of the software tool will improve measures to address pillar failures and provide safer mine operations. LLDF makes it possible to know more about the effects of discontinuities, to assess the hazards on local sections, to predict future scenarios and provide a safer environment for miners.

### An approach for time-dependent strength degradation adjustment

As it was discussed in the Section 3, research objective 2.2, underground stone mine rock mass generally contains two joint sets perpendicular to each other. Two different conceptual DFNs realizations consisting of two perpendicular joint sets are generated to be consistent with the field observations. The joint frequency number( $P_{10}$ ) is set to 1.0 for all conceptual realizations. However, the joint trace length is varied using a log-normal distribution with mean values of 0.5  $m$  and 1.0  $m$ , consistent with field observations. The normal distribution for vertical and horizontal joints orientations, with  $90^\circ$  and  $0^\circ$  dip angles are assumed. Also, the uniformly distributed position assumption is applied in the DFNs generation scheme.

The homogenization process explained in Section 3, research objective 2.2, of this research is applied. Figures 4.30 to 4.32 show the change of normalized pillar strength as a function of pillar width for low, medium, and high strength rock categories. Normalized strength calculated as the model estimated strength over UCS. In addition to the S-Pillar pillar strength equation represented with orange line and dots, power strength equations of Hedley and Grant (1972) with a green line and Von Kimmelmann (1984) with magenta color, are also presented in the figures. The numerically estimated pillar strength and the strength reduction trend as a function of size increment in each strength group are found to be in good agreement with the literature.

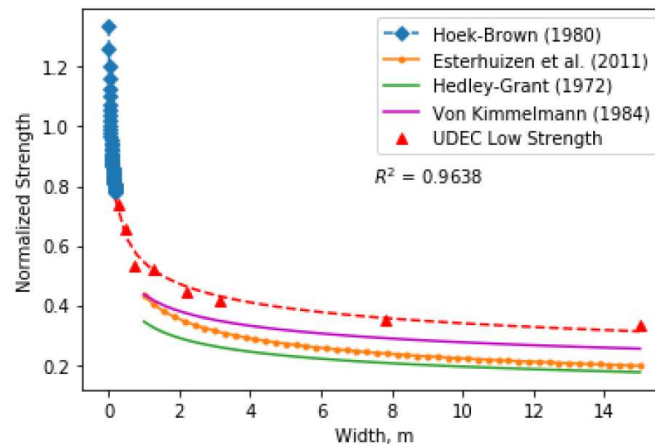


**Figure 4.30.** Low Strength Up-Scaling Behavior Captured by UDEC among the Literature.



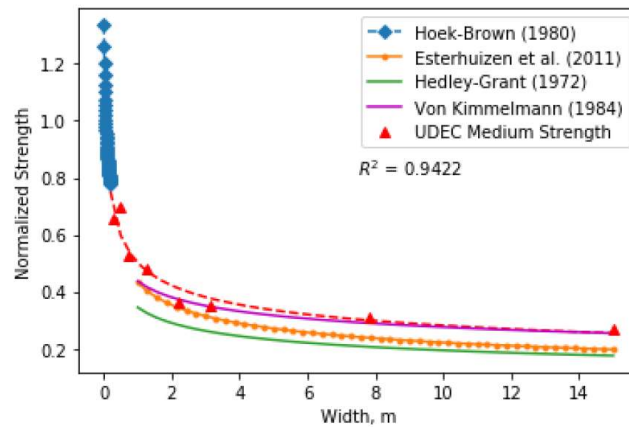


**Figure 4.31.** Medium Strength Up-Scaling Behavior Captured by UDEC among the Literature.

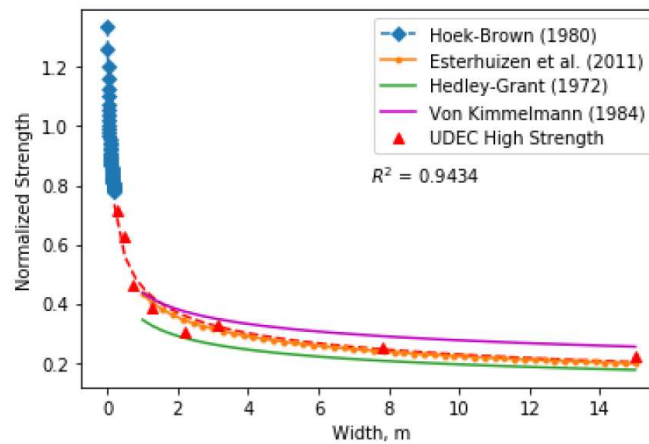


**Figure 4.32.** High Strength Up-Scaling Behavior Captured by UDEC among the Literature.

Figures from 4.33 to 4.35 summarizes the UDEC estimated pillar strengths for various width-to-height ratios. Empirical equations are also included in these graphs. Pillar strengths are normalized with UCS to eliminate biases arising from the intact rock strength differences. Good agreement is achieved for the pillar strength prediction by using the proposed methodology in the UDEC. The low-strength rock groups are shown in Figure 4.33. UDEC predicted strengths higher than the empirical equations. In the S-Pillar database, there is not any failed pillar case reported for low-strength rock masses. However, during the derivation of the pillar strength equation for stone mines, average intact rock strength of all strength categories is used. During the statistical analyses of the S-Pillar database, it is observed that combined RQD and joint spacing rating is the highest in the low strength rocks when compared to other strength groups. Esterhuizen (personal communications, March 26, 2021) indicated that the stone mines having the high-strength intact rock are suffering from structurally controlled failure. Also, it is supported by Esterhuizen et al. (2019) that the Loyalhanna formation (a high-strength limestone rock formation) has well-developed joint sets due to folding in the Appalachian Plateau causing to form joint sets and faults.



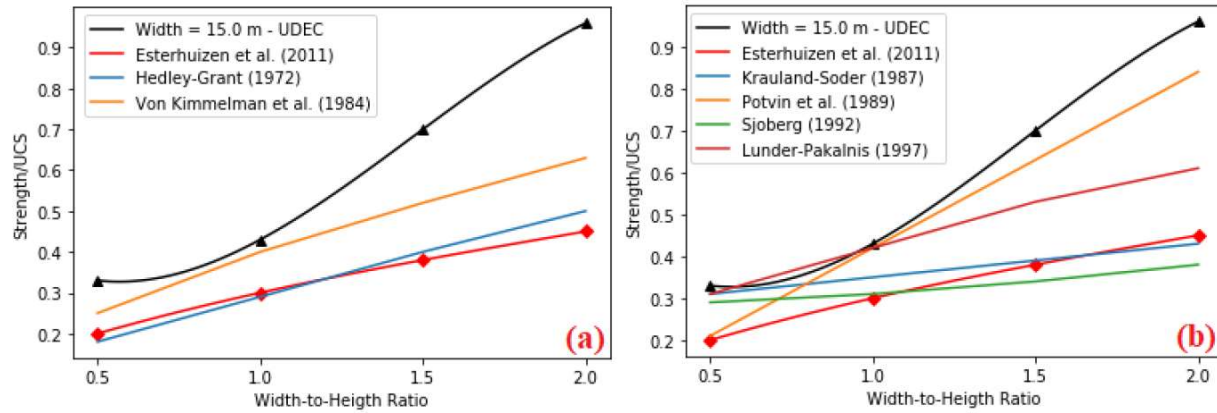


**Figure 4.33.** Low Strength Limestone Rocks with Various Width-to-Height Ratio - Width 15.0 m in Pillar Stability Charts: a) Power Strength Estimation Equations; b) Linear Strength Estimation Equations.

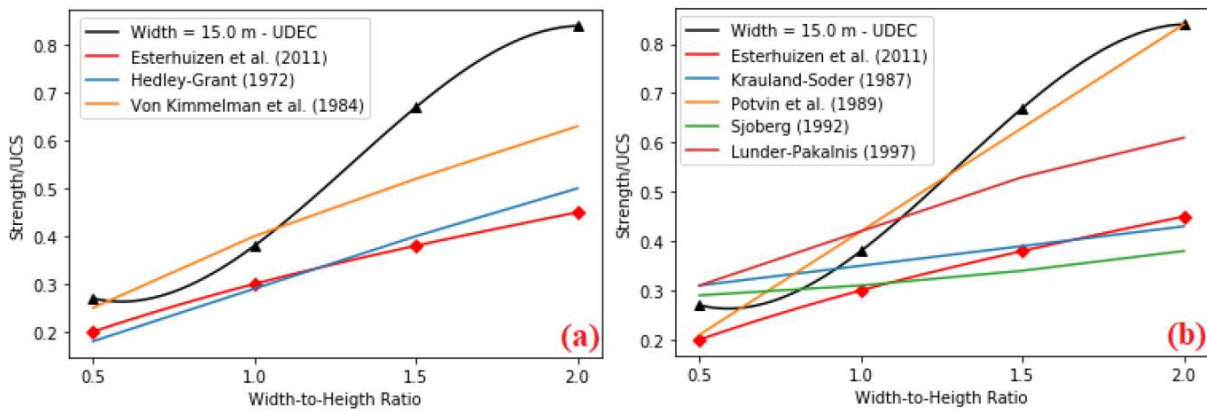


**Figure 4.34.** Medium Strength Limestone Rocks with Various Width-to-Height Ratio – Width 15.0 m in Pillar Stability Charts: a) Power Strength Estimation Equations; b) Linear Strength Estimation Equations.

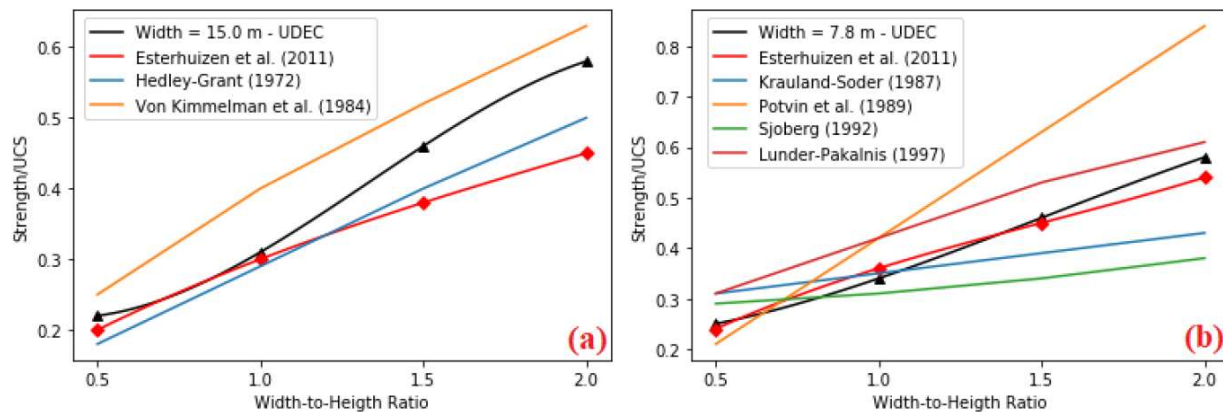


**Figure 4.35.** High Strength Limestone Rocks with Various Width-to-Height Ratio – Width 15.0 m in Pillar Stability Charts: a) Power Strength Estimation Equations; b) Linear Strength Estimation Equations.

Overall, the study explained the pillar strength and the failure mechanisms with explicit consideration of the naturally existing joint sets. There is not any accepted methodology to estimate the long-term time-dependent strength of the underground stone mine pillars. The creep behavior due to the stress corrosion should be studied with the crack length of the fracture developments, confinement rate, and the rock toughness to explain the stress-corrosion-based strength degradation as proposed by Damjanac and Fairhurst (2010), and Damjanac et al. (2012). Damage progress can be monitored with time-lapse scans using the robotic system stress-corrosion-based strength degradation approach can be established by the back analysis, using the modeling methodology developed in this research (Figure 4.36).

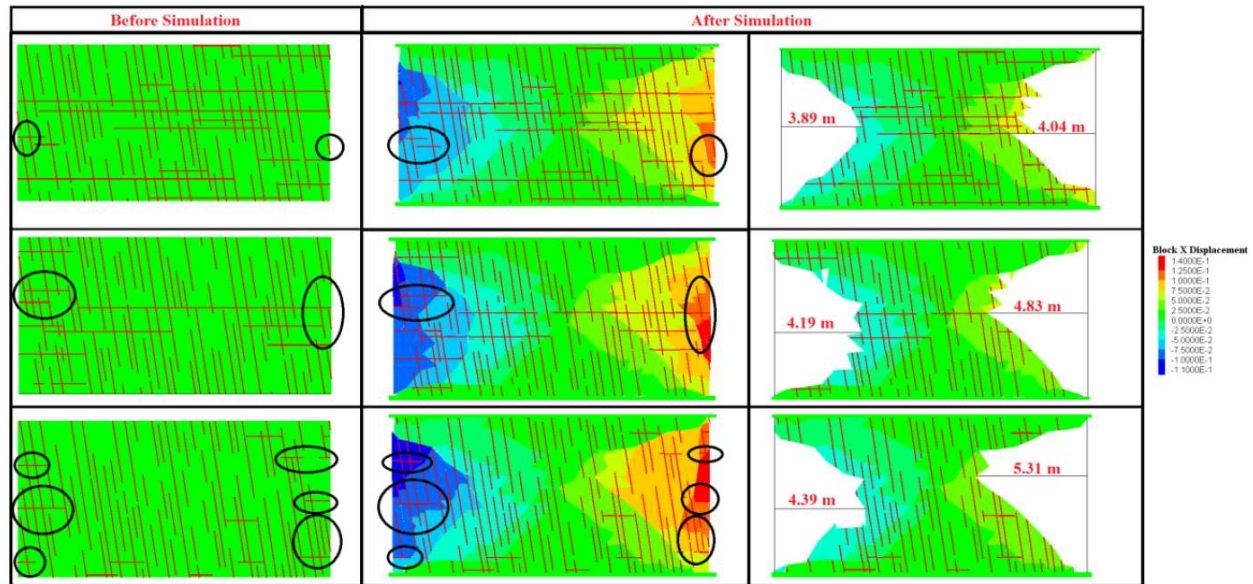


**Figure 4.36.** Back analysis using the modeling methodology developed in this research.

## 5.0 Publication Record and Dissemination Efforts:

1. Lima, R. R., & Pereira, G. A. (2023). A Multi-model framework for Tether-based Drone Localization, *Journal of Intelligent & Robotic Systems* (Under Review).
2. Rocamora, B. M., Lima, R. R., Samarakoon, K., Rathjen, J., Gross, J. N., & Pereira, G. A. (2023). Oxpecker: A Tethered UAV for Inspection of Stone-Mine Pillars. *Drones*, 7(2), 73.
3. Samarakoon, K. Y., Pereira, G. A., & Gross, J. N. (2022, June). Impact of the Trajectory on the Performance of RGB-D SLAM Executed by a UAV in a Subterranean Environment. In *2022 International Conference on Unmanned Aircraft Systems (ICUAS)* (pp. 812-820). IEEE.
4. Lima, R. R., & Pereira, G. A. (2022, June). Drone Collision Detection and Classification using Proprioceptive Data. In *2022 International Conference on Unmanned Aircraft Systems (ICUAS)* (pp. 562-569). IEEE.
5. Lima, R. R., & Pereira, G. A. (2021, June). On the development of a tether-based drone localization system. In *2021 International Conference on Unmanned Aircraft Systems (ICUAS)* (pp. 195-201). IEEE.
6. Gonçalves, V. M., McLaughlin, R., & Pereira, G. A. (2020). Precise landing of autonomous aerial vehicles using vector fields. *IEEE Robotics and Automation Letters*, 5(3), 4337-4344.
7. Suner, M.C., Tulu, I.B. Examining the Effect of Natural Fractures on Stone Mine Pillar Strength Through Synthetic Rock Mass Approach. *Mining, Metallurgy & Exploration* (2022). <https://doi.org/10.1007/s42461-022-00649-2>
8. Suner, M.C., Tulu, I.B. Pillar Strength Estimation of Underground Stone Mines with Numerical Simulations. 41st International Conference on Ground Control in Mining, Canonsburg, PA, July, 2022.
9. Suner, M., Tulu IB, “Stochastic Sampling on Synthetic Rock Mass to Study Effect of Natural Joints on Pillar Mechanics.” 40th International Conference on Ground Control in Mining, Virtual, 2021.
10. Escobar, S., & Tulu, I. B. (2021). Calculating Stone Mine Pillar Concentric Ring Zone Capacities for Boundary Element Modeling. American Rock Mechanics Association.
11. Ihsan Tulu, J. Gross, Y. Gu and G. Pereira. “Autonomous Robotic Early Warning System for Underground Stone.” SME Annual Conference and Expo, Phoenix, Arizona, February, 24, 2020.
12. Ihsan Berk Tulu. “Robotic System to Inspect Stone Mine Pillars.” SME/PCMIA Annual Joint Meeting, Pittsburgh, Pennsylvania, October, 21, 2021.
13. Mario Bendezu, Ihsan Tulu. “Semi-automatic geotechnical characterization of pillars in stone mines with autonomous robotic system.” SME Annual Conference and Expo, Virtual, 2021.
14. M. Suner and I. Tulu. “Stochastic Sampling on Synthetic Rock Mass to Study Effect of Natural Joints on Pillar Mechanics.” SME Annual Conference and Expo, Salt Lake City, UT, February 28, 2022.
15. S. Escobar and I. Tulu. “Calculating Stone Mine Pillar Concentric Ring Zone Capacities for Boundary Element Modeling.” SME Annual Conference and Expo, Salt Lake City, UT, March 01, 2022.

16. Ihsan Berk Tulu. “WVU Stone Mine Pillar Stability Research.” MSHA Roof Control Division Roundtable, November, 2021.
17. Mustafa Suner and Ihsan Berk Tulu. “Application of Synthetic Rock Mass to Study Stone Mine Pillars.” NIOSH Geotechnical Modeling COP Meeting, March, 3, 2021.
18. Rosbel Jimenez and Ihsan Berk Tulu “Development of a wizard for the implementation of empirical strength equations in stone mines in the U.S.” SME Annual Conference and Expo, Denver, CO, February 28, 2023.

## 6.0 Conclusions and Impact Assessment:

The research presented here has several significant results that will undoubtedly improve the quality of the ground control design and safety of mine workers in the United States in the future, particularly for underground stone mining sector. During this research study, a proof-of-concept of an autonomous robotics system, shown in Figure 3.1, composed of an unmanned ground vehicle (UGV), called Rhino, and a tethered unmanned aerial vehicle (TUAV), known as Oxpecker, was developed. This robotic system was tested in different underground mining environments and is a TRL 7 technology. In addition to this new technology, this research project produced a practical stone mine pillar design framework and accompanying software tool that utilizes the empirical stone mine pillar equation, Large Discontinuity Factor (LDF), AutoCAD ObjectARX add-in Integrated Stability Mapping Software (ISMS), and LaModel software. The application of this new approach and beta version of the software were demonstrated in this report.

The ground robot, Rhino, can autonomously operate more than 6 hours with a single battery cycle. Tethered design allows the UAV, Oxpecker, work in tandem with the UGV and able to operate for several hours without human intervention and to precisely land on the Rhino. A tether-powered UAV has the payload capacity to carry localization and 3D mapping sensors and the weight of the released power cable. Tethered system manages the cable release and retraction and that assists the drone localization and landing by measuring relevant variables. The coverage software on Oxpecker is designed to survey and map the face of a pillar or wall by executing a predefined trajectory with a sweeping pattern. Oxpecker uses both LiDAR and camera to scan the pillars, both accurate and RGB colored view of the pillar wall can be gathered and discontinuities, fractures or any other features can be extracted from the 3D scan data. Ground robot, Rhino, also provides the necessary lighting for the high-quality camera images.

This research extended the application of S-Pillar design approach to the BEM to allow stone mine operators to integrate overburden stress distribution under variable topography and pillar layouts with irregularly sized pillars into their designs. In addition to this new development, the new term Local Large Discontinuity Factor (LLDF) is proposed to explicitly account for the impact of large discontinuities on local intersected pillar stability. The LLDF enables the stone mine operators to incorporate impact of spatial distribution of large discontinuities on the pillar stability and to identify the hazards in local areas on the mine layout. The software tool developed in this thesis incorporates the large discontinuity impacts, overburden stress distribution under variable topography by integrating S-Pillar approach with Integrated Stability Mapping Software (ISMS) and LaModel. This research also developed a Synthetic Rock Mass (SRM) approach to explain the pillar strength and failure mechanism with the explicit consideration of naturally existing joint sets in the stone mines. Pillar strengths predicted by the SRM approach developed in this research are in good agreement with the stone pillar strength equation published by NIOSH.

Finally, the robotic system and practical design tool and methods developed during this research are immediately available to the mining industry, Mine Safety and Health Administration (MSHA), National Institute for Occupational Safety and Health (NIOSH), and State agencies to evaluate and consider for application in the ground control design process.



## 7.0 Recommendations for Future Work:

The following research are recommended for future work based on the findings from this research project where TRL 7 proof of concept robotic technology and pillar design framework with accompanying software tools were developed:

- Esterhuizen et al. (2011) stated that in underground stone mines, rooms are on average 44-ft wide, and the desired roof span dimensions are generally predetermined by the operational requirements, the size of the mining equipment, etc. The roof design in stone mines is generally focused on optimizing the stability of the roof under the usual rock mass conditions, and an unsupported roof is common in underground stone mines due to the inherently strong rock mass. Operators generally support the roof based on their experience in the mine if they encounter a geological condition or geological structure. Esterhuizen et al. (2011) stated that large roof falls were observed at 19 mine operations visited during the development of the roof span design guidelines. They reported that high horizontal stress contributed to 36%, failure of the weak band / parting plane within the roof beam contributed to 28%, large discontinuities contributed to 21% and failure of weak immediate roof strata contributed to 15% of all roof falls. NIOSH roof span design guidelines recommend stone mine operators should conduct detailed geotechnical characterization of the mine since the discontinuities play a major role in roof stability and should monitor changes in rock mass conditions. Therefore, successful roof support design depends on accurate identification of the geological structures and recognition of the adverse changes in rock mass conditions in the stone mines, and failure to recognize these hazards caused many massive roof fall accidents, the most recent fatal accident happened on January 2022 in the mine operating in Loyalhanna formation. We recommend adaptation of a sensory subsystem to the UAV developed in this project that allows mine operators to inspect stone mine roofs through high-resolution pictures or point clouds would help the identification of the roof fall hazards.
- We recommend development of a database of high-resolution 3D maps of stone mine layouts from different mining operations to develop guidelines for stone mine operators to evaluate pillar stability of old workings and roof fall hazards from a UAV and/or UGV captured high-resolution 3D point clouds and geomechanical data,
- We recommend development of a stand-alone stability mapping package. Current design approach developed in this project utilizes multiple design software to generate results.
- We recommend a research that will target (i) extension of the stone mine pillar concentric zone capacities derived by Escobar and Tulu (2021) to semi benched pillars, (ii) development of laminated overburden model calibration method for stone mine stress analysis, and (iii) development of simplified stone mine roof hazard index that would be a function of horizontal stress, discontinuity condition, roof beam thickness, and pillar stability.

## 8.0 References:

1. MSHA (2021). Assessing Pillar Collapse and Airblast Hazards in Underground Stone Mines Retrieved from Mine Safety and Health Administration (MSHA): <https://www.msha.gov/news-media/special-initiatives/2021/10/29/pillar-collapse-initiative>
2. MSHA. (2016). Mine Data Retrieval System (Accident Injuries Data Set). Retrieved from Mine Safety and Health Administration (MSHA): <https://www.msha.gov/mine-data-retrieval-system>
3. Li, J., Du, Z., Ruther, R. E., An, S. J., David, L. A., Hays, K., Wood, M., Phillip, N. D., Sheng, Y., Mao, C., et al. (2017). Toward low-cost, high-energy density, and high-power density lithium-ion batteries. *Jom*, 69(9):1484–1496.
4. Mulgaonkar, Y.; Whitzer, M.; Morgan, B.; Kroninger, C.M.; Harrington, A.M.; Kumar, V. Power and weight considerations in small, agile quadrotors. In *Proceedings of the Micro- and Nanotechnology Sensors, Systems, and Applications VI*, Baltimore, MD, USA, 5–9 May 2014; SPIE: Bellingham, WA, USA, 2014; Volume 9083, pp. 376–391.
5. Foehn, P.; Kaufmann, E.; Romero, A.; Penicka, R.; Sun, S.; Bauersfeld, L.; Laengle, T.; Cioffi, G.; Song, Y.; Loquercio, A.; et al. Agilicious: Open-source and open-hardware agile quadrotor for vision-based flight. *Sci. Robot.* 2022, 7, eabl6259.
6. Koubâa, A.; Allouch, A.; Alajlan, M.; Javed, Y.; Belghith, A.; Khalgui, M. Micro air vehicle link (mavlink) in a nutshell: A survey. *IEEE Access* 2019, 7, 87658–87680.
7. Ermakov, V. MAVROS. 2020. Available online: <https://github.com/mavlink/mavros> (accessed on 1/18/2023).
8. Rocamora, B. M., Lima, R. R., Samarakoon, K., Rathjen, J., Gross, J. N., & Pereira, G. A. (2023). Oxpecker: A Tethered UAV for Inspection of Stone-Mine Pillars. *Drones*, 7(2), 73.
9. Shan, T., Englot, B., Meyers, D., Wang, W., Ratti, C., and Rus, D. (2020). Lio-sam: Tightly-coupled lidar inertial odometry via smoothing and mapping. In *2020 IEEE/RSJ international conference on intelligent robots and systems (IROS)*, pages 5135–5142. IEEE
10. Oleynikova, H., Taylor, Z., Fehr, M., Siegwart, R., and Nieto, J. (2017). Voxblox: Incremental 3d euclidean signed distance fields for on-board mav planning. In *2017 IEEE/RSJ International Conference on Intelligent Robots and Systems (IROS)*, pages 1366–1373. IEEE.
11. Zhang, J., Hu, C., Chadha, R. G., and Singh, S. (2020). Falco: Fast likelihood-based collision avoidance with extension to human-guided navigation. *Journal of Field Robotics*, 37(8):1300–1313
12. Tatsch, C. A. A. (2020). Route Planning for Long-Term Robotics Missions. West Virginia University.
13. Yamauchi, B. (1997). A frontier-based approach for autonomous exploration. In *Proceedings 1997 IEEE International Symposium on Computational Intelligence in Robotics and Automation CIRA'97. 'Towards New Computational Principles for Robotics and Automation'*, pages 146–151. IEEE.
14. Bircher, A., Kamel, M., Alexis, K., Oleynikova, H., and Siegwart, R. (2016). Receding horizon” next-best-view” planner for 3d exploration. In *2016 IEEE international conference on robotics and automation (ICRA)*, pages 1462–1468. IEEE.

15. Cao, C., Zhu, H., Choset, H., and Zhang, J. (2021). Tare: A hierarchical framework for efficiently exploring complex 3d environments. In *Robotics: Science and Systems*.
16. Lima, R. R., & Pereira, G. A. (2023). A Multi-model framework for Tether-based Drone Localization, *Journal of Intelligent & Robotic Systems* (Under Review).
17. Samarakoon, K. Y., Pereira, G. A., & Gross, J. N. (2022, June). Impact of the Trajectory on the Performance of RGB-D SLAM Executed by a UAV in a Subterranean Environment. In *2022 International Conference on Unmanned Aircraft Systems (ICUAS)* (pp. 812-820). IEEE.
18. Lima, R. R., & Pereira, G. A. (2022, June). Drone Collision Detection and Classification using Proprioceptive Data. In *2022 International Conference on Unmanned Aircraft Systems (ICUAS)* (pp. 562-569). IEEE.
19. Lima, R. R., & Pereira, G. A. (2021, June). On the development of a tether-based drone localization system. In *2021 International Conference on Unmanned Aircraft Systems (ICUAS)* (pp. 195-201). IEEE.
20. Gonçalves, V. M., McLaughlin, R., & Pereira, G. A. (2020). Precise landing of autonomous aerial vehicles using vector fields. *IEEE Robotics and Automation Letters*, 5(3), 4337-4344.
21. Ates, M. (2022): "Integrated Large Discontinuity Factor, Lamodel and Stability Mapping Approach for Stone Mine Pillar Stability", West Virginia University, 2022.
22. Bendezu de la Cruz, Mario Alejandro, "Evaluation of LIDAR systems for rock mass discontinuity identification in underground stone mines from 3D point cloud data", West Virginia University, 2021.
23. Bishop, R. "Applications and Development of Intelligent UAVs for the Resource Industries", Virginia Tech, 2022. <https://vtechworks.lib.vt.edu/10919/109724>
24. Escobar, Samuel, and Ihsan Berk Tulu. (2021): "Calculating Stone Mine Pillar Concentric Ring Zone Capacities for Boundary Element Modeling". Paper presented at the 55th U.S. Rock Mechanics/Geomechanics Symposium, Virtual, June 2021.
25. Escobar, Samuel, "Implementing the Empirical Stone Mine Pillar Strength Equation into the Boundary Element Method Software LaModel" (2021). Graduate Theses, Dissertations, and Problem Reports. 10273. <https://researchrepository.wvu.edu/etd/10273>
26. Esterhuizen, G., Dolinar, D., Ellenberger, J., & Prosser, L. (2011). *Pillar and Roof Span Design Guidelines for Underground Stone Mines*. Pittsburgh: National Institute for Occupational Safety and Health.
27. Esterhuizen, G. (2021). Personal Communications.
28. National Institute for Occupational Safety and Health. (2022). Mining Project: Underground Stone Mine Pillar Design in Challenging Conditions. Retrieved from [https://www.cdc.gov/niosh/mining/researchprogram/projects/project\\_undergroundstoneminepillardesigninchallengingconditions.html](https://www.cdc.gov/niosh/mining/researchprogram/projects/project_undergroundstoneminepillardesigninchallengingconditions.html)
29. Mark, C., & Iannacchione, A. T. (1992). Coal pillar mechanics: theoretical models and field measurements compared. In *Proceedings of the Workshop on Coal Pillar Mechanics and Design*. Pittsburgh, PA: US Department of the Interior, Bureau of Mines, IC (Vol. 9315, pp. 78-93). Johnson et al. (2014)

30. Esterhuizen, G., Dolinar, D., & Ellenberger, J. (2008). Pillar Strength and Design Methodology for Stone Mines. *Proceedings of the 27th International Conference on Ground Control in Mining*, (pp. 241-253). Morgantown, WV, U.S.A. Preston et al., (2015)
31. Roberts, D., Tolfree, D., & McIntire, H. (2007). Using Confinement as a Means to Estimate Pillar Strength in a Room and Pillar Mine. 1st Canada - U.S. Rock Mechanics Symposium. Vancouver, Canada: American Rock Mechanics Association. Hoek, E., & Brown, E. (1980). *Underground Excavations in Rock*. London: Institution of Mining and Metallurgy.
32. Süner, Mustafa Can, "The Effect of Natural Fractures on the Mechanical Behavior of Limestone Pillars: A Synthetic Rock Mass Approach Application" (2021). Graduate Theses, Dissertations, and Problem Reports. 8254. <https://researchrepository.wvu.edu/etd/8254>
33. Suner, M and Tulu, I. Examining the Effect of Natural Fractures on Stone Mine Pillar Strength through Synthetic Rock Mass Approach. *Mining, Metallurgy & Exploration* (2022) (In press).
34. Priest, S., & Hudson, J. (1981). Estimation of discontinuity spacing and trace length using scanline surveys. *International Journal of Rock Mechanics and Mining Sciences & Geomechanics Abstracts*, 189-197.
35. Elmo, D. (2006). Evaluation of a Hybrid FEM/DEM Approach for Determination of Rock Mass Strength using a Combination of Discontinuity Mapping and Fracture Mechanics Modelling with Particular Emphasis on Modelling of Jointed Pillars.
36. Vazaios, I., Diederichs, M., & Vlachopoulos, N. (2014). Factors Affecting Realism of DFNs for Mechanical Stability Analysis. *International Discrete Fracture Network Engineering Conference*. Vancouver, Canada.
37. Monsalve, J., Baggett, J., Bishop, R., & Ripepi, N. (2018). Integration of Laser Scanning and Numerical Modelling in 3DEC in Structurally Controlled Underground Limestone Mines. SME.
38. Iannacchione, A., & Coyle, P. (2002). An Examination of the Loyalhanna Limestone's Structural Features and their Impact on Mining and Ground Control Practices. *Proceedings of the 21st International Conference on Ground Control in Mining*. Morgantown, WV. Esterhuizen 2021
39. Damjanac, B., & Fairhurst, C. (2010). Evidence for a Long-Term Strength Threshold in Crystalline Rock.
40. Damjanac, B., Martin, D., Diederichs, M., McCreath, D., & Lam, T. (2012). Long-Term Stability for a Proposed Nuclear Waste Deep Geological Repository: Bruce Nuclear Site, Ontario, Canada. *Rock Engineering and Technology for Sustainable Underground Construction Eurock*. Stockholm, Sweden: Eurock.
41. Hedley, D., & Grant, F. (1972). *Stope-and-Pillar Design for the Elliot Lake Uranium Mines*. Ottawa: Department of Energy, Mines and Resources Mines Branch.
42. Hudyma, M. (1988). Development of Empirical Rib Pillar Design Criterion for Open Stope Mining.
43. Krauland, N., & Soder, P. (1987). Determining Pillar Strength From Pillar Failure Observation. *Engineering and Mining Journal*, 34-40.

44. Sjöberg, J. (1992). Failure Modes and Pillar Behavior in the Zinkgruvan Mine. Rock Mechanics.



## 9.0 Appendix

**Table A1.** *TUAV components power and weight specifications.*

Part Name	Manufacturer	Model	Quantity	Power (W)	Weight (g)
Quadrotor Frame	Holybro	X500	1	-	470
Brushless Motors	T-MOTOR	MN3520 KV400	4	680	888
Propellers	T-MOTOR	P12x4 Prop	4	-	58
Electronic Speed Controllers	T-MOTOR	FLAME HV 60A	4	-	294
Flight Management Unit	Holybro	Pixhawk 4	1	2.5	16
Power Management Board	Holybro	PM07	1	-	40
Telemetry Transmitter	Holybro	TT Radio V3 915 MHz	1	0.5	38
GPS Antenna	Holybro	Pixhawk 4 GPS Module	1	0.8	32
Companion Computer	Intel	NUC11i5PAH (without case)	1	36	210
LiDAR Camera	Intel	RealSense L515	1	3.3	95
Tracking Camera	Intel	RealSense T265	1	1.5	55
UWB Transceiver Module	Decawave	DWM1001	1	0.3	-
Distance Measurement Sensor	Garmin	LidarLite3	1	0.7	22
Distance Measurement Sensor	Garmin	LidarLite4	1	0.7	22
Inertial Measurement Unit	Analog Devices	ADIS-16495 2BMLZ-ND	1	0.3	42
RC Receiver	Spektrum	AR620 DSMX 6-Channel	1	-	8
Microcontroller	Arduino	UNO R3	1	0.2	25
Flexible Wire (16AWG, 2 cond.)	BNTECHGO	-	-	-	570